

MODELLING AND SIMULATION OF
SINGLE DIELECTRIC BARRIER DISCHARGE
PLASMA ACTUATORS

A Dissertation

Submitted to the Graduate School
of the University of Notre Dame
in Partial Fulfillment of the Requirements
for the Degree of

Doctor of Philosophy

by

Dmitriy M. Orlov, B.S., M.S.A.E.

Thomas C. Corke, Director

Graduate Program in Aerospace and Mechanical Engineering

Notre Dame, Indiana

October 2006

© Copyright by
Dmitriy M. Orlov
2006
All Rights Reserved

MODELLING AND SIMULATION OF
SINGLE DIELECTRIC BARRIER DISCHARGE
PLASMA ACTUATORS

Abstract

by

Dmitriy M. Orlov

This work presents the study of the single-dielectric barrier discharge aerodynamic plasma actuator. The physics of the plasma discharge was studied through the time-resolved light intensity measurements of the plasma illumination. Plasma characteristics were obtained and analyzed for a range of applied voltage amplitudes and a.c. frequencies.

Based on this data, electro-static and lumped-element circuit models were developed. The time-dependent charge distribution was used to provide boundary conditions to the electric field equation that was used to calculate the actuator body force vector. Numerical flow simulations were performed to study the effect of the plasma body force on the neutral fluid. The results agreed well with the experiments.

An application of the plasma actuators to the leading-edge separation control on the NACA 0021 airfoil was studied numerically. The results were obtained for a range of angles of attack for uncontrolled flow, steady and unsteady plasma actuation. The aerodynamic stall of the airfoil was studied. Improvement in the airfoil characteristics was observed in numerical simulations at high angles of

Dmitriy M. Orlov

attack in cases with plasma actuation. The computational results corresponded very well with experimental observations.

In memory of Mikhail Aleksandrovich Vostrikov.

CONTENTS

FIGURES	v
ACKNOWLEDGMENTS	xii
CHAPTER 1: INTRODUCTION	1
1.1 Background	1
1.2 Objectives	13
CHAPTER 2: PHYSICAL PROPERTIES OF PLASMA ACTUATOR. . .	15
CHAPTER 3: ELECTRO-STATIC MODEL	37
3.1 Mathematical and Numerical Formulation	37
3.1.1 Electro-static Model	38
3.1.1.1 Governing equations for electro-static problem and body force	38
3.1.1.2 Numerical Formulation of Electro-static Problem	44
3.1.2 Flow Problem	47
3.1.2.1 Governing Equations for Flow Problem	47
3.1.2.2 Boundary Conditions	48
3.1.2.3 Model Problem	51
3.1.2.4 Numerical Formulation of Flow Problem	52
3.2 Results	54
3.2.1 Body Force Results	54
3.2.2 Flow Problem Results with Spatially Weighted Body Force	69
3.2.3 Flow Problem Results with Temporally-spatially weighted body force.	80
CHAPTER 4: LUMPED-ELEMENT CIRCUIT MODEL	91
4.1 Spatial Lumped-Element Circuit Model	91
4.1.1 Mathematical Formulation	91

4.1.2	Numerical Formulation of Temporal Lumped-Element Circuit Model	97
4.1.3	Results	98
4.2	Spatial-Temporal Lumped-Element Circuit Model	107
4.2.1	Mathematical Formulation	107
4.2.2	Numerical Formulation of Space-Time Lumped-Element Circuit Model	114
4.2.3	Results of Space-Time Lumped-Element Circuit Model	116
CHAPTER 5: MODELING OF LEADING-EDGE SEPARATION CONTROL USING PLASMA ACTUATORS.		141
5.1	Background	141
5.2	Problem Formulation	142
5.3	Results	153
CHAPTER 6: CONCLUSIONS AND RECOMMENDATIONS FOR FUTURE WORK		173
6.1	Conclusions	173
6.1.1	Physics of Discharge	173
6.1.2	Electrostatic Model	175
6.1.3	Lumped-element Circuit Model	176
6.1.4	Leading-edge Separation Control	178
6.2	Recommendations For Future Work	180
6.2.1	Physical Properties of Plasma Discharge	180
6.2.2	Improvements to the Lumped-element Circuit Model	181
6.2.3	Applications	183
BIBLIOGRAPHY		184

FIGURES

1.1	The aerodynamic plasma actuator in a chord-wise section.	2
1.2	The dielectric barrier discharge is self-limiting because charge buildup on the dielectric surface opposes the voltage applied across the plasma, when the applied voltage is negative going (a), or the charge transferred through the plasma is limited to that deposited on the dielectric surface, when the voltage reverses (b).	4
2.1	Experimental setup used in measuring plasma light emission for SDBD model validation.	16
2.2	Schematic of experimental setup used in measuring plasma light emission.	17
2.3	Representative voltage (a), current (b) and PMT output (c) time series for SDBD plasma actuator.	18
2.4	Space-time variation of the measured plasma light emission for SDBD plasma actuator corresponding to one period, T , of the input a.c. cycle.	20
2.5	Contour lines of space-time variation of the measured plasma light emission for SDBD plasma actuator corresponding to one period, T , of the input a.c. cycle.	21
2.6	Plasma sweep velocity as function of applied voltage amplitude. .	22
2.7	Maximum plasma extent as function of applied voltage amplitude. 23	23
2.8	Space-time variation of the measured plasma light emission for SDBD plasma actuator at $V_{app} = 5$ kV and $f_{a.c.} = 5$ kHz.	25
2.9	Space-time variation of the measured plasma light emission for SDBD plasma actuator at $V_{app} = 5$ kV and $f_{a.c.} = 6$ kHz.	26
2.10	Space-time variation of the measured plasma light emission for SDBD plasma actuator at $V_{app} = 5$ kV and $f_{a.c.} = 7$ kHz.	27
2.11	Space-time variation of the measured plasma light emission for SDBD plasma actuator at $V_{app} = 5$ kV and $f_{a.c.} = 8$ kHz.	28

2.12	Space-time variation of the measured plasma light emission for SDBD plasma actuator at $V_{app} = 5$ kV and $f_{a.c.} = 9$ kHz.	29
2.13	Space-time variation of the measured plasma light emission for SDBD plasma actuator at $V_{app} = 5$ kV and $f_{a.c.} = 10$ kHz.	30
2.14	Space-time variation of the measured plasma light emission for SDBD plasma actuator at $V_{app} = 5$ kV and $f_{a.c.} = 11$ kHz.	31
2.15	Plasma sweep velocity as function of applied a.c. frequency.	32
2.16	Maximum extent of the plasma as function of applied a.c. frequency.	33
2.17	Total light emission for SDBD plasma actuator as function of applied a.c. frequency.	34
2.18	Total light intensity from the plasma actuator as function of applied voltage amplitude.	35
3.1	One-dimensional electric field acting on the charges.	40
3.2	Rectangular computational domain with solid boundaries.	49
3.3	Computational domain with two electrodes separated by the dielectric.	55
3.4	Numerical grid for the electro-static problem with Robert's stretching applied to resolve electric field and body force near the electrodes.	59
3.5	Zoomed-in view of the numerical grid for the electro-static problem with Robert's stretching applied to resolve electric field and body force near the electrodes.	60
3.6	Electric potential φ as a function of space coordinates.	61
3.7	Lines of constant electric potential near inner edge of electrodes.	62
3.8	Electric field \vec{E} in the upper part of the domain (air), near inner electrodes' edges.	63
3.9	Body force as result of electro-static equation solution.	64
3.10	Body force on the fluid flow scale.	65
3.11	Incorrect flow resulting from non-weighted body force. The largest velocity vector corresponds to $ V = 2$ m/s.	66
3.12	Spatial variation of light intensity from the plasma actuator.	68
3.13	Spatially-weighted body force.	70
3.14	Computational domain, normalized by X_{max} and Y_{max} , actuator located on the bottom surface at $X = 0.5$	71
3.15	Body force is introduced into the Navier-Stokes equations at time $t = 0$	73

3.16	“Starting” vortex near actuators at $t = 0.25ms$. The largest velocity vector corresponds to $ V = 1.5$ m/s.	74
3.17	“Starting” vortex near actuators at $t = 1.25ms$. The largest velocity vector corresponds to $ V = 3$ m/s.	75
3.18	PIV setup by Post [61].	76
3.19	PIV laser trigger setup by Post [61].	76
3.20	“Starting” vortex at $t = 2, 12, 35, 60$ ms, PIV results by Post [61].	77
3.21	Velocity field of the developed jet flow at $T \rightarrow \infty$.The largest velocity vector corresponds to $ V = 4.7$ m/s.	78
3.22	Developed jet flow at $T \rightarrow \infty$, PIV results by Post [61].	79
3.23	Magnitude of the space-time weighting function used on the electrostatic body force for one half of the a.c. cycle.	81
3.24	Method for introducing space-time weighting of electro-static body force during time-steps of the Navier-Stokes solver.	82
3.25	x -component velocity profiles normalized by maximum velocities and the locations of maximum velocities at different locations downstream of the simulated actuator with spatial weighting of the body force and the steady (long-time) solution.	84
3.26	x -component velocity profiles taken at $X = 0.5938$ for different times following the impulsive start of the actuator body force. Body force is spatially weighted only.	85
3.27	x -component velocity profiles taken at $X = 0.5938$ for different times following the impulsive start of the actuator body force. Body force is spatially-temporally weighted.	86
3.28	Maximum x -component velocity as a function of time for impulsively started actuator body force. Star indicates first-order time constant corresponding to where $\frac{U}{U_{t \rightarrow \infty}} = \frac{1}{e}$	87
3.29	Maximum induced velocity in electro-static actuator model as a function of voltage.	89
4.1	Spatial lumped-element circuit model of a single dielectric barrier discharge plasma actuator.	93
4.2	Schematic showing three node points where voltage is followed in the circuit in the spatial lumped-element circuit model of a single dielectric barrier discharge plasma actuator.	95

4.3	Voltage time series for $\alpha = 0.1$ and $\alpha = 0.2$: applied voltage (solid line), surface voltage (dashed line), voltage difference (dotted line), and plasma threshold (dash-dotted line).	100
4.4	Voltage time series for $\alpha = 0.3$ and $\alpha = 0.4$: applied voltage (solid line), surface voltage (dashed line), voltage difference (dotted line), and plasma threshold (dash-dotted line).	101
4.5	Applied voltage and rectified current in the circuit, experimental results.	102
4.6	Average dissipated power as a function of the applied voltage based on the actuator model.	104
4.7	Dependence of plasma actuator maximum induced velocity (open symbols) and plasma dissipated power based on lumped-element circuit model(closed symbols as a function of applied a.c. voltage.	105
4.8	Maximum extent of the plasma as function of applied voltage amplitude for temporal lumped-element circuit model simulation and experiments (Enloe [20] and present).	106
4.9	The physical space over the encapsulated electrode is divided into N sub-regions.	108
4.10	Electric circuit model of a single dielectric aerodynamic plasma actuator.	109
4.11	Schematic drawing of the n-th air capacitor.	110
4.12	Schematic drawing of the n-th dielectric capacitor.	111
4.13	Maximum value of the plasma body force as function of the number of parallel networks.	113
4.14	Voltage on the surface of the dielectric in the first five sub-circuits (n=1,2,3,4,5) obtained from space-time lumped element circuit model.	117
4.15	Plasma current in the first five sub-circuits (n=1,2,3,4,5) obtained from space-time lumped element circuit model.	118
4.16	Rectified plasma current for one a.c. period of input obtained from space-time lumped element circuit model.	120
4.17	Contour lines of constant rectified plasma current obtained from space-time lumped element circuit model.	121
4.18	Comparison between space-time model and experiments for the maximum plasma extent over covered electrode as function of voltage.	123
4.19	Comparison between space-time model and experiment for plasma sweep velocity as function of voltage.	124

4.20	Comparison between space-time model and experiment for maximum extent of the plasma as function of applied a.c. frequency.	125
4.21	Comparison between space-time model and experiment for plasma sweep velocity as function of applied a.c. frequency.	126
4.22	Computational domain for calculation of unsteady plasma body force.	128
4.23	Normalized plasma bodyforce magnitude as function of time and position over covered electrode.	130
4.24	Normalized maximum value of the plasma bodyforce magnitude as function of time. Dots indicate where the snapshots of the body force vector fields are taken.	131
4.25	Plasma body force vector field and body force amplitude at $t = 0.2 \cdot T_{a.c.}$. The body force is normalized by the maximum value in the a.c. cycle.	132
4.26	Plasma body force vector field at $t = 0.4 \cdot T_{a.c.}$. The body force is normalized by the maximum value in the a.c. cycle.	133
4.27	Plasma body force vector field at $t = 0.7 \cdot T_{a.c.}$. The body force is normalized by the maximum value in the a.c. cycle.	134
4.28	Plasma body force vector field at $t = 0.9 \cdot T_{a.c.}$. The body force is normalized by the maximum value in the a.c. cycle.	135
4.29	Spectrum of the plasma body force obtained with space-time lumped-element circuit model.	137
4.30	Effect of dielectric material on plasma body force.	138
4.31	Effect of dielectric material on power dissipated by the plasma actuator.	139
5.1	Schematic of the plasma actuator on the leading edge of NACA 0021 airfoil for body force computations.	144
5.2	Unstructured grid near leading edge of NACA 0021 airfoil for plasma body force computations.	145
5.3	Computed steady plasma body force vectors near leading edge of NACA 0021 airfoil, shown on structured computational grid used for flow solver.	146
5.4	Full view of computational grid used for the flow simulation of the NACA 0021 airfoil.	147
5.5	Zoomed-in view of computational grid showing grid point clustering in the region of the boundary layer.	148

5.6	Lift and drag coefficients convergence history at 5 degrees angle of attack, $U_{fs} = 35$ m/s, uncontrolled flow.	155
5.7	Lift and drag coefficients convergence history at 25 degrees angle of attack, $U_{fs} = 35$ m/s, uncontrolled flow.	156
5.8	Lift coefficient versus angle of attack at $U_{fs} = 35$ m/s for uncontrolled flow.	157
5.9	Example of short duty cycle a.c. input for unsteady operation of plasma actuators (a) and its numerical representation (b).	159
5.10	Velocity vector field near leading edge of airfoil at $t = 0.00001$ seconds after the impulsive start of the actuator. The largest velocity vector corresponds to $ V = 4.03$ m/s.	160
5.11	Velocity vector field near leading edge of airfoil at $t = 0.02$ seconds after the impulsive start of the actuator. The largest velocity vector corresponds to $ V = 8.34$ m/s.	161
5.12	Velocity vector field near leading edge of airfoil at $t = 0.06$ seconds after the impulsive start of the actuator. The largest velocity vector corresponds to $ V = 8.36$ m/s.	162
5.13	Velocity vector field near leading edge of airfoil at $t = 0.18$ seconds after the impulsive start of the actuator. The largest velocity vector corresponds to $ V = 8.37$ m/s.	163
5.14	Velocity vector field (a) and contour lines of $\lambda_2 = 0$ (b) at $t = 0.01743$ seconds in still air. The plasma actuator is working in unsteady mode at 120 Hz. The largest velocity vector corresponds to $ V = 4.49$ m/s.	164
5.15	Contour lines of stream function (a) and $\lambda_2 = 0$ (b), no actuation, 23 degrees angle of attack.	165
5.16	Contour lines of stream function (a) and $\lambda_2 = 0$ (b) for steady actuation, 23 degrees angle of attack.	166
5.17	Contour lines of stream function (a) and $\lambda_2 = 0$ (b) for unsteady actuation at 120 Hz, duty cycle of 10%, 23 degrees angle of attack.	167
5.18	Lift coefficient versus angle of attack at $U_{fs} = 35$ m/s for uncontrolled flow, steady and unsteady actuation.	168
5.19	Drag coefficient versus angle of attack at $U_{fs} = 35$ m/s for uncontrolled flow, steady and unsteady actuation.	169
5.20	Drag polar at $U_{fs} = 35$ m/s for uncontrolled flow, steady and unsteady actuation.	170

5.21	$\frac{C_L}{C_D}$ versus angle of attack at $U_{fs} = 35$ m/s for uncontrolled flow, steady and unsteady actuation.	171
5.22	Comparison between numerical and experimental data for lift coefficient versus angle of attack for uncontrolled case, steady and unsteady actuation. Numerical simulations performed at $U_{fs} = 35$ m/s. Experiment performed at $U_{fs} = 30$ m/s, adopted from [52]. .	172

ACKNOWLEDGMENTS

I want to thank Orbital Research Inc and USAF/AFRL, WPAFB who supported this research under contract number FA8650-04-C-3405. I would like to acknowledge the USAF program manager Dr. Charles Suchomel, and Mr. Mehul Patel, the PI/Program manager at Orbital Research Inc. Additional support for this research came from contract with Boeing Inc that was monitored by Mr. Joseph Silkey.

I wish to thank Professor Thomas C. Corke, my advisor, mentor and teacher, for his continued guidance, support, encouragement and inspiration provided throughout the whole period of my research, for the opportunities and challenges that allowed me to gain priceless experience.

I would like to express my appreciation to the members of the doctoral committee, Professor C. Lon Enloe, Professor Flint O. Thomas, and Professor Eric J. Jumper, for reviewing the dissertation and providing useful suggestions and comments.

Special recognition is due to Dr. Martiqua L. Post for the valuable experimental data that provided the reference point for my numerical models. Thank you to Dr. Eric H. Matlis for his expertise in software and hardware. Thank you to Dr. Stanislav V. Gordeyev for helpful discussions, criticism and advice. Thank you to Dr. Ercan Erturk and Dr. Osamah Haddad for their guidance. Thank you to Mr. Thomas Apker for his assistance with the Fluent UDF computations. I

also wish to thank all of my friends and colleagues at Hessert Lab for their help and support.

I am especially grateful to my parents Galina and Mikhail Orlov, and my grandmother Zoya Vostrikova without whose never-ending love and support none of this would have been possible.

Thank you to Daria, my beautiful wife for the encouragement and patience, support and understanding, for everything that words cannot express.

CHAPTER 1

INTRODUCTION

1.1 Background

The aerodynamic plasma actuator is a particular configuration of the Single-Dielectric Barrier Discharge, specifically, a surface discharge. The configuration of the plasma actuator is simple. It consists of two electrodes arranged highly asymmetrically. One of the electrodes is exposed to the surrounding air, and the other is totally encapsulated in a dielectric material, as shown on Figure 1.1. Typically, the plasma actuator's electrodes are long and thin and are arranged span-wise on an aerodynamic surface.

When a high 5 – 20 kV peak-to-peak AC voltage at frequencies from 3 to 15 kHz is applied, a plasma discharge appears on the insulator surface above the insulated electrode, and directed momentum is coupled into the surrounding air. The amount of the momentum coupling is effective in substantially altering the airflow over the actuator surface.

The plasma actuators have been successfully used in different flow control applications, such as exciting boundary layer instabilities on a sharp cone at Mach 3.5 [44], lift augmentation on a wing section [13, 14, 46, 54], low-pressure turbine blade separation control [31–34, 41], turbine tip clearance flow control [15, 45, 74], bluff body control [8, 73], drag reduction [35, 78], unsteady vortex generation

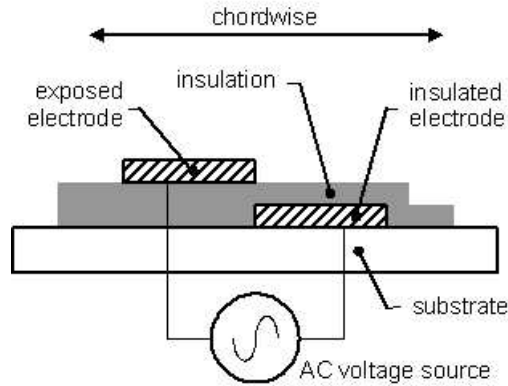


Figure 1.1. The aerodynamic plasma actuator in a chord-wise section.

[48, 50, 51, 75], and airfoil leading-edge separation control [12, 52, 58, 59, 61–63]. The advantages of the plasma actuator flow control device over traditional flow control devices are: reduced size and weight, absence of moving parts, increased reliability, inexpensiveness, high bandwidth (quick response), reduced drag, increased aerodynamic agility.

Plasma actuator's behavior is primarily governed by the buildup of charge on the dielectric-encapsulated electrode. When AC voltage is applied, a plasma discharge appears on the insulator surface above the encapsulated electrode, and directed momentum is coupled into the surrounding air. In operation, the plasma in the discharge appears on the surface of the dielectric each half-cycle of the applied AC voltage.

To the unaided eye, the plasma appears as a relatively uniform diffuse discharge, but optical measurements of the plasma indicate that it is highly structured in both space and time. The temporal nature of the actuator indicates that this plasma is indeed a single dielectric barrier discharge [19]. The most important

feature of the SDBD is that it can sustain a large-volume discharge at atmospheric pressure without the discharge collapsing into a constricted arc.

The SDBD can maintain such a discharge because the configuration is self-limiting, as shown in Figure 1.2. To maintain a SDBD discharge, an AC applied voltage is required. Figure 1.2 (a) illustrates the half cycle of the discharge for which the exposed electrode is more negative potential than the surface of the dielectric, being the cathode in the discharge. In this case, assuming the potential difference is high enough, the exposed electrode can emit electrons. Because the discharge terminates on a dielectric surface, the build up of the surface charge opposes the applied voltage, and the discharge shuts itself off unless the magnitude of the applied voltage is continually increased.

The behavior of the discharge is similar on the opposite half-cycle: a positive slope in the applied voltage is required to maintain the discharge. In this half-cycle, the charge available to the discharge is limited to that deposited during the previous half-cycle on the dielectric surface, which now plays the role of the cathode, as shown in Figure 1.2 (b). This self-limiting behavior due to charge buildup on the dielectric surface impacts the spatial and temporal structure of the plasma.

Although the plasma is composed of charged components, it is net neutral, being created by the ionization of neutral air, as many negative electrons as positive ions exist in the plasma. Responding to the external electric field, the electrons move to the positive electrode and the ions to the negative, resulting in an imbalance of charges on the edges of the plasma. The charge imbalance sets up an electric field in the plasma opposite to that of the external applied field. The re-

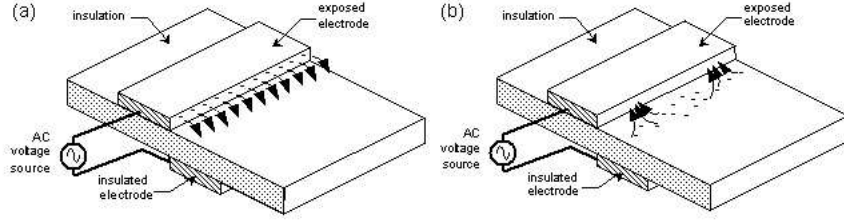


Figure 1.2. The dielectric barrier discharge is self-limiting because charge buildup on the dielectric surface opposes the voltage applied across the plasma, when the applied voltage is negative going (a), or the charge transferred through the plasma is limited to that deposited on the dielectric surface, when the voltage reverses (b).

arrangement of the charges will continue until the net electric field in the plasma is neutralized.

The density of the positive and negative charges will be equal in the bulk of the plasma. Only on the edges will there be a charge imbalance, due to the thermal motion of the particles. The thickness of the regions along the edges in which the plasma supports a net positive or negative charge density is determined by the shielding length, or Debye length, of the plasma.

The time scale of the charge rearrangement process in the plasma is on the order of $10^{-9} - 10^{-8}$ seconds (for electron temperature of $1000 - 10000$ K, with a mobility velocity on the order of $10^5 - 10^6$ m/s [64]). This plasma formation time is several orders of magnitude smaller than the time during which the plasma is producing an effect on the surrounding air.

Thus, we see, that there are three separate temporal time scales that are relevant to the SDBD process. The shortest time scale, of the order of 10^{-8} seconds, is associated with the initiation of the micro-discharges across the plasma

actuator gap leading to charge redistribution. The second time scale is related to the operation of the plasma actuator itself. It is defined by the period of the a.c. cycle that drives the alternating current discharge. This time scale is on the order of 10^{-4} sec (for an a.c. frequency of the order of 10 kHz), which is approximately 10^4 times slower than the time scale of the micro-discharges. The third timescale is the one that governs the movements of the neutral fluid responding to the plasma actuator. This time scale is on the order of 10^{-2} seconds.

The four order of magnitude difference in time scales allows us to assume that the plasma formation and charge rearrangement processes are instantaneous. This allows us to assume that the plasma is operating in a quasi-steady regime, when the charges are rearranged in the region, so that they cancel the external electric field everywhere, except the small regions near the electrodes. This leads to the quasi-DC assumption used in modeling the plasma formation and computing the plasma body force.

The dielectric barrier discharge process provides a means for efficiently ionizing gases at atmospheric pressure that is well suited for many chemical plasma processes. As a result it is a well studied and understood process. One of the earliest references was in 1857 when Siemens [70] proposed a novel type of electrical gas discharge, that could generate ozone from atmospheric pressure oxygen or air. Since then, the DBDs have been widely used for different applications. The classical Dielectric Barrier Discharge configuration utilizes planar or cylindrical electrode arrangements with at least one dielectric layer placed between the electrodes.

The discharge investigated in the present research results from activating a model at atmospheric pressure at frequencies typically in the 1 – 10 kHz range and

voltages in the several kilovolts range. There is a wide variance in the terminology used for the discharge in literature. The names assigned to the phenomena include atmospheric glow discharge, surface barrier discharge (SBD), dielectric barrier discharge (DBD), Single Dielectric Barrier Discharge (SDBD) and Surface Plasma Chemistry Process (SPCP).

Despite of considerable progress in understanding the structure and the properties of such discharges, which principally occurred in the last few decades, the present knowledge of this subject appears to be insufficient to provide an adequate quantitative theoretical description for barrier discharge behavior in air at high (atmospheric) pressure. Although, a classic symmetric DBD has been widely studied, asymmetric electrode arrangements such as those used in the plasma flow control actuators have not been studied, until recently. All the studies of the plasma actuator that were done in the past years may be divided into three major categories: the physics of the SDBD discharge, the optimization of the plasma actuator, and the applications.

The physics of the discharge can be studied using different techniques. Some of this methods are more direct. These may include the electric current and light intensity observations [19–21, 37]. The others are less direct, and help to study the plasma actuator physics through the effects that it produces on the ambient fluid. One of the first techniques was based on the smoke visualization and was used to demonstrate the plasma actuator effect [60, 65]. The other methods include the hot wire, Pitot tube and DPIV flow velocity measurements [60, 61], acoustic [9], accelerometer [57] measurements. Kozlov *et al.* [38] used the spatially resolved cross-correlation spectroscopy to make well-resolved quantitative estimates of the electric field strength and relative electron density. A conventional

Schlieren technique was used by Wilkinson and Konkle-Parker [77] to visualize the flow field induced by an SDBD plasma actuator. Enloe *et al.* have used the laser deflection technique to measure the air density variations near and in the plasma region.

A thorough study of the plasma actuator physics has been performed by Enloe *et al.* [19–21]. In their work, they have used the photomultiplier technique to study the temporal and spatial structure of the plasma discharge. Through the comparison between the electric current in the actuator and the light emission PMT measurements it was shown that these two correlate, and that we can use the light intensity information to study the physics of the barrier discharge. It was also discovered that there existed a noticeable difference between the two halves of the a.c. cycle when the applied voltage was negative-going and when it was positive-going. It was also shown experimentally that power dissipated in the plasma actuator was increasing as the applied voltage to the power of $7/2$, $P \propto V_{app}^{7/2}$, and that this functional relation was typical for this surface dielectric barrier discharges.

The same functional dependence was observed by Post [60, 61] for the plasma induced velocity, $U \propto V_{app}^{7/2}$. Post has also shown that the plasma actuators placed in arrays had an additive effect, and two actuators working in array create a plasma induced jet in which momentum of two is twice the momentum from a single actuator. This characteristic of the plasma actuator was also observed by Forte *et al.* [24] in their Pitot tube and LDV measurements.

Enloe *et al.* have performed the studies of the atmospheric composition on the plasma actuator efficiency [18]. The presence of oxygen in the atmosphere is known to allow for the formation of negative ions via attachment of electrons to

the oxygen. As their results indicate, the actuator performance directly correlates with the fraction of the oxygen in the atmosphere, and its efficiency increases linearly with the percentage of oxygen.

There has been a recent attempt by Anderson *et al.* to measure the dependence of the plasma actuator effects on the air humidity [7]. Their results showed that the plasma actuator performance did not change with the increase of the relative air humidity. This is most probably due to the fact that a very small range of humidities was checked (40-60 %). It also should be mentioned that the absolute humidity is more important for the plasma actuator operation than the relative humidity.

These studies of the plasma actuator had two major goals: one was to understand the physics of the single dielectric barrier discharge, and the other was to optimize the plasma actuator to increase its effectiveness.

The first major attempts on the plasma actuator optimization were done by Post [61] and Enloe *et al.* [20, 21]. They have shown the vital role played by the asymmetry. This was shown by covering the open electrode by a dielectric layer. They have also studied the effects of the geometry on the performance of the plasma actuator. It was discovered that the width of the lower electrode is very important, and that this covered electrode should be sufficiently wide for the plasma formation. It was also shown that a small gap or overlap of the electrodes does not change the performance characteristics of the actuator, but affects the stability of the plasma discharge ignition. The slight overlap makes the plasma ignition more uniform.

The other important characteristic that affects the performance of the plasma actuator is the form of the applied voltage signal. As the physics of the SDB

discharge suggested, the formation of the plasma is directly related to the voltage change across the actuator. The steeper and longer the slope of the voltage signal, $\frac{dV}{dt}$, the more plasma is formed on the surface of the dielectric, the higher is the induced flow velocity by the actuator. Post [61] tested different forms of the input a.c. signal and found the best results when the applied voltage had the form of the “positive sawtooth”.

As it was already mentioned, all the measurement techniques described above provide plenty of indirect information about the plasma actuators. But these experimental techniques do not allow us to obtain directly the information about the distribution of electric field and electron density along the discharge axis. Therefore, an important role in the investigation of such discharges is played by numerical modeling.

One of the first models was developed by Massines *et al.* [43]. The one-dimensional model was based on a simultaneous solution of the continuity equations for charged and excited particles, and the Poisson equation. The study allowed one to obtain spatial-temporal distributions for plasmas. It has been shown that the processes in a discharge volume are characterized by such values as mobility, diffusion coefficient, and ionization rate constant.

Research, related to the present work, has been done by Paulus *et al.* [55]. A particle-in-cell simulation was used to study the time-dependent evolution of the potential and the electrical field surrounding two-dimensional objects during a high voltage pulse. The numerical procedure was based on the solution of Poisson’s equation on a grid in a domain containing an L-shaped electrode, and the determination of the movement of the particles through the grid. The simulation showed that the charged particles moved toward the regions of high electric po-

tential, creating high electric strength fields near the electrode's edges. It also proved that the plasma builds up on a microsecond time scale.

There was also an attempt to model the plasma actuator effects without modeling the discharge process using an approximation model. A first-order approach to modeling the effect of plasma actuators using the potential flow model was developed by Hall *et al.* [28, 29]. In this model, the plasma actuator was represented by a doublet and incorporated into a Smith-Hess panel code. Hall has shown [29] that after the calibration of the doublet strength, it could duplicate experimental data for the change in airfoil lift characteristics due to applying plasma actuators. The development of this model was driven by the experimental observations of the similar streamline patterns produced by the plasma actuator on the surface of a flat plate in a uniform flow and those of an inversed doublet at the wall.

Enloe *et al.* [20, 21] provided a formulation for the body force produced by the SDBD plasma actuator on the ambient air. Another model for the plasma body force was presented by Roth *et al.* [65]. This model is based on the derivation of the forces in gaseous dielectrics by Landau [39]. In this model, the body force is proportional to the gradient of the squared electric field:

$$F_b = \frac{d}{dx} \left(\frac{1}{2} \epsilon_0 E^2 \right) \quad (1.1)$$

As it has been shown by Enloe *et al.* [19] this model for the body force does not account for the presence of the charged particles. For example, in the absence of charged particles the body force calculated using equation (1.1) is not zero, which is an obvious error. It has been also shown by Enloe *et al.* that the body force given by equation (1.1) and in form derived in the present work are not equal, except in the special case of a one-dimensional condition where $\vec{E} = E_x \hat{i}$

and $E_y = E_z = 0$, and $\partial/\partial y = \partial/\partial z = 0$. This special case is not relevant to our aerodynamic applications.

Another model for the body force was given by Shyy *et al.* [69]. The time-averaged body force was calculated as

$$F_{tave} = \vartheta \alpha \rho_c e_c \Delta t E \delta \quad (1.2)$$

where ϑ is the frequency of the applied voltage, α is a factor to account for the collision efficiency, ρ_c is the charge density, e_c is the charge of electron, Δt is the time during which the plasma discharge takes place, E is the electric field, and δ is the Dirac delta function.

Shyy *et al.* varied the parameters related to the electrode operation, including the voltage, frequency, and free stream speed to investigate the characteristics of the plasma-induced flow and the heat transfer characteristics. It was shown based on their model that the induced flow velocities and heat flux vary proportionally with the applied frequency and voltage.

One of the largest disadvantages of their model lied in the electric field formulation that was based on an assumption that electric field strength E decreased linearly as one moved away from the inner edge of the electrodes. This assumption was not consistent with the physics of the discharge process, as recent measurements have shown [49].

Suzen *et al.* [71, 72] utilized the electrostatic model with the exponential weighting described in this thesis to compute the plasma body force using Enloe formulation [20, 21]. In their work, they proposed to split the electrostatic equations into two parts: the first one is due to the external electric field, and the second part is due to the electric field created by the charged particles. This is

making the problem unnecessarily overcomplicated because it is known that the electric fields can be superimposed. This idea is used later in this thesis.

On the other hand, there have been numerous models developed for dielectric barrier discharges in air that include very complicate chemistry. These models usually include 20 – 30 reaction equations with different reaction times and energy outputs. These equations account for electron, ion-neutral, and neutral-neutral reactions in different gases that are present in the air [26, 27, 38, 42, 53].

Mostly these models were developed for a simple one-dimensional dielectric barrier discharge due to need of the vast computational resources. Recently, Font *et al.* [22, 23] utilized these ideas to model the plasma discharge in the asymmetric plasma actuator. In their model they included nitrogen and oxygen reactions based on the experimental results of Enloe *et al.* [18]. With this model, Font was able to show the propagation of a single streamer from the bare electrode to the dielectric surface and back. Due to the fact that the complexity of the problem requires significant computational power, modeling of the whole a.c. cycle is still an open issue.

There also exists a group of simplified models in which the chemical reactions are not considered, but the gas is still considered as a mixture of ions, electrons and neutral molecules. These models were first derived for a simple one-dimensional discharge [66, 68], and later extended to two-dimensional dielectric barrier discharges [25, 56, 67].

Likhanskii *et al.* [40] modeled the weakly ionized air plasma as a four-fluid mixture of neutral molecules, electrons, and positive and negative ions, including ionization and recombination processes. Their simulations show a large importance of the presence of negative ions in the air. Likhanskii also points to the

leading role of charging the dielectric surface by electrons in the cathode phase which is critical, acting as a harpoon pulling positive ions forward and accelerating the gas in the anode phase.

Although these models usually give results which precisely describe all of the different processes involved in the plasma discharge, they are very time-consuming and require significant computer resources. Such calculations were either performed for simple one-dimensional symmetric domains, that are relevant to industrial plasma processes, or for a single streamer propagation in a two-dimensional case relevant to the plasma actuator geometry. Estimates of the computer resources needed for these simulations in air at high pressure are significant. Such simulations are not suitable as design tools used in the iterative optimization of the plasma actuators and for their use in applications.

1.2 Objectives

Given this background into the SDBD plasma actuator, the objectives of this work are the following:

1. Develop models for Single Dielectric Barrier Discharge plasma actuators that contain the essential physics, but are computationally efficient enough to be used in the design and optimization of flow control applications.
2. Derive the body force effect based on the SDBD models that ultimately does not require empirically determined coefficients.
3. Using the model, investigate various parameters such as voltage amplitude, frequency, and dielectric properties on the body force and power dissipated to seek optimum designs of plasma actuators.

4. Incorporate the space-time dependent body force into a numerical flow solver to determine the effect the actuators have on the neutral flow.
5. Utilize the flow solver in a practical application of leading-edge separation control and compare the simulation to an equivalent experiment.

CHAPTER 2

PHYSICAL PROPERTIES OF PLASMA ACTUATOR.

Previous experiments by Enloe *et al.* [20] have shown that the bulk current across the electrodes of a SDBD plasma actuator correlates with the light emission of the plasma. Therefore it is useful to study the space-time development of the light illumination in order to provide data that can be used in the physical modeling of the SDBD process. To accomplish this, a TSI Model 9162 photomultiplier tube was utilized to measure the plasma light emission from an actuator. The experimental setup is illustrated in Figure 2.1, and the schematic of the electrodes arrangement relative to the photomultiplier is shown in Figure 2.2. The photo-multiplier tube (PMT) used a double-slit optical tube in order to focus on a narrow slit of the ionized gas. The slit was aligned to be parallel to the edge of the exposed electrode. This provided a narrow view in the direction perpendicular to that at which the plasma sweeps out over the encapsulated electrode. The accuracy of the spatial measurements was 0.5 mm.

A representative time trace of the PMT output is shown in Figure 2.3 (c). Also shown are the comparable input voltage and measured bulk current time series acquired over the same time period. The current was measured by Pearson Current Monitor Model 2100 inductive current pickup that was placed around the wire lead to one of the electrodes. The response time of the inductive current pickup was 20 nanoseconds. The voltage was measured with a high voltage probe



Figure 2.1. Experimental setup used in measuring plasma light emission for SDBD model validation.

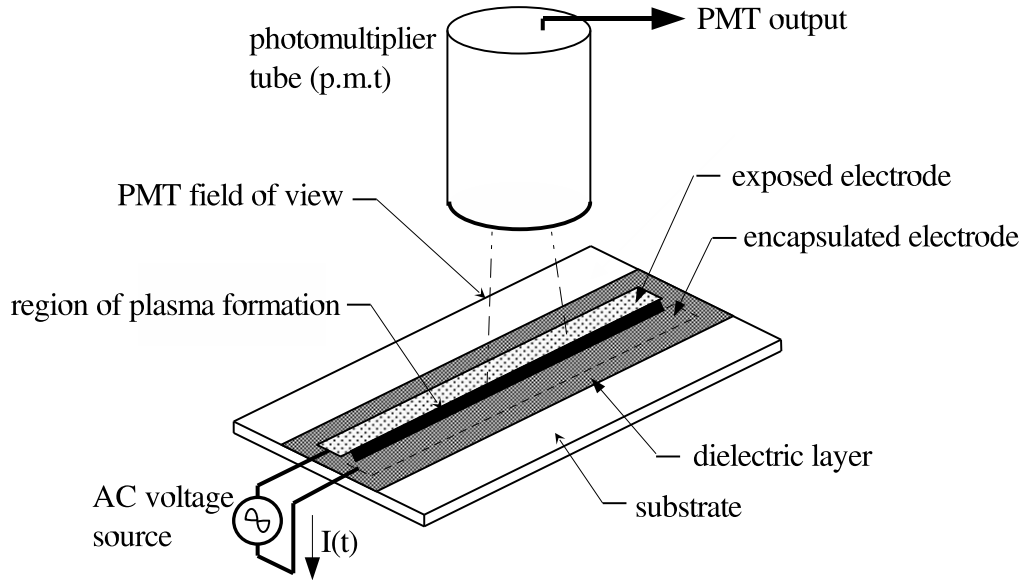
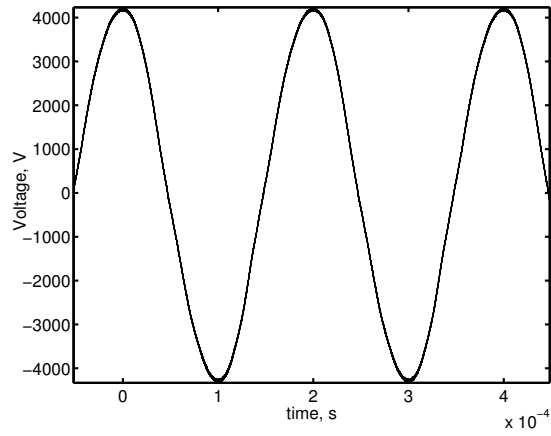


Figure 2.2. Schematic of experimental setup used in measuring plasma light emission.

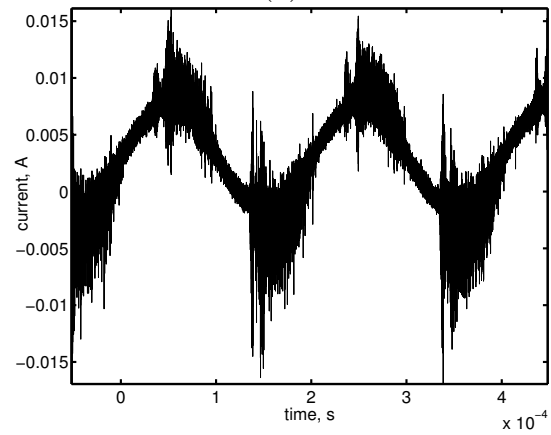
that was attached to one of the electrode leads. Both had frequency response that was much higher than the a.c. frequency (5 kHz) used in the experiment.

The narrow spikes in the current and PMT traces correspond to the part of the cycle when the plasma is present. These are narrow because they are dominated by the short-time-scale micro-discharges. These appear in both the current through the electrodes and the PMT output which is proportional to light intensity. Comparing the two indicates that the actuator current and plasma light emission are perfectly correlated, as had been previously shown by Enloe *et al.* [20].

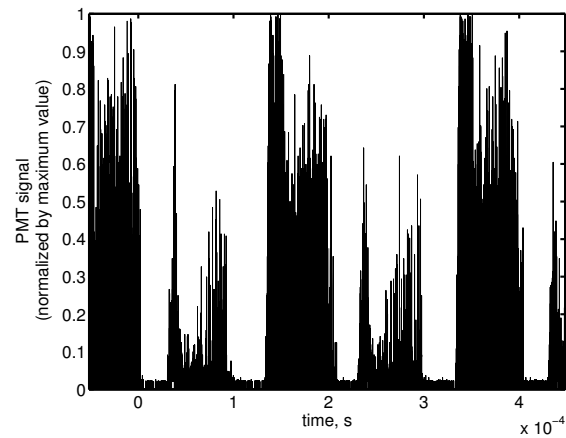
The plasma ignites and extinguishes twice in the a.c. period. The initiation of the ionization occurs when the potential difference between the electrodes exceeds a minimum threshold. When this occurs, the exposed surface of the dielectric becomes a “virtual electrode” on which charge builds up. When the charge builds



(a)



(b)



(c)

Figure 2.3. Representative voltage (a), current (b) and PMT output (c) time series for SDBD plasma actuator.

to a point where the potential difference between it and the exposed electrode is below the minimum to cause the ionization, the plasma extinguishes. This is the self-limiting character of the DBD process. We can observe this happening during both halves of the a.c. cycle.

We note that the current and the light intensity are different between the two halves of the a.c. cycle. The portion where the amplitude of the “spikes” is smaller is during that part of the cycle when the electrons that were deposited on the dielectric surface are then moving back to the bare electrode. This process is not as efficient so that there are fewer electrons to collide with ions and the current and the light intensity are weaker. In other experiments, by Enloe *et al.* [20], the bare electrode was also covered by a dielectric layer, a so-called Double Dielectric (DDBD), and the current amplitude associated with the ionization was completely symmetric in the a.c. cycle.

A comparison will be made later to the current time series from the lumped-element circuit model. The lumped-element circuit model, described in Chapter 4, simulates the charge and discharge occurring on the middle (msec) time scale that is representative of the body force. Therefore to compare this with the experimental current or PMT time traces, we draw a smooth curve that represents the envelope of the peaks of the narrow spikes caused by the micro-discharges. If one does this, the current traces from the model show similar character namely, a comparable phase shift with respect to the input voltage time series, plasma igniting and extinguishing twice in the a.c. period, and the non-equal current amplitudes between the two events.

The envelope of the amplitudes of the narrow spikes can be obtained from the experiment by taking multiple realizations that are phase locked with the input

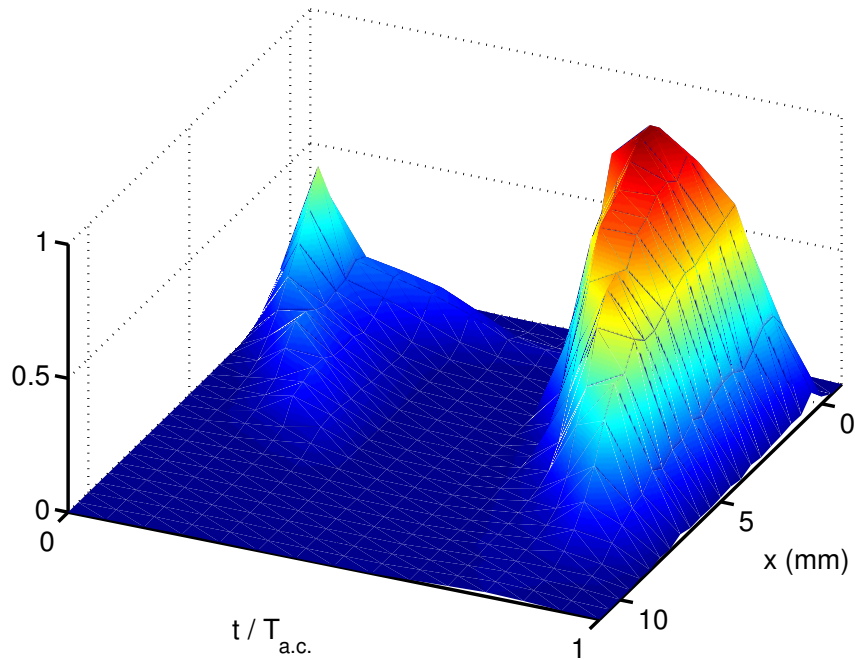


Figure 2.4. Space-time variation of the measured plasma light emission for SDBD plasma actuator corresponding to one period, T , of the input a.c. cycle.

voltage a.c. cycle. Because the micro-discharges are random in time, they occur at different times during the plasma generation portion of the cycle. Therefore when an average of many cycles is accumulated, the narrow spikes fill the space to indicate the maximum amplitude envelope. This has been done while viewing different slices of the plasma at different distances from the overlap junction of the exposed and encapsulated electrodes. The result is shown in Figure 2.4.

Figure 2.4 shows the space-time variation of plasma light emission for one period of the a.c. cycle. The light emission has been normalized by its maximum value in the cycle. The time axis corresponds to the a.c. period of the input voltage. The position axis refers to the location over the encapsulated electrode, with

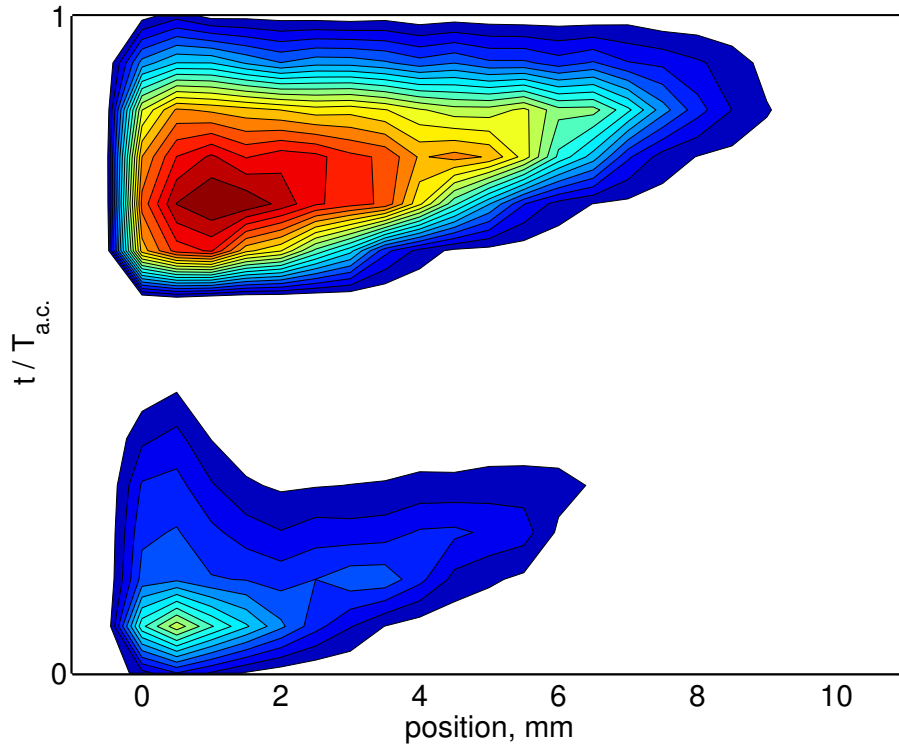


Figure 2.5. Contour lines of space-time variation of the measured plasma light emission for SDBD plasma actuator corresponding to one period, T , of the input a.c. cycle.

zero corresponding to the the overlap junction of the exposed and encapsulated electrodes.

The space-time character of the plasma formation over the actuator has a number of interesting features. For example, there is a sharp peak at the time of ignition. This occurs near the overlap junction. The plasma then sweeps out from the junction to cover a portion of the encapsulated electrode. As the plasma sweeps out, its light emission is less intense. The estimates are that the intensity decreases exponentially from the junction. This leads to the exponential weighting

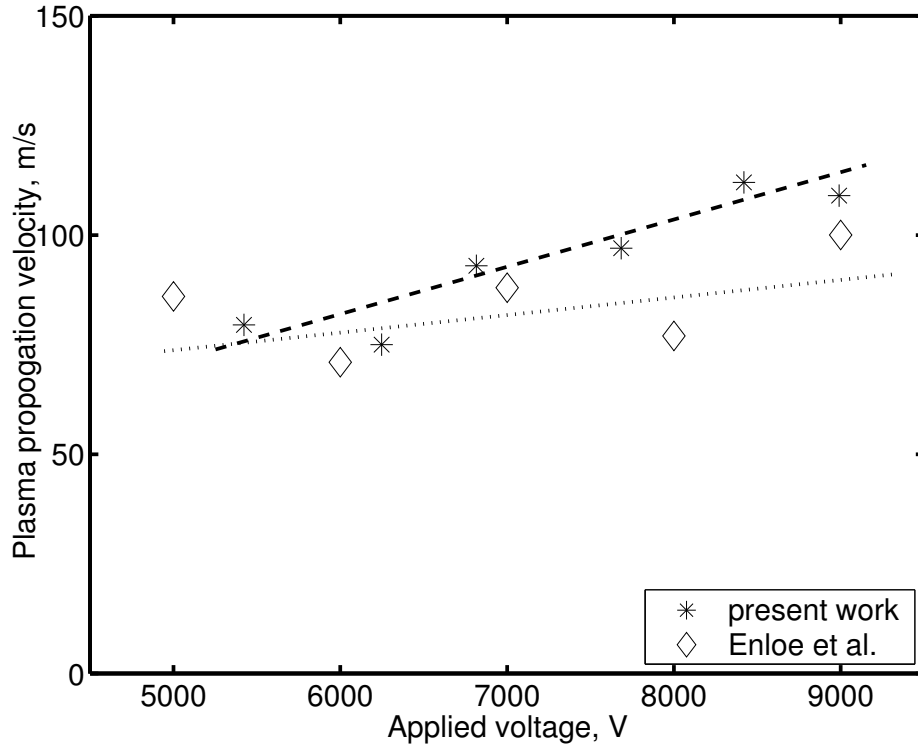


Figure 2.6. Plasma sweep velocity as function of applied voltage amplitude.

we have used in estimating the spatial dependence of the body force in our DNS simulations [47, 48, 76].

Of particular interest is the velocity with which the plasma sweeps over the encapsulated electrode. This can be determined from the slope, $d(\text{position})/dt$, of the left edge of the light-emission surfaces. This is shown in Figure 2.6 for a range of applied voltage amplitudes at a fixed a.c. frequency (5 kHz). The result of this work agrees with the previous result of Enloe *et al.* [20]. Similar information can be determined from the lumped element model that will be discussed later.

Another interesting characteristic that we can obtain from the light emission space-time surface is the maximum extent of the plasma. It is shown in Figure 2.7

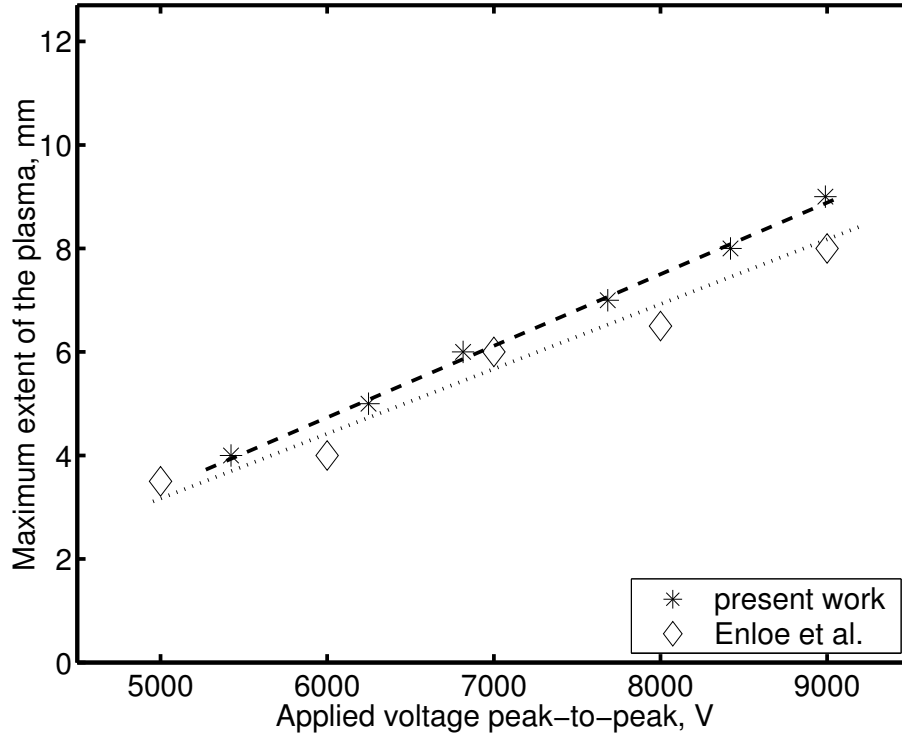


Figure 2.7. Maximum plasma extent as function of applied voltage amplitude.

as function of the applied voltage amplitude along with the previously published results of Enloe *et al.* [20]. It was observed to depend strongly on the applied voltage magnitude. This result is very important for the design of the plasma actuator. On one hand, the plasma does not extend beyond the end of the encapsulated electrode, and on the other hand, at low applied voltage amplitudes the plasma does not extend far, and covers only part of the covered electrode.

A set of experiments has been run at the constant applied voltage amplitude for a range of a.c. frequencies to find the dependence of the SDBD discharge characteristics on the applied frequency. For these experiments, the voltage across the plasma actuator was kept at $V_{app} = 5$ kV, and the a.c. frequency was changed in

the range of 5 – 11 kHz. The contour lines of the measured plasma light emission are shown in Figures 2.8 - 2.14. results from these contours are presented in terms of the propagation velocity and plasma extent in Figures 2.15 and 2.16, respectively. We notice, that the maximum extent of the plasma does not change with frequency, as shown in Figure 2.16. This also means that the plasma propagation velocity would increase with a.c. frequency because at high frequencies, the plasma has less time during the a.c. period to expand to the same extent as at low frequency. These results are shown in Figure 2.15.

A set of experiments has been run with the double-slit extension tube removed from the PMT to collect all of the light emitted by the SDBD. The results for a range of a.c. frequencies at a fixed voltage (5 kV) are shown in Figure 2.17. The results for a range of applied voltage amplitudes at a fixed a.c. frequency (5 kHz) are shown in Figure 2.18. The light intensity on this plot is represented by the PMT signal amplitude generated in the photomultiplier.

Figure 2.17 shows the total light emission from an SDBD plasma discharge in the whole a.c. period. It may be noticed that there is a maximum of the total light emission at 6 - 7 kHz. This may be assumed to be the optimal frequency for the plasma actuator operation.

Figure 2.18 shows the total amount of the emitted light in the whole a.c. period and the light in the first and second halves separately as a function of the applied a.c. voltage (peak-to-peak). It is clear that the second half of the a.c. period has illumination levels that are lower than the other half period across the full range of voltages examined. Drawn for reference is the line corresponding to $V_{app}^{7/2}$. Previous measurements by Enloe *et al.* [20] had shown a proportionality of the thrust produced by a plasma actuator as $V_{app}^{7/2}$. Later, Post [61] observed that the

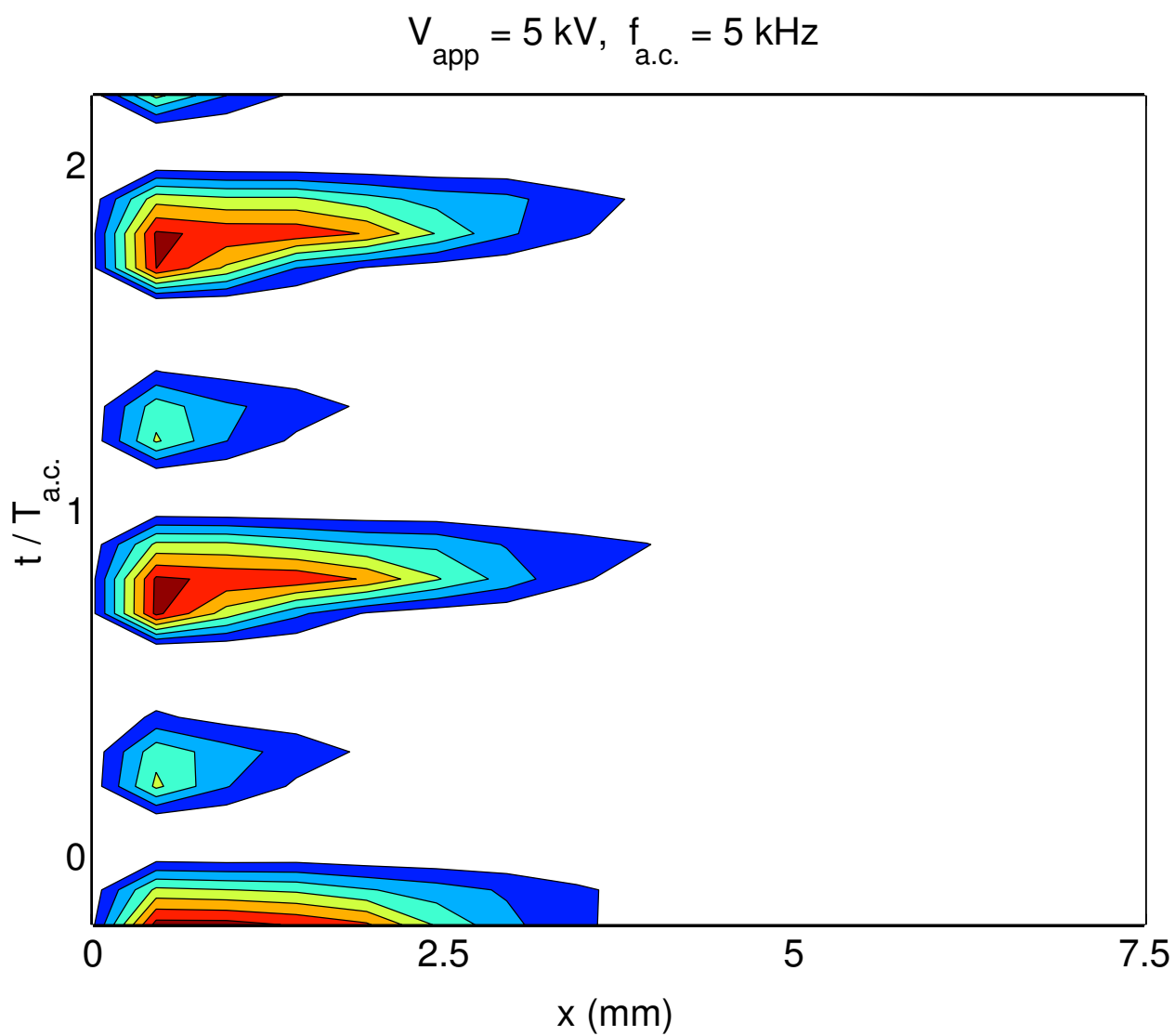


Figure 2.8. Space-time variation of the measured plasma light emission for SDBD plasma actuator at $V_{app} = 5 \text{ kV}$ and $f_{a.c.} = 5 \text{ kHz}$.

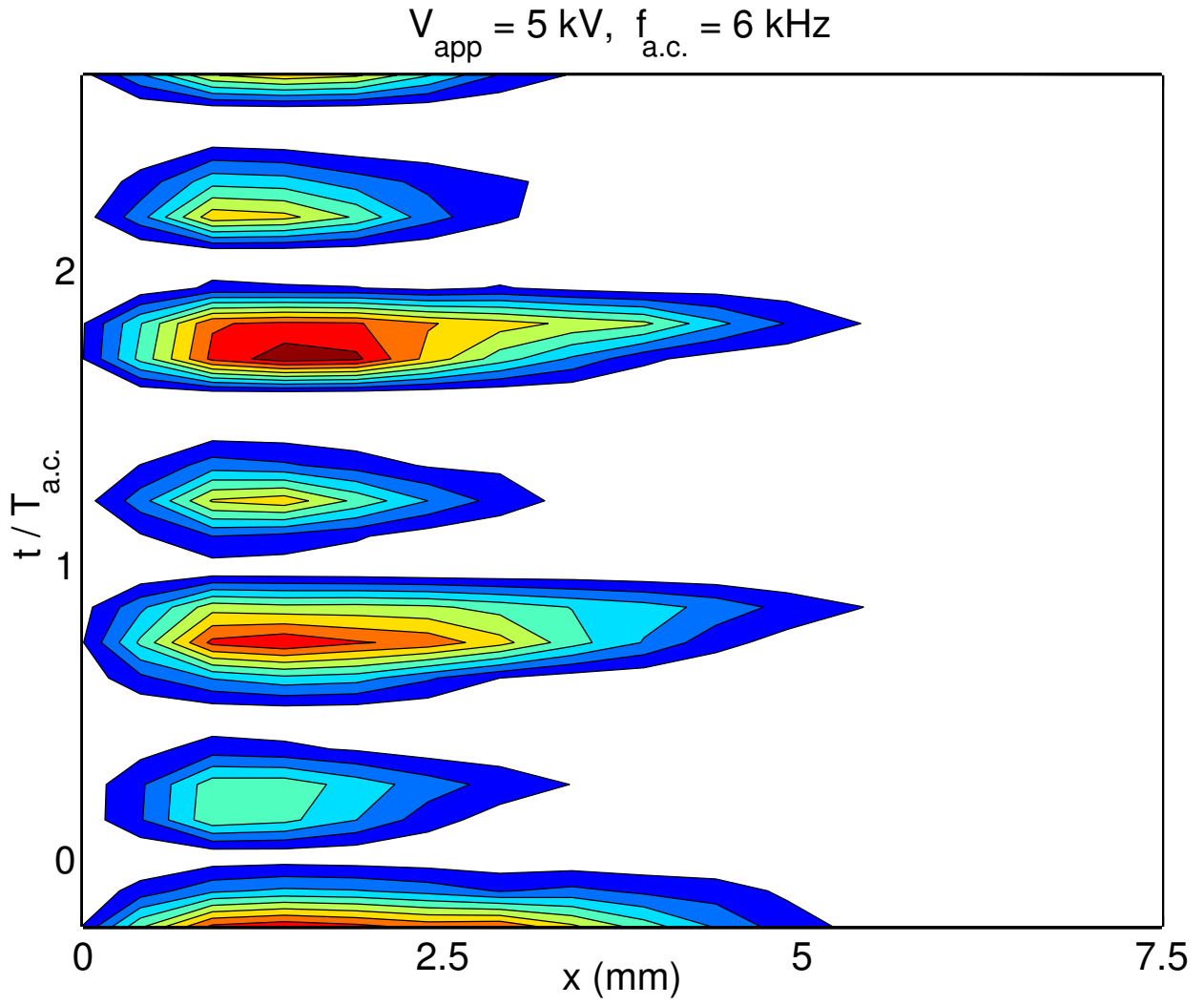


Figure 2.9. Space-time variation of the measured plasma light emission for SDBD plasma actuator at $V_{app} = 5 \text{ kV}$ and $f_{a.c.} = 6 \text{ kHz}$.

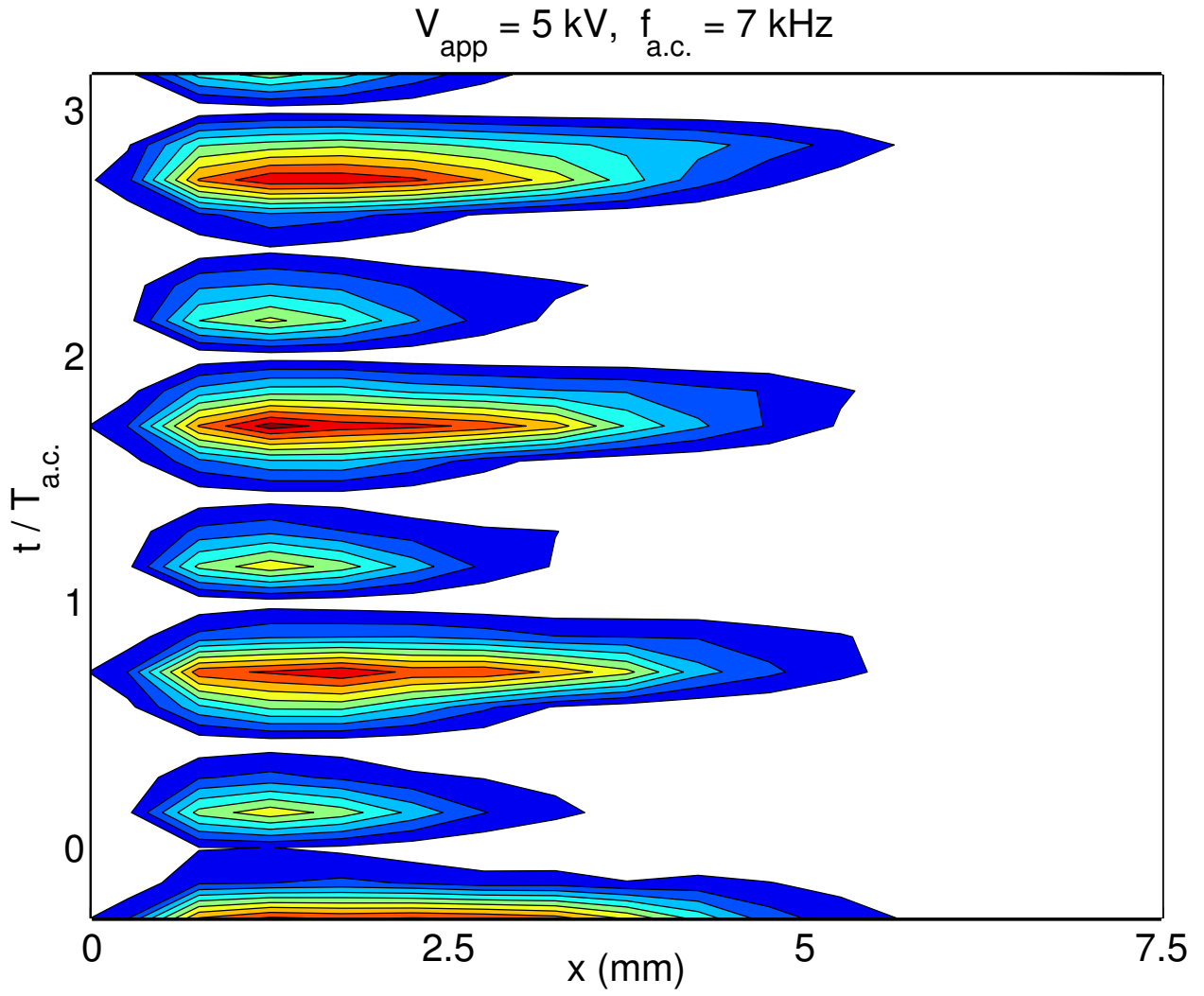


Figure 2.10. Space-time variation of the measured plasma light emission for SDBD plasma actuator at $V_{app} = 5 \text{ kV}$ and $f_{a.c.} = 7 \text{ kHz}$.

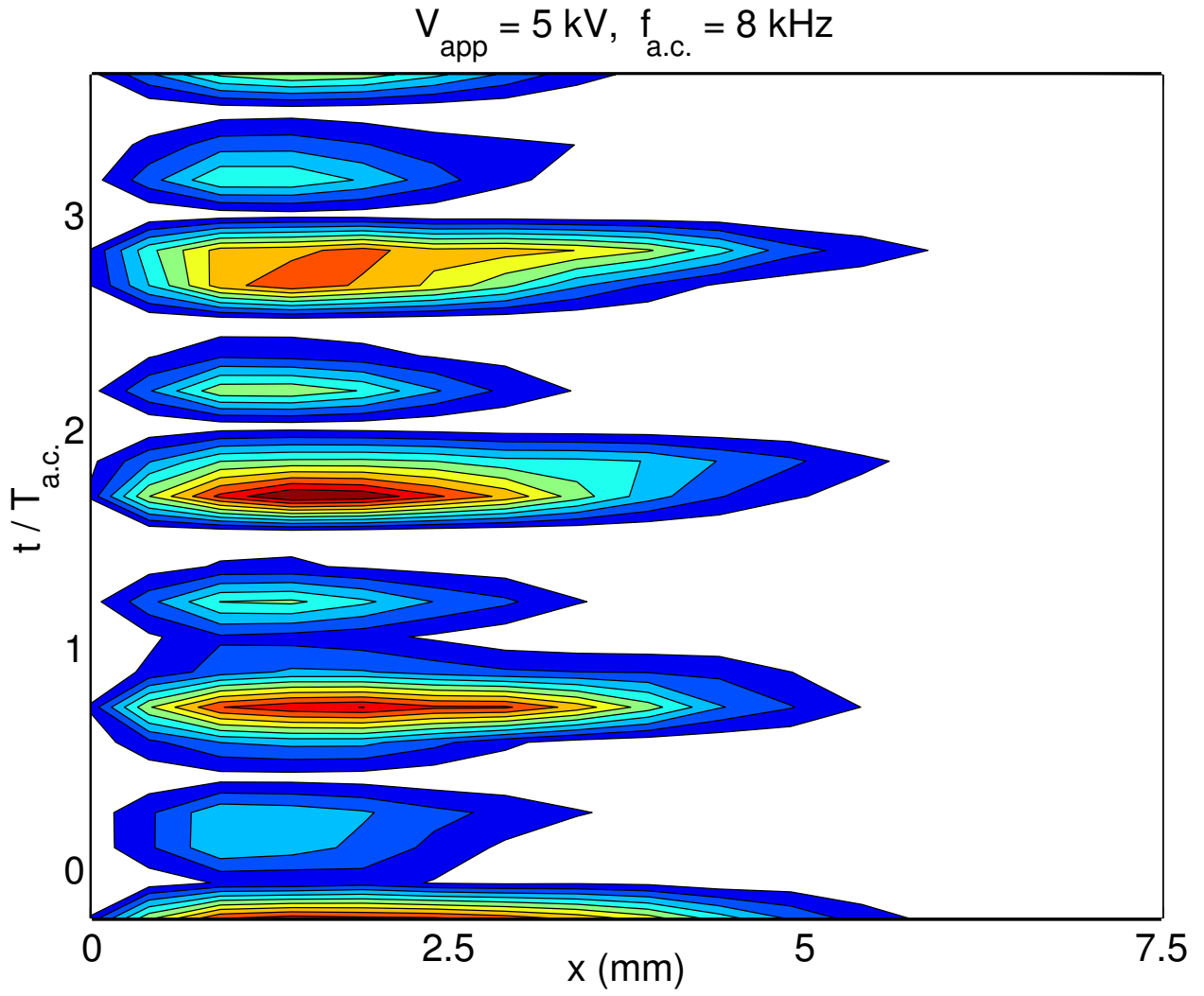


Figure 2.11. Space-time variation of the measured plasma light emission for SDBD plasma actuator at $V_{app} = 5 \text{ kV}$ and $f_{a.c.} = 8 \text{ kHz}$.

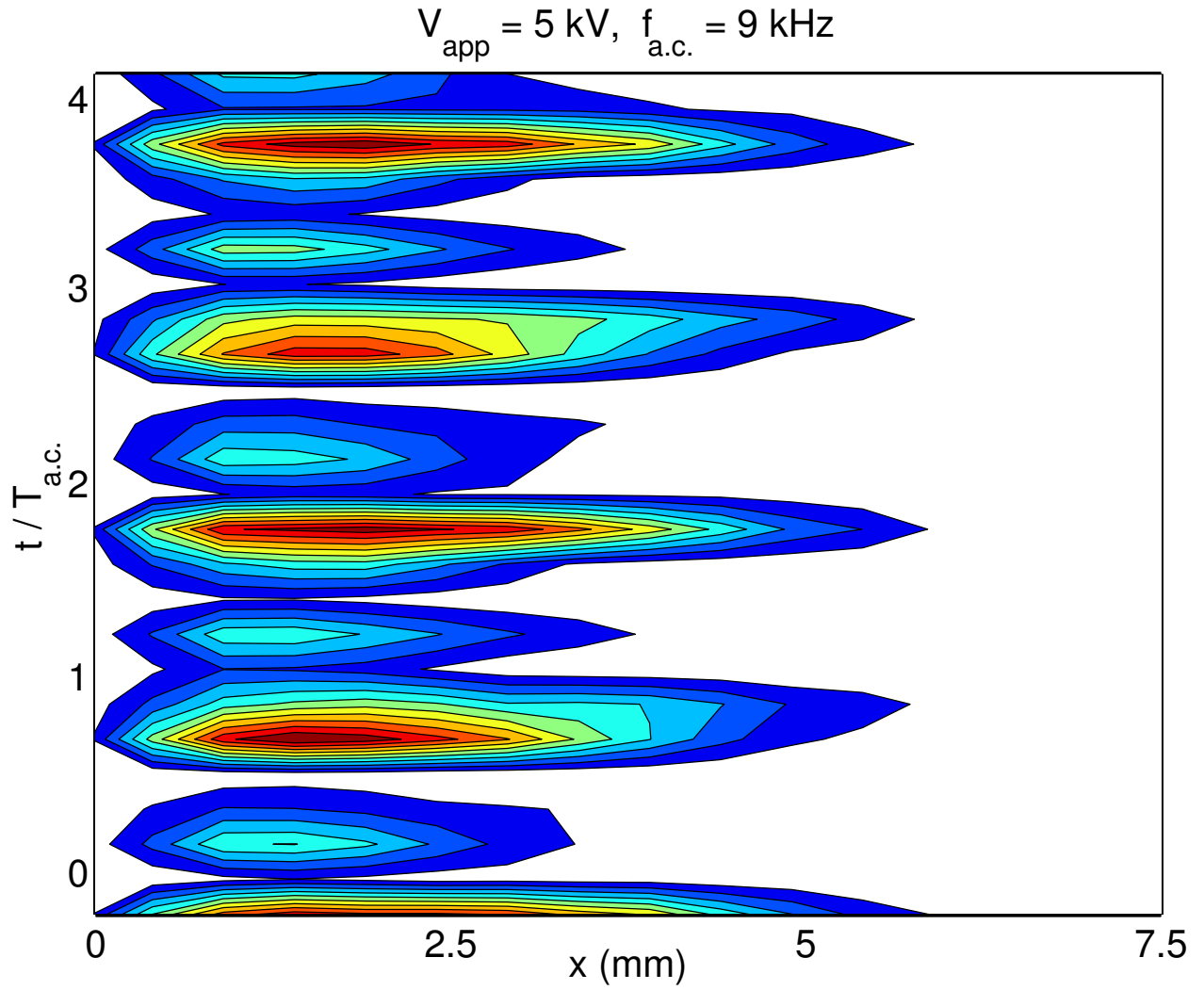


Figure 2.12. Space-time variation of the measured plasma light emission for SDBD plasma actuator at $V_{app} = 5 \text{ kV}$ and $f_{a.c.} = 9 \text{ kHz}$.

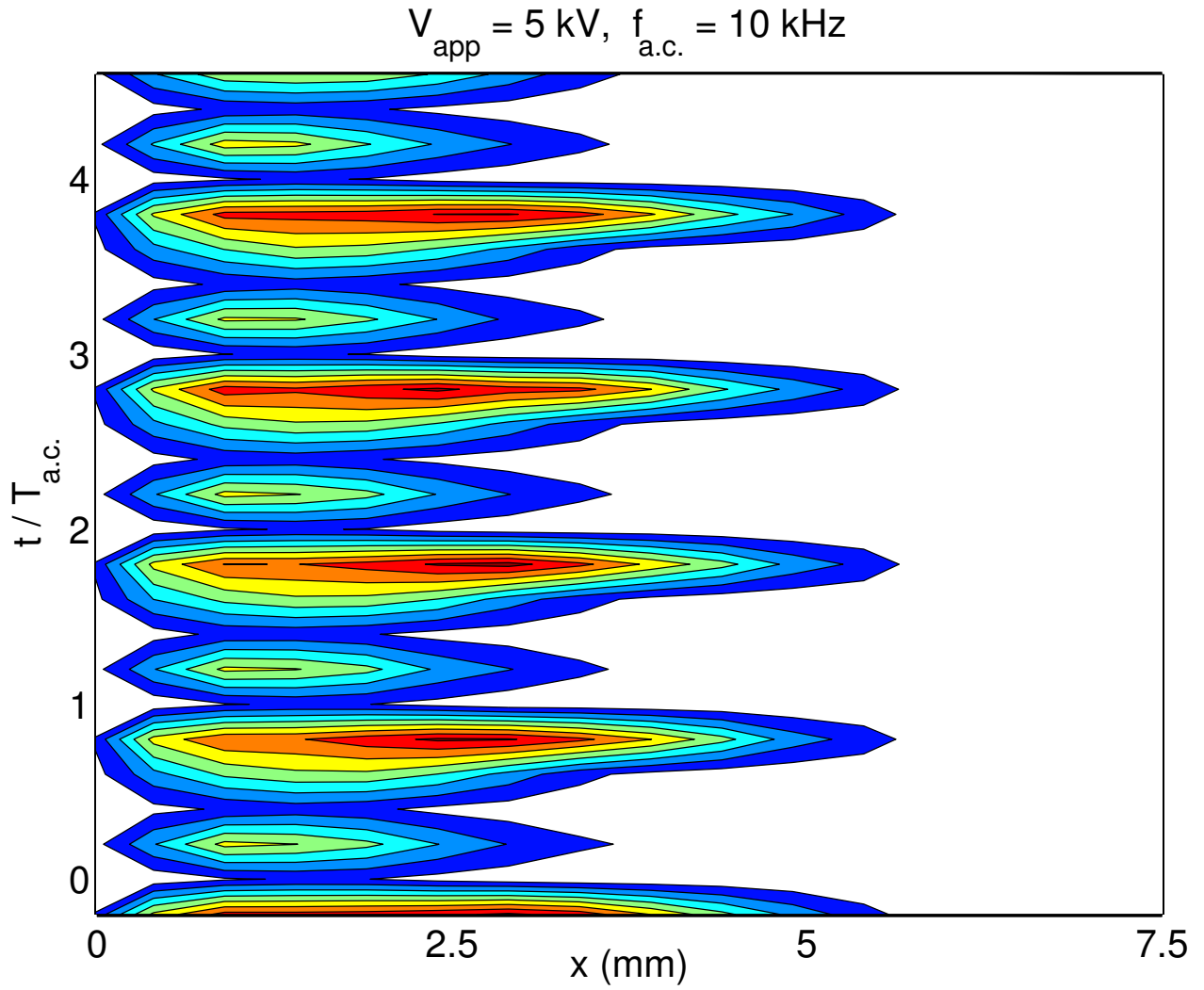


Figure 2.13. Space-time variation of the measured plasma light emission for SDBD plasma actuator at $V_{app} = 5 \text{ kV}$ and $f_{a.c.} = 10 \text{ kHz}$.

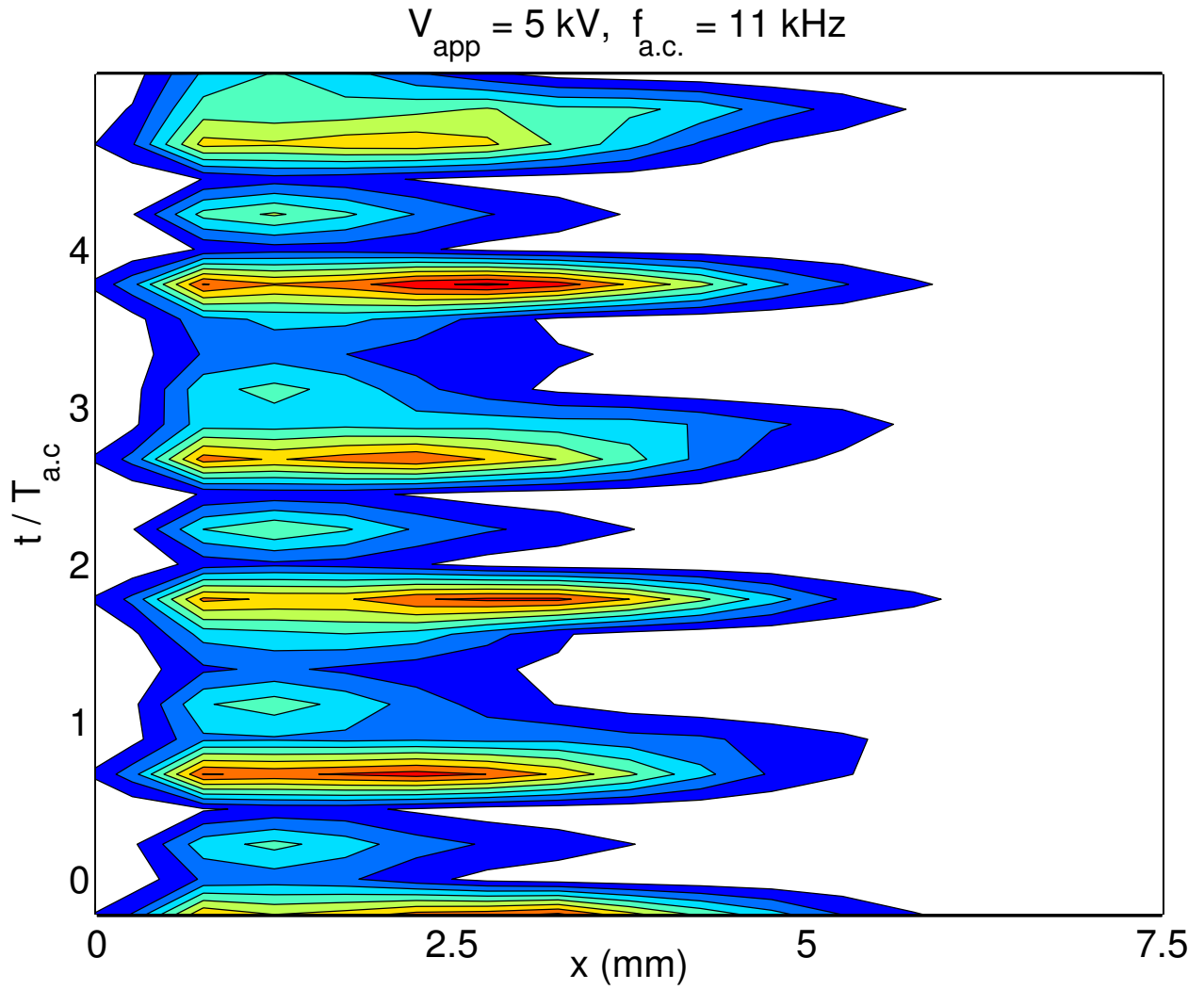


Figure 2.14. Space-time variation of the measured plasma light emission for SDBD plasma actuator at $V_{\text{app}} = 5 \text{ kV}$ and $f_{\text{a.c.}} = 11 \text{ kHz}$.

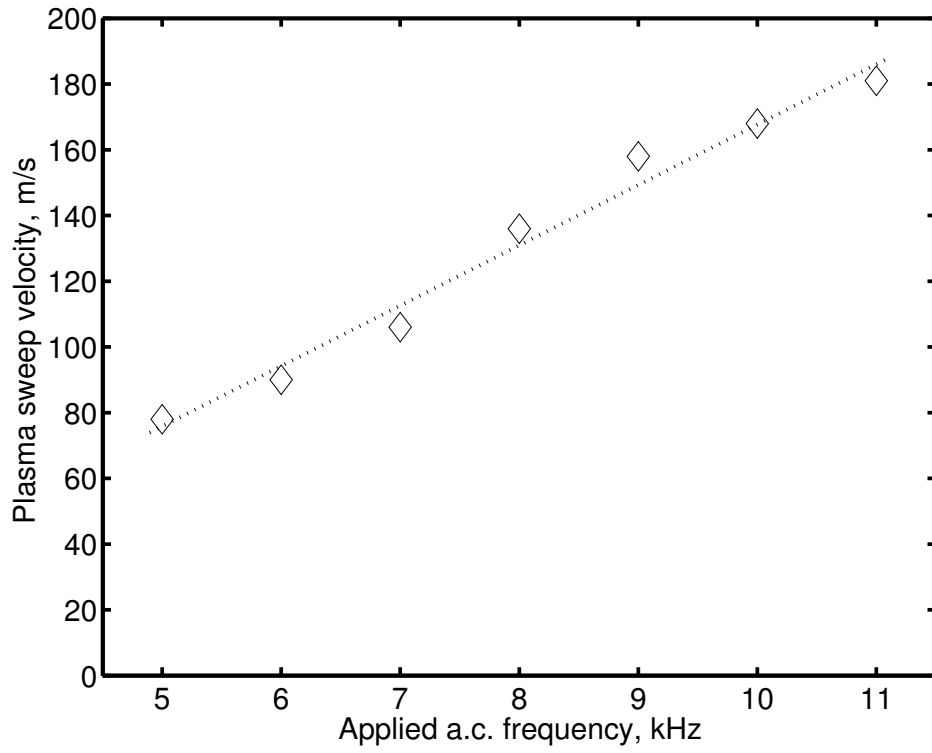


Figure 2.15. Plasma sweep velocity as function of applied a.c. frequency.

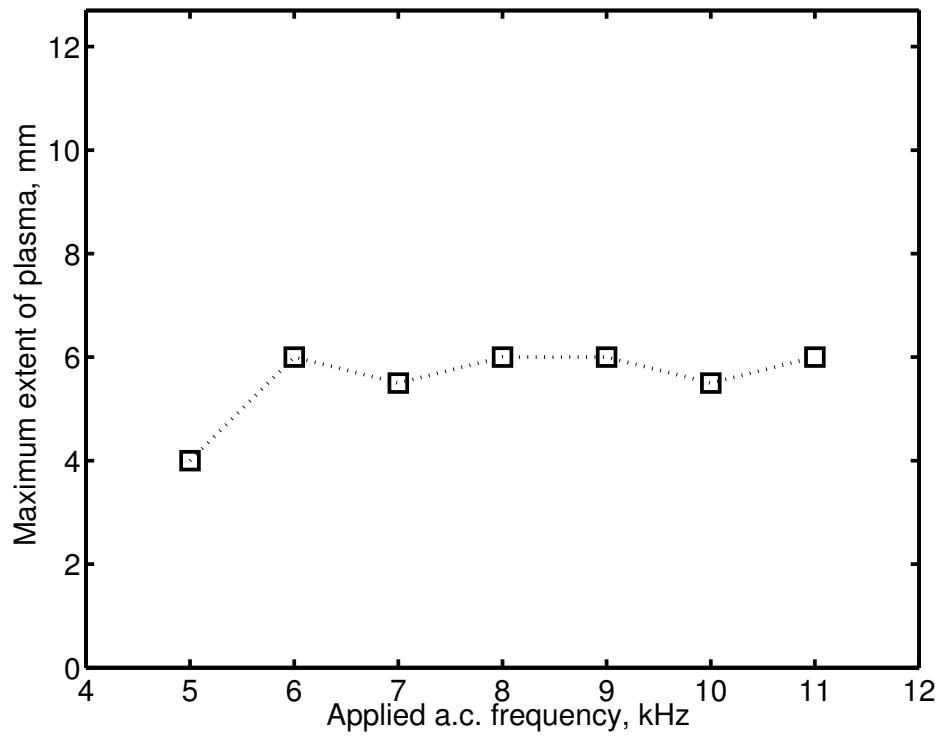


Figure 2.16. Maximum extent of the plasma as function of applied a.c. frequency.

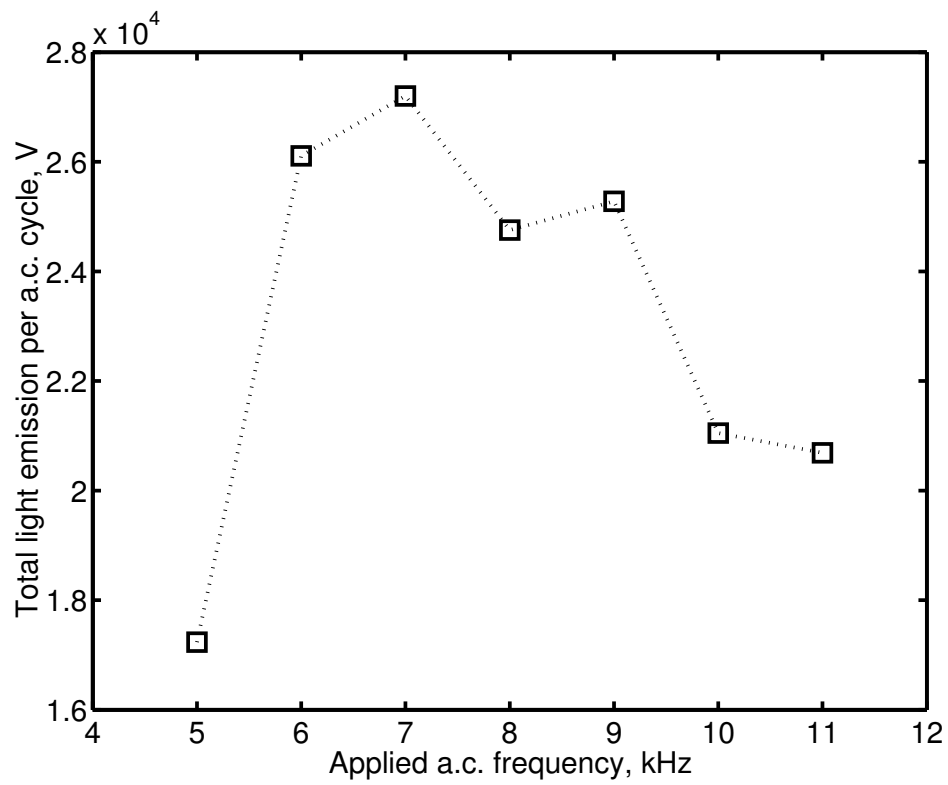


Figure 2.17. Total light emission for SDBD plasma actuator as function of applied a.c. frequency.

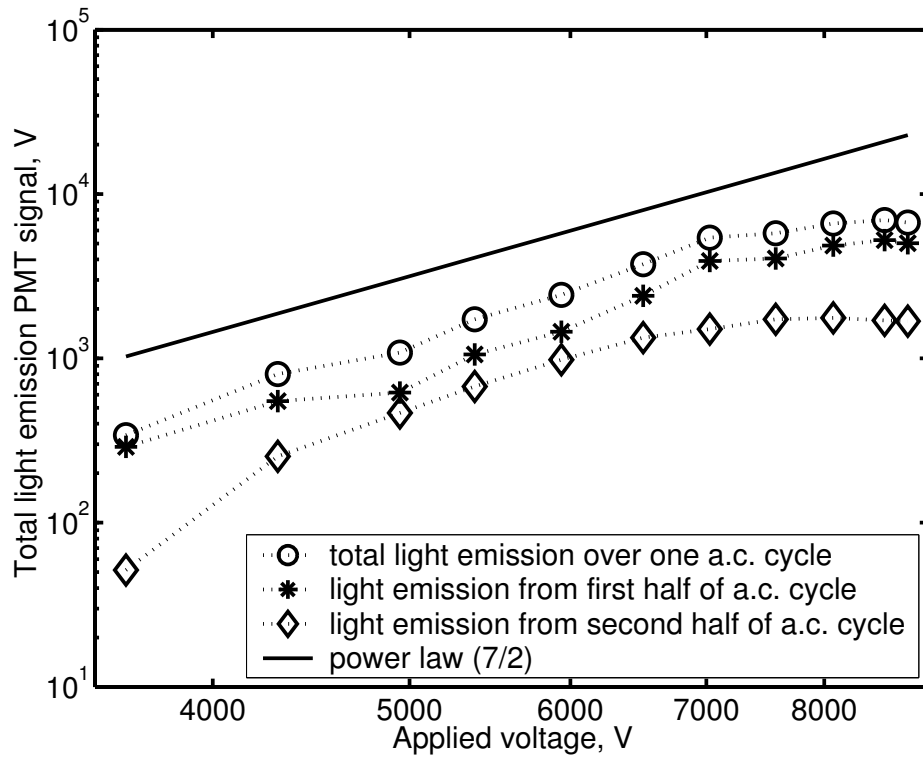


Figure 2.18. Total light intensity from the plasma actuator as function of applied voltage amplitude.

velocity maximum produced by a plasma actuator also was proportional to $V_{app}^{7/2}$. The light intensity change with voltage in Figure 2.18 indicates that at least up to a voltage of approximately 7 kV, the variation is proportional to $V_{app}^{7/2}$. The deviation at the higher voltage may be the result of limited size of the covered electrode which is insufficient to hold the charge build-up in the a.c. cycle.

Since the light intensity had been shown to correlate with current, this would indicate that the dissipated power of the plasma has the same proportionality to the voltage. Again a comparison of the plasma model behavior described in Chapter 4 to these results presented here will be made later in the thesis.

CHAPTER 3

ELECTRO-STATIC MODEL

3.1 Mathematical and Numerical Formulation

The first approach to explain the behavior of the plasma actuator is the electro-static model, described in this chapter. It is based on the assumption of different time scales that play different roles in the physics of the plasma actuator.

The characteristic velocities of the fluid transport of interest are on the order of 10-100 m/s. The process of plasma formation is characterized by the electron velocity in the plasma which is of the order of 10^5 - 10^6 m/s based on an electron temperature of 1000-10000 K [64]. This significant difference in the characteristic velocity time scales allows one to decouple the problem into separate parts associated with (1) the plasma body force formation and (2) the fluid flow response.

In this chapter, the governing equations for the electro-static problem will be formulated first. The equation for the plasma body force will then be derived based on the solution of the electro-statics. Finally, the equations of the flow problem will be presented.

The equations will be solved numerically in this chapter. The other part in this chapter deals with the numerical formulation and solution approach.

3.1.1 Electro-static Model

3.1.1.1 Governing equations for electro-static problem and body force

The plasma is an ionized quasi-neutral gas. In the general case, the system can be represented by a set of four Maxwell's equations given by

$$\begin{aligned}
 \oint_L \vec{H} d\vec{l} &= \int_S \left(\vec{j} + \frac{\partial \vec{D}}{\partial t} \right) d\vec{S}, \\
 \oint_L \vec{E} d\vec{l} &= - \int_S \frac{\partial \vec{B}}{\partial t} d\vec{S}, \\
 \oint (\vec{D} d\vec{S}) &= \int \rho_c dV, \\
 \oint (\vec{B} d\vec{S}) &= 0,
 \end{aligned} \tag{3.1}$$

where \vec{H} is the magnetic field strength, \vec{B} is the magnetic induction, \vec{E} is the electric field strength, \vec{D} is the electric induction, \vec{j} is the electric current, and ρ_c is the charge density, while L is the contour of integration, S is the bounding surface of the volume V . These Maxwell's equations (3.1) can be rewritten in differential form as

$$\begin{aligned}
 \text{curl} \vec{H} &= \vec{j} + \frac{\partial \vec{D}}{\partial t}, \\
 \text{curl} \vec{E} &= - \frac{\partial \vec{B}}{\partial t}, \\
 \text{div} \vec{D} &= \rho_c, \\
 \text{div} \vec{B} &= 0.
 \end{aligned} \tag{3.2}$$

It can be assumed that the charges in the plasma have sufficient amount of time to redistribute themselves in the region and the whole system is quasi-steady. In

this case, the electric current, \vec{j} , the magnetic field, \vec{H} , and the magnetic induction, \vec{B} , are all equal to zero. In addition the time derivatives of the electric induction, $\frac{\partial \vec{D}}{\partial t}$, and the magnetic induction, $\frac{\partial \vec{B}}{\partial t}$ are equal to zero. With this simplification, only one of the Maxwell's equations is left (3.2) to describe the given system of charges with charge density ρ_c , that is

$$\text{div} \vec{D} = \rho_c. \quad (3.3)$$

The vector of electric induction, \vec{D} , is related to a vector of electric field strength, \vec{E} , through the dielectric coefficient, ε , as

$$\vec{D} = \varepsilon \vec{E}. \quad (3.4)$$

The dielectric coefficient is a general property of the media. By definition, if an electric potential, φ , is known as a function of space coordinates then it is possible to compute an electric field strength, \vec{E} , by

$$\vec{E} = -\vec{\nabla} \varphi. \quad (3.5)$$

Substituting equations (3.5) and (3.4) into equation 3.3 gives the following

$$\nabla(\varepsilon \nabla \varphi) = -\frac{\rho_c}{\varepsilon_0}. \quad (3.6)$$

To examine the behavior of the charges in the electric field, we consider a simple case when the electric field is acting along some direction s only. Let us suppose that the electric field is acting on the charges as shown on Figure 3.1. In this case, the equation of the motion of the plasma gas can be written as

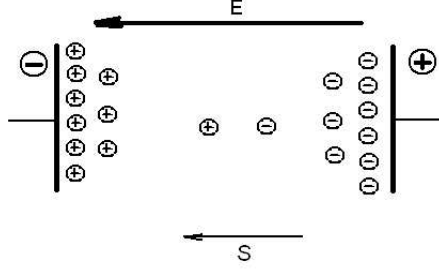


Figure 3.1. One-dimensional electric field acting on the charges.

$$mn \left[\frac{\partial \vec{u}_p}{\partial t} + (\vec{u} \cdot \vec{\nabla}) \vec{u} \right]_s = qn \vec{E} - \frac{\partial p}{\partial s}, \quad (3.7)$$

where m is the mass of the ion particle, n is the number of the particles in the plasma gas, u_p is the velocity of the plasma gas, q is the charge of the particle, and p is the pressure of the plasma gas. Ignoring the diffusion processes and assuming that the system is in steady state ($\frac{\partial}{\partial t} = 0$), and that velocity gradients can be ignored, the left side of the equation (3.7) vanishes. Substituting for pressure the gradient ∇p which for an isothermal gas, $\nabla p = k_b T \nabla n$, where k_b is the Boltzmann's constant, T is the temperature of the plasma gas, and n is the number of the particles in the plasma gas, we obtain

$$qnE = k_b T \frac{\partial n}{\partial s}. \quad (3.8)$$

For the plasma under consideration, the ions lose only one electron and have the charge $q = -e$, where e is the charge of the electron. Applying equation (3.5) to the one-dimensional electric field, $E = -\frac{\partial \varphi}{\partial s}$, equation (3.8) becomes

$$e \frac{\partial \varphi}{\partial s} = \frac{k_b T}{n} \frac{\partial n}{\partial s}. \quad (3.9)$$

The solution of equation 3.9 is the Boltzmann relation

$$n = n_0 \exp\left(\frac{e\varphi}{k_b T}\right), \quad (3.10)$$

where n_0 is the number of the molecules that are separated into ions and electrons by the electric field, which is the so called background plasma density.

It can be seen from equation (3.10) that the charged particles have a larger concentration in the regions of the high electric potential. According to this equation, their density decays exponentially. Without loss of generality, these results can be extended to the two-dimensional case.

The net charge density at any point in plasma is defined as the difference between the net positive charge produced by ions and the net negative charge of electrons. The difference can be related to the local electric potential, φ , by the Boltzmann relation (3.10). Assuming a quasi-steady state with a time scale long enough for the charges to redistribute themselves, we obtain

$$\rho_c = e(n_i - n_e) \approx -en_0 \left(\frac{e\varphi}{kT_i} + \frac{e\varphi}{kT_e} \right), \quad (3.11)$$

where T_i and T_e are temperatures of ion and electron species, respectively.

Substituting the equation for the charge density (3.11) into the Maxwell's equation (3.6), leads to the electro-static equation for this problem namely,

$$\nabla(\varepsilon \nabla \varphi) = \frac{1}{\lambda_D^2} \varphi, \quad (3.12)$$

where λ_D is called the Debye length, which is the characteristic length for electrostatic shielding in a plasma. The Debye length is defined as

$$\lambda_D = \left[\frac{e^2 n_0}{\epsilon_0} \left(\frac{1}{kT_i} + \frac{1}{kT_e} \right) \right]^{-\frac{1}{2}}. \quad (3.13)$$

The free charges in the plasma are shielded out in a distance given by the Debye length (3.13). The Coulomb force between the particles in a plasma (interaction between oppositely charged particles) is thus shielded by the mobility of free charges, and so is reduced in range from ∞ to $\sim \lambda_D$. The higher the temperature of the particles, the more mobility they have, and the greater is their range. When the density n_e of electrons is high, the Debye length shrinks.

The Debye shielding is valid if there are enough particles in the charge cloud. The criteria for this is the dimensionless plasma parameter, Λ , that characterizes unmagnetized plasma systems, defined as

$$\Lambda = \frac{4}{3} \pi \lambda_D^3 n_e. \quad (3.14)$$

If the plasma parameter is

$$\Lambda \gg 1, \quad (3.15)$$

then it means that the plasma is weakly-coupled, and the Debye shielding is valid. For the plasmas of consideration, the Debye length is approximately 0.00017 m and the density of the charged particles is on the order of 10^{16} particles/m³ [64]. In this case, the criteria is $\Lambda = 3.5 \cdot 10^5$. Therefore the equation (3.15) is satisfied, indicating that the assumption of the Debye shielding is true.

The equation of electro-statics is solved in the domain shown in Figure 3.3. The value of the electric potential is set on the electrodes

$$\varphi |_{\text{electrodes}} = \pm\varphi_0. \quad (3.16)$$

The boundary conditions on the outer boundaries model the condition at the “infinity”, where the electric potential, φ , is equal to zero

$$\varphi |_{\text{outer boundary}} = 0. \quad (3.17)$$

The solution of the electro-static equation (3.12) is the electric potential φ . The electric field strength E is related to φ through Eq.(3.5). If we assume a value for λ_D , then ρ_c can be found as

$$\rho_c = -\frac{\varepsilon_0}{\lambda_D^2}\varphi. \quad (3.18)$$

Because there is an electric field in the plasma in regions where there is also a net charge density, there will be a force on plasma. The electric force acting on a single charge is given by Lorentz equation,

$$\vec{f}_b^* = q\vec{E}. \quad (3.19)$$

Therefore the force density that acts on a continuous system of charges with charge density ρ_c , can be written as

$$\vec{f}_b^* = \rho_c\vec{E} = -\left(\frac{\varepsilon_0}{\lambda_D^2}\right)\varphi\vec{E}. \quad (3.20)$$

This body force (3.20) is a body force per volume of plasma. This body force is the basis of the plasma actuator effect on neutral air. We note that it is a vector which acts in the vector direction of the electric field.

3.1.1.2 Numerical Formulation of Electro-static Problem

The governing equations for the electro-static problem (3.12) are discretized using the standard centered second order scheme.

We rewrite the governing equation (3.12) as

$$\varepsilon \nabla^2 \varphi + \nabla \varepsilon \nabla \varphi = \frac{1}{\lambda_D^2} \varphi. \quad (3.21)$$

A standard definition of gradient ($\vec{\nabla}$) function is

$$\vec{\nabla} = \frac{\partial}{\partial x} \hat{i} + \frac{\partial}{\partial y} \hat{j} + \frac{\partial}{\partial z} \hat{k}, \quad (3.22)$$

which gives us the following form of the governing equation:

$$\varepsilon \frac{\partial^2 \varphi}{\partial x^2} + \varepsilon \frac{\partial^2 \varphi}{\partial y^2} + \frac{\partial \varepsilon}{\partial x} \frac{\partial \varphi}{\partial x} + \frac{\partial \varepsilon}{\partial y} \frac{\partial \varphi}{\partial y} = \frac{1}{\lambda_D^2} \varphi. \quad (3.23)$$

To solve the governing equation in a mathematical plane on a uniform grid (ξ, η) , the coordinate transformation is applied

$$\xi = \xi(x), \quad (3.24)$$

$$\eta = \eta(y).$$

In this case, the governing equation becomes

$$\varepsilon \xi_x^2 \frac{\partial^2 \varphi}{\partial \xi^2} + \varepsilon \eta_y^2 \frac{\partial^2 \varphi}{\partial \eta^2} + \left(\varepsilon \xi_{xx} + \frac{\partial \varepsilon}{\partial \xi} \xi_x^2 \right) \frac{\partial \varphi}{\partial \xi} + \left(\varepsilon \eta_{yy} + \frac{\partial \varepsilon}{\partial \eta} \eta_y^2 \right) \frac{\partial \varphi}{\partial \eta} = \frac{1}{\lambda_D^2} \varphi. \quad (3.25)$$

For an approximation of the first and second derivatives on a uniform grid we use centered differences:

$$\begin{aligned} \frac{\partial \varphi}{\partial \xi} &= \frac{\varphi_{i+1,j} - \varphi_{i-1,j}}{2\Delta\xi}, \\ \frac{\partial \varphi}{\partial \eta} &= \frac{\varphi_{i,j+1} - \varphi_{i,j-1}}{2\Delta\eta}, \\ \frac{\partial^2 \varphi}{\partial \xi^2} &= \frac{\varphi_{i+1,j} - 2\varphi_{i,j} + \varphi_{i-1,j}}{\Delta\xi^2}, \\ \frac{\partial^2 \varphi}{\partial \eta^2} &= \frac{\varphi_{i,j+1} - 2\varphi_{i,j} + \varphi_{i,j-1}}{\Delta\eta^2}. \end{aligned} \quad (3.26)$$

Finally, we get an equation in the form:

$$A_{i+1,j} \varphi_{i+1,j} + B_{i-1,j} \varphi_{i-1,j} + C_{i,j+1} \varphi_{i,j+1} + D_{i,j-1} \varphi_{i,j-1} = E_{i,j} \varphi_{i,j}, \quad (3.27)$$

where numerical coefficients A , B , C , D and E are the known coefficients of the grid transformation and can be computed at every point of the domain before the

iteration procedure:

$$A = \frac{\varepsilon \xi_x^2}{\Delta \xi^2} + \frac{\varepsilon \xi_{xx}}{2\Delta \xi} + \frac{\frac{\partial \varepsilon}{\partial \xi} \xi_x^2}{2\Delta \xi}, \quad (3.28)$$

$$B = \frac{\varepsilon \xi_x^2}{\Delta \xi^2} - \frac{\varepsilon \xi_{xx}}{2\Delta \xi} - \frac{\frac{\partial \varepsilon}{\partial \xi} \xi_x^2}{2\Delta \xi}, \quad (3.29)$$

$$C = \frac{\varepsilon \eta_y^2}{\Delta \eta^2} + \frac{\varepsilon \eta_{yy}}{2\Delta \eta} + \frac{\frac{\partial \varepsilon}{\partial \eta} \eta_y^2}{2\Delta \eta}, \quad (3.30)$$

$$D = \frac{\varepsilon \eta_y^2}{\Delta \eta^2} - \frac{\varepsilon \eta_{yy}}{2\Delta \eta} - \frac{\frac{\partial \varepsilon}{\partial \eta} \eta_y^2}{2\Delta \eta}, \quad (3.31)$$

$$E = 2\frac{\varepsilon \xi_x^2}{\Delta \xi^2} + 2\frac{\varepsilon \eta_y^2}{\Delta \eta^2} + \frac{1}{\lambda_D^2}. \quad (3.32)$$

The boundary conditions for this problem, given by Equations 3.16 and 3.17, become

$$\begin{aligned} \varphi |_{\xi=(-1,0),\eta=0} &= 1, \\ \varphi |_{\xi=(0,1),\eta=0} &= -1, \\ \varphi |_{\xi=-2,\eta=(-2,2)} &= 0, \\ \varphi |_{\xi=2,\eta=(-2,2)} &= 0, \\ \varphi |_{\xi=(-2,2),\eta=-2} &= 0, \\ \varphi |_{\xi=(-2,2),\eta=2} &= 0, \end{aligned} \quad (3.33)$$

The equation (3.27) is then solved using the standard point Gauss-Seidel procedure.

3.1.2 Flow Problem

3.1.2.1 Governing Equations for Flow Problem

The governing equations for the fluid flow problem that we have selected are the unsteady 2-D Navier-Stokes equations in primitive variables. In dimensional form these are given by

$$\begin{aligned} u_t^* + u^* \frac{\partial u^*}{\partial x^*} + v^* \frac{\partial u^*}{\partial y^*} &= -\frac{1}{\rho} \frac{\partial p^*}{\partial x^*} + \nu \left(\frac{\partial^2 u^*}{\partial x^{*2}} + \frac{\partial^2 u^*}{\partial y^{*2}} \right) + f_b^{(x)*}, \\ v_t^* + u^* \frac{\partial v^*}{\partial x^*} + v^* \frac{\partial v^*}{\partial y^*} &= -\frac{1}{\rho} \frac{\partial p^*}{\partial y^*} + \nu \left(\frac{\partial^2 v^*}{\partial x^{*2}} + \frac{\partial^2 v^*}{\partial y^{*2}} \right) + f_b^{(y)*}, \end{aligned} \quad (3.34)$$

where x and y are the Cartesian coordinates and $(*)$ denotes dimensional terms, and $f_b^{(x)*}$ and $f_b^{(y)*}$ are components of the body force in the x and y directions respectively. The body force, \vec{f}_b^* , comes into the equations on the right hand side as a solution of electro-static problem, point by point.

We define the stream function, ψ , as

$$\begin{aligned} u^* &= \frac{\partial \psi^*}{\partial y^*}, \\ v^* &= -\frac{\partial \psi^*}{\partial x^*}, \end{aligned} \quad (3.35)$$

and the vorticity, ω , as

$$\begin{aligned} \vec{\omega}^* &= \vec{\nabla} \cdot \vec{V}^* = \begin{vmatrix} \vec{i} & \vec{j} & \vec{k} \\ \frac{\partial}{\partial x^*} & \frac{\partial}{\partial y^*} & \frac{\partial}{\partial z^*} \\ u^* & v^* & w^* \end{vmatrix} = \left(\frac{\partial v^*}{\partial x^*} - \frac{\partial u^*}{\partial y^*} \right) \vec{k}, \\ \omega^* &= \omega_z^* = \frac{\partial v^*}{\partial x^*} - \frac{\partial u^*}{\partial y^*} = \frac{\partial^2 \psi^*}{\partial x^{*2}} + \frac{\partial^2 \psi^*}{\partial y^{*2}}. \end{aligned} \quad (3.36)$$

Transforming the governing equations (3.34) into the stream function-vorticity form, we obtain

$$\begin{aligned} \frac{\partial \omega^*}{\partial t^*} + \frac{\partial \psi^*}{\partial y^*} \frac{\partial \omega^*}{\partial x^*} + \frac{\partial \psi^*}{\partial x^*} \frac{\partial \omega^*}{\partial y^*} &= \nu \left(\frac{\partial^2 \omega^*}{\partial x^{*2}} + \frac{\partial^2 \omega^*}{\partial y^{*2}} \right) + \frac{\partial f_b^{(x)*}}{\partial y^*} - \frac{\partial f_b^{(y)*}}{\partial x^*}, \\ \frac{\partial^2 \psi^*}{\partial x^{*2}} + \frac{\partial^2 \psi^*}{\partial y^{*2}} &= -\omega^*. \end{aligned} \quad (3.37)$$

We nondimensionalize it using the free stream velocity, U_∞ , and characteristic length, L , as

$$\begin{aligned} x &= \frac{x^*}{L}, \quad y = \frac{y^*}{L}, \quad t = \frac{t^*}{L/U_\infty}, \\ \omega &= \frac{U_\infty}{L} \omega^*, \quad \psi = LU_\infty \psi^*, \\ f^{(x)} &= f_b^{(x)*} \frac{L}{U_\infty^2}, \quad f^{(y)} = f_b^{(y)*} \frac{L}{U_\infty^2}. \end{aligned} \quad (3.38)$$

Finally, we obtain the stream function equation in nondimensional form,

$$\frac{\partial^2 \psi}{\partial x^2} + \frac{\partial^2 \psi}{\partial y^2} = -\omega, \quad (3.39)$$

and the vorticity equation,

$$\frac{\partial \omega}{\partial t} + \frac{\partial \psi}{\partial y} \frac{\partial \omega}{\partial x} + \frac{\partial \psi}{\partial x} \frac{\partial \omega}{\partial y} = \frac{1}{Re} \left(\frac{\partial^2 \omega}{\partial x^2} + \frac{\partial^2 \omega}{\partial y^2} \right) + \frac{\partial f^{(x)}}{\partial y} - \frac{\partial f^{(y)}}{\partial x}. \quad (3.40)$$

These equations are discretized and solved numerically.

3.1.2.2 Boundary Conditions

The boundary condition on the stream function at the solid boundary is given by equation (3.52). Figure 3.2 shows the computational domain with for rigid

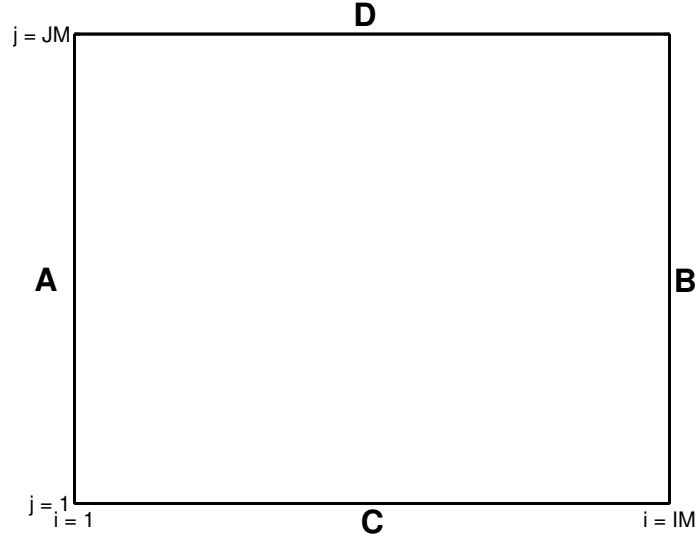


Figure 3.2. Rectangular computational domain with solid boundaries.

boundaries A, B, C, and D. In this section, the boundary conditions will be formulated for the boundary A, and this result will be extended to the other boundaries at B, C, and D.

Considering equation (3.39) for the stream function at point $(1, j)$, then

$$\left(\frac{\partial^2 \psi}{\partial x^2} + \frac{\partial^2 \psi}{\partial y^2} \right)_{1,j} = -\omega_{1,j}. \quad (3.41)$$

Along the surface, the stream function is constant, and its value is specified as $\psi_{1,j} = 0$. Then, along A,

$$\frac{\partial^2 \psi}{\partial y^2} \Big|_{1,j} = 0, \quad (3.42)$$

and equation (3.41) is then reduced to

$$\frac{\partial^2 \psi}{\partial x^2} \Big|_{1,j} = -\omega_{1,j}. \quad (3.43)$$

To obtain an expression for the second-order derivative in the equation above, we utilize a Taylor series expansion

$$\psi_{2,j} = \psi_{1,j} + \frac{\partial\psi}{\partial x} \Big|_{1,j} \Delta x + \frac{\partial^2\psi}{\partial x^2} \Big|_{1,j} \frac{(\Delta x)^2}{2} + \dots \quad (3.44)$$

Therefore along boundary A

$$v_{1,j} = -\frac{\partial\psi}{\partial x} \Big|_{1,j} = 0. \quad (3.45)$$

Therefore, the stream function at the point just above surface A is

$$\psi_{2,j} = \psi_{1,j} + \frac{\partial^2\psi}{\partial x^2} \Big|_{1,j} \frac{(\Delta x)^2}{2} + O(\Delta x)^3, \quad (3.46)$$

from which

$$\frac{\partial^2\psi}{\partial x^2} \Big|_{1,j} = \frac{2(\psi_{2,j} - \psi_{1,j})}{(\Delta x)^2} + O(\Delta x). \quad (3.47)$$

Substitution of equation (3.47) into equation (3.43) yields an expression for the vorticity at the surface A which is

$$\omega_{1,j} = \frac{2(\psi_{1,j} - \psi_{2,j})}{(\Delta x)^2}. \quad (3.48)$$

A similar procedure is used to derive the boundary conditions at boundaries B, C, and D. The appropriate expressions are, respectively,

$$\begin{aligned} \omega_{IM,j} &= -\frac{\partial^2\psi}{\partial x^2} \Big|_{IM,j} = \frac{2(\psi_{IM,j} - \psi_{IMM1,j})}{(\Delta x)^2}, \\ \omega_{i,1} &= -\frac{\partial^2\psi}{\partial y^2} \Big|_{i,1} = \frac{2(\psi_{i,1} - \psi_{i,2})}{(\Delta y)^2}, \\ \omega_{i,JM} &= -\frac{\partial^2\psi}{\partial y^2} \Big|_{i,JM} = \frac{2(\psi_{i,JM} - \psi_{i,JMM1})}{(\Delta y)^2}. \end{aligned} \quad (3.49)$$

As it was shown in [6], the first-order expression for $\omega_{i,1}$ often gives better results than higher-order expressions. Although higher order implementation of the boundary conditions in general will increase the accuracy of the solution, they often cause instabilities in high Reynolds number flows. Therefore we have elected to use the first-order expression given by equations 3.47 and 3.49.

3.1.2.3 Model Problem

Following the experiments by Post [61], in which plasma actuators were located on an inner surface of a closed box, we consider the flow in a closed box with no slip and no penetration conditions on all walls:

$$\begin{aligned} u_{\text{wall}}^* &= 0, \\ v_{\text{wall}}^* &= 0. \end{aligned} \tag{3.50}$$

After nondimensionalization, the boundary conditions become

$$\begin{aligned} u_{\text{wall}} &= 0, \\ v_{\text{wall}} &= 0. \end{aligned} \tag{3.51}$$

For the previously introduced stream function (3.35), the boundary conditions for the stream function on the rigid walls is

$$\psi = \text{Const} = 0, \tag{3.52}$$

and from the definition of the stream function it follows that on the walls,

$$\begin{aligned}\frac{\partial\psi}{\partial y} &= 0, \\ \frac{\partial\psi}{\partial x} &= 0,\end{aligned}\tag{3.53}$$

which can be written in a short form as

$$\frac{\partial\psi}{\partial\vec{n}} = 0,\tag{3.54}$$

where \vec{n} is a vector, normal to the wall.

The vorticity on the walls is computed numerically using ω and ψ values at interior points according to equations (3.48) and (3.49). The governing equations are temporal and therefore require initial conditions. The initial conditions for the model problem will be discussed in Section 3.3.

3.1.2.4 Numerical Formulation of Flow Problem

The vorticity transport equation (3.40) is discretized using Forward Time Central Space method. In this method the time derivative is approximated by a first-order forward difference expression whereas second-order central difference relations are used for the spatial derivatives.

For correct modeling of the convective terms, the use of an upwind differencing scheme is more appropriate [30]. Using the conservative form of the vorticity transport equation, the convective terms are approximated with forward and backward first-order differences on the nonuniform grid, while the diffusive terms are

approximated with second-order centered differences:

$$\begin{aligned}
& \frac{\omega_{i,j}^{n+1} - \omega_{i,j}^n}{\Delta t} + \frac{1}{2}(1 - \epsilon_x) \frac{u_{i+1,j}\omega_{i+1,j} - u_{i,j}\omega_{i,j}}{x_{i+1} - x_i} + \frac{1}{2}(1 + \epsilon_x) \frac{u_{i,j}\omega_{i,j} - u_{i-1,j}\omega_{i-1,j}}{x_i - x_{i-1}} \\
& + \frac{1}{2}(1 - \epsilon_y) \frac{v_{i,j+1}\omega_{i,j+1} - v_{i,j}\omega_{i,j}}{y_{j+1} - y_j} + \frac{1}{2}(1 + \epsilon_y) \frac{v_{i,j}\omega_{i,j} - v_{i,j-1}\omega_{i,j-1}}{y_j - y_{j-1}} \\
& = \frac{1}{Re} \frac{2}{(x_i - x_{i-1})^2 (\alpha_i^x + 1)} \left[\omega_{i-1,j} - \omega_{i,j} \left(\frac{1}{\alpha_i^x} + 1 \right) + \omega_{i+1,j} \left(\frac{1}{\alpha_i^x} \right) \right] \\
& + \frac{1}{Re} \frac{2}{(y_j - y_{j-1})^2 (\alpha_j^y + 1)} \left[\omega_{i,j-1} - \omega_{i,j} \left(\frac{1}{\alpha_j^y} + 1 \right) + \omega_{i,j+1} \left(\frac{1}{\alpha_j^y} \right) \right] \\
& + \frac{f_{i,j+1}^x - f_{i,j-1}^x}{y_{j+1} - y_{j-1}} - \frac{f_{i-1,j}^y - f_{i+1,j}^y}{x_{i+1} - x_{i-1}}, \tag{3.55}
\end{aligned}$$

where $\alpha_i^x = \frac{x_{i+1} - x_i}{x_i - x_{i-1}}$ and $\alpha_j^y = \frac{y_{j+1} - y_j}{y_j - y_{j-1}}$.

If u is positive, a backward approximation must be utilized. Thus, ϵ_x is set equal to one. If u is negative, a forward approximation is used and therefore ϵ_x is set equal to -1 . The same analogy is applied to v and the corresponding coefficient ϵ_y . The upwind formulation allows the information to be convected only to the points in the flow direction and, therefore, more appropriately models the physics of the problem.

The stream function equation that is given by equation (3.39) is classified as an elliptic equation. The point Gauss-Seidel formulation for this equation gives

$$\psi_{i,j}^{k+1} = \frac{1}{2(1 + \beta^2)} [(\Delta x)^2 \omega_{i,j}^k + \psi_k^{i+1,j} + \psi_{k+1}^{i-1,j} + \beta^2(\psi_k^{i,j+1} + \psi_{k+1}^{i,j-1})], \tag{3.56}$$

where $\beta = \frac{\Delta x}{\Delta y}$.

The numerical procedure consists of the following steps:

1. Specify initial values for ω and ψ at time $t = 0$;

2. Specify values for the body force, \vec{f}_b , in the domain, which are given as a solution of the electro-static problem;
3. Specify the convergence parameter (as defined in Chapter 3);
4. Solve the vorticity transport equation (3.55) for ω at each interior grid point at time $t + \Delta t$;
5. Iterate for new ψ values at all points by solving the stream function equation (3.56) using new ω 's at interior points;
6. Find the velocity components from $u = \psi_y$ and $v = -\psi_x$ in discrete form;
7. Determine values of ω on the boundaries using ω and ψ values at interior points defined by equations (3.48) and (3.49);
8. Return to Step 4 if the solution is not converged.

The vorticity transport and the stream function equations are solved by the numerical scheme described with boundary conditions as discussed previously.

3.2 Results

3.2.1 Body Force Results

The aerodynamic plasma actuator's configuration used in experiments [20, 21, 61] consists of two electrodes, one which is exposed to the surrounding air and the other which is completely encapsulated by a dielectric material. The electrodes are placed in an asymmetric arrangement shown in Figure 1.1, that leads to a predominant electric field direction.

To model this particular configuration, the electro-static equation is solved in a square domain with asymmetric electrode configuration separated by a $3 \cdot 10^{-3}$

inch thick Kapton dielectric layer ($\varepsilon = 2.8$) located in the center of the domain. The air has a dielectric coefficient close to the value given for a vacuum, $\varepsilon = 1.0$. The configuration is shown on Figure 3.3. The value of the Debye length λ_D is 0.001 inches, which is characteristic for the plasmas of this type [64].

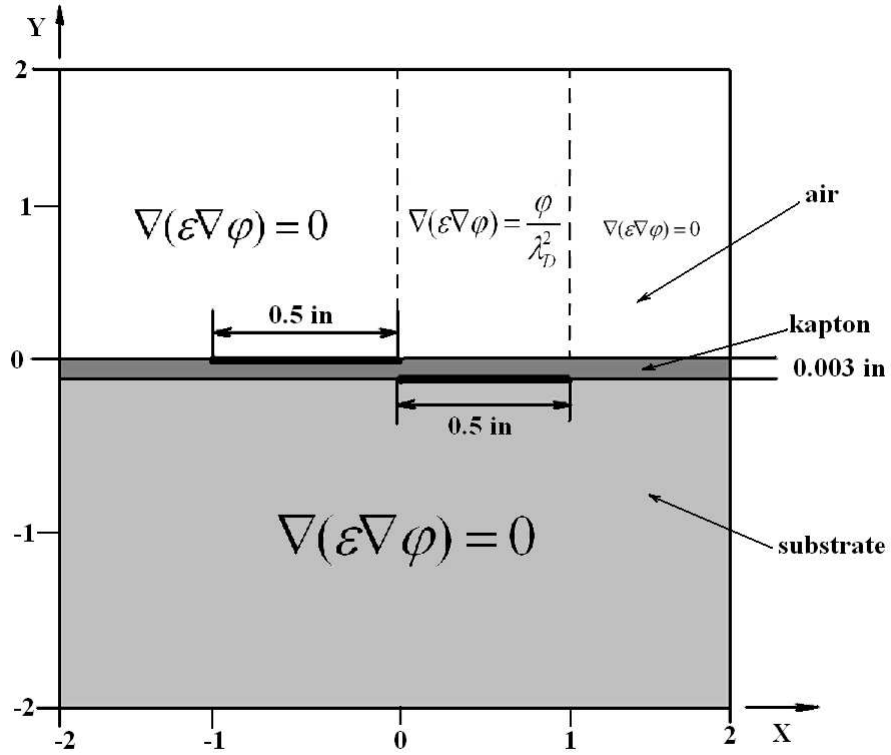


Figure 3.3. Computational domain with two electrodes separated by the dielectric.

The electro-static equation (3.12) was solved inside a 201x201 square domain using the procedure described in Section 3.1.1.2. The boundary conditions that were given by Eq. (3.16 - 3.17) are given as the normalized potential on the exposed (upper) and encapsulated (lower) electrodes, namely

$$\begin{aligned}\varphi|_{\text{upper electrode}} &= 1.0, \\ \varphi|_{\text{lower electrode}} &= -1.0.\end{aligned}\tag{3.57}$$

$$\tag{3.58}$$

On the outer boundaries, which are far from the electrode, the electric potential is zero, namely

$$\varphi|_{\text{outer boundary}} = 0.0.\tag{3.59}$$

The error parameter was defined as the maximum absolute difference in the electric potential variable in two consecutive pseudo-time steps. This is given as

$$ERR = \max(|\varphi_{i,j}^{n+1} - \varphi_{i,j}^n|).\tag{3.60}$$

In the present calculations, it was considered that the convergence was achieved when ERR was less than 10^{-10} . Such a low value was chosen to have sufficient accuracy for body force calculations.

As it had been noticed in the experiments, the plasma exists only above the encapsulated electrode, appearing as the blue glow. That is the region where the Maxwell's equation (3.12) has a non-zero charge term, ρ_c , on the right hand side. In all the other sub-regions of the computational domain, the electro-statics were

modeled by the Maxwell's equation with zero charge density, namely

$$\operatorname{div}\vec{D} = 0. \quad (3.61)$$

In this form, the Maxwell's equation becomes the Laplace equation

$$\nabla(\varepsilon\nabla\varphi) = 0. \quad (3.62)$$

Analyzing the electro-static equation (3.12), it can be noticed that the charges are expected to move to the regions of high electric potential amplitudes. The characteristic length of this region of high charge density is determined by the Debye length coefficient. The smaller the Debye length, the narrower that region located near the electrode and dielectric surface becomes.

To resolve the electric field in this narrow surface region, the Robert's stretching [6] was used in the vertical direction, clustering the grid lines near the surface. The equation for the location of the wall-normal grid points is

$$y = \frac{h_y (\beta_y + 1) - (\beta_y - 1) \{[(\beta_y + 1)/(\beta_y - 1)]^{1-\bar{y}}\}}{2 [(\beta_y + 1)/(\beta_y - 1)]^{1-\bar{y}} + 1}, \quad (3.63)$$

where h_y is the size of the domain in the y direction, β_y is the stretching parameter in the y direction, taken to be 1.001, and \bar{y} is the coordinate of the nonclustered uniform grid points.

The same Robert's stretch was needed to be performed in the horizontal direction, x , in order to cluster grid lines near the inner edge of the electrodes to resolve the electric field in the region where the plasma existed, and where the body force coupled with surrounding neutral air. The stretching formulation is

given as

$$x = \frac{h_x (\beta_x + 1) - (\beta_x - 1) \{[(\beta_x + 1)/(\beta_x - 1)]^{1-\bar{x}}\}}{2 [(\beta_x + 1)/(\beta_x - 1)]^{1-\bar{x}} + 1}, \quad (3.64)$$

where h_x is the size of the domain in the x direction, and β_x is the stretching parameter in the x direction, this was again taken to be 1.001, and \bar{x} is the coordinate of the nonclustered uniform grid points. The resulting non-uniform solution grid is shown on Figure 3.4. A zoomed-in view of the grid near the electrodes is shown in Figure 3.5.

In its mathematical formulation, this problem is very similar to the heat transfer problem, in which the temperature variable plays the same role as the electric potential in electro-statics. The dielectric coefficient ε is similar to the heat transfer coefficient k .

The result of the electric potential computations is presented on Figure 3.6 showing the magnitude of the electric potential in the computational domain as a function of the space coordinates. Referring back to Figures 3.4 and 3.5, Y is the direction above and below the electrodes, X is the direction parallel to the electrodes. The constant potential is seen to exist on the electrodes as specified by the boundary conditions. The potential decays rapidly in space off the electrodes.

A zoomed-in view of lines of constant electric potential near the inner edges of the electrodes is shown in Figure 3.7. Mathematically, these lines of constant potential are similar to the iso-thermal lines in the heat transfer problem. The lines circle around the electrodes, and the isolines of a higher electric potential are closer to the upper electrode, while the low electric potential isolines are clustered near the lower electrode. The electric potential lines are not symmetric about the line running through the aligned edge of the electrodes because of the ionization

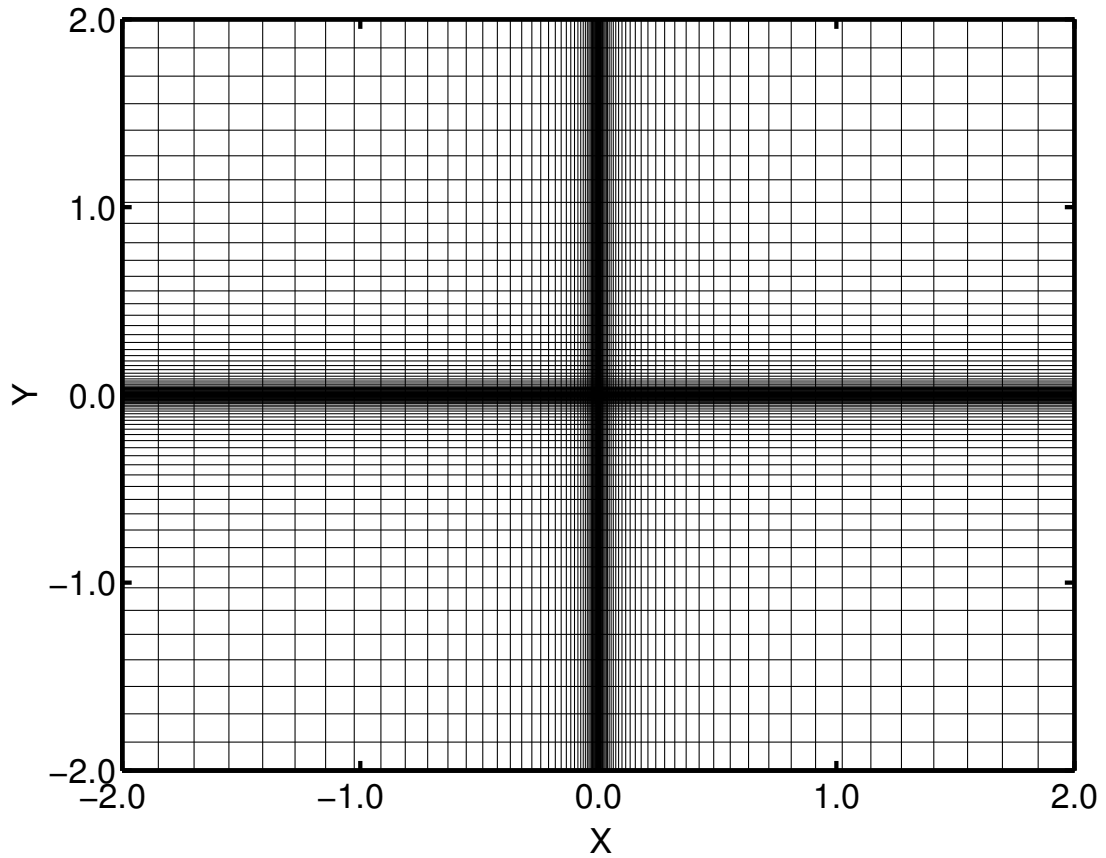


Figure 3.4. Numerical grid for the electro-static problem with Robert's stretching applied to resolve electric field and body force near the electrodes.

in the air over the covered electrode, which distorts the electric field lines in that region.

The enlarged view of the region close to the inner electrode edges indicates that there are large gradients in the electric potential that are produced by the electrode geometry that produce a large electric field strength E . The electric field corresponding to the potential field lines shown in Figure 3.7 is shown in Figure

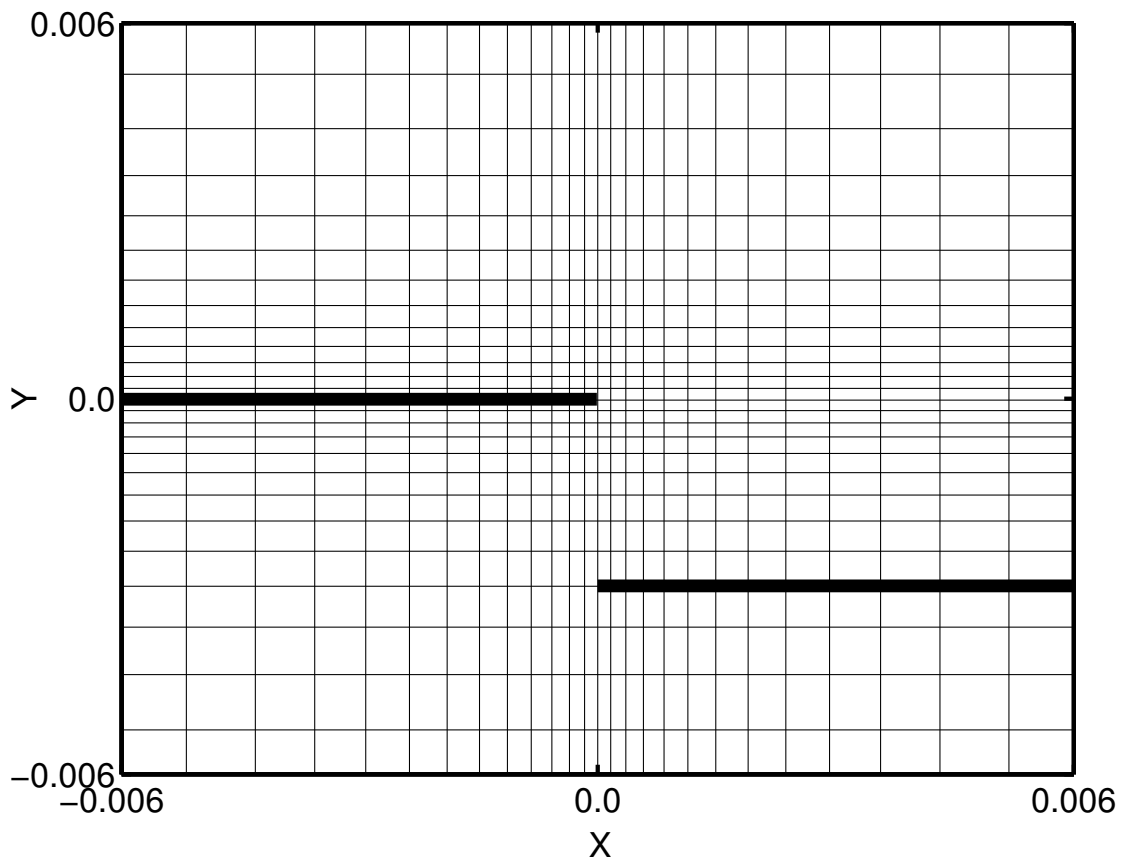


Figure 3.5. Zoomed-in view of the numerical grid for the electro-static problem with Robert's stretching applied to resolve electric field and body force near the electrodes.

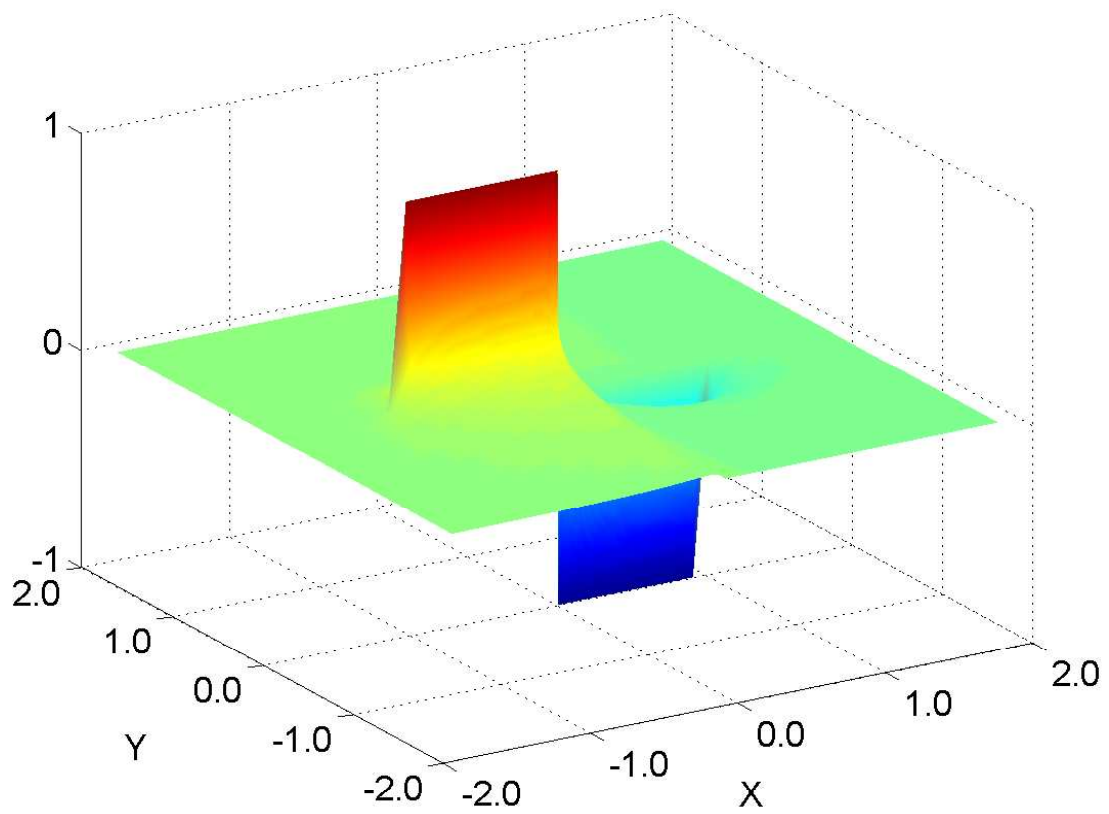


Figure 3.6. Electric potential φ as a function of space coordinates.

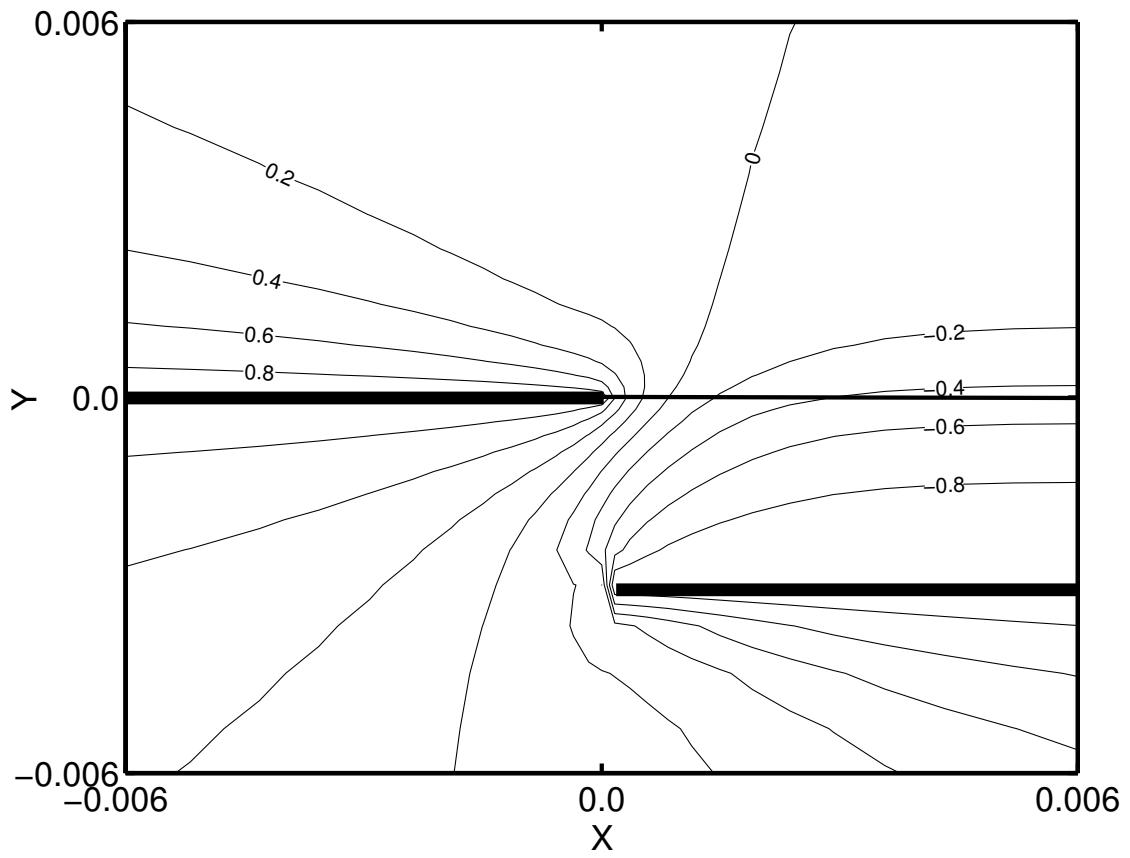


Figure 3.7. Lines of constant electric potential near inner edge of electrodes.

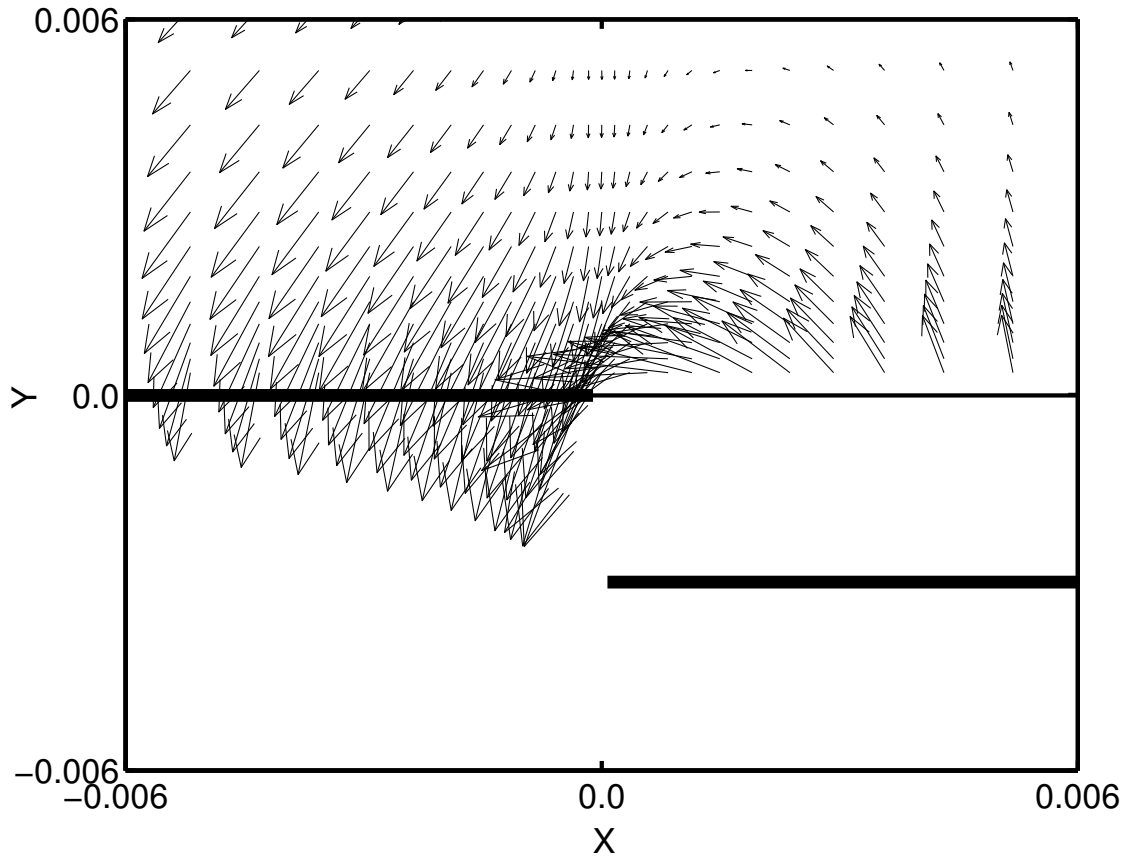


Figure 3.8. Electric field \vec{E} in the upper part of the domain (air), near inner electrodes' edges.

3.8. The arrows indicate the vector direction which is generally towards the upper electrode.

The body force calculated as given by equation (3.20) is presented on Figure 3.9. Note that the body force only exists where the free charges are present in the air. This is only over the covered electrode. Everywhere else, the body force is zero by definition.

The enlarged view of the body force vectors in Figure 3.9 gives a somewhat distorted view of the extent of the body force produced by the asymmetric elec-

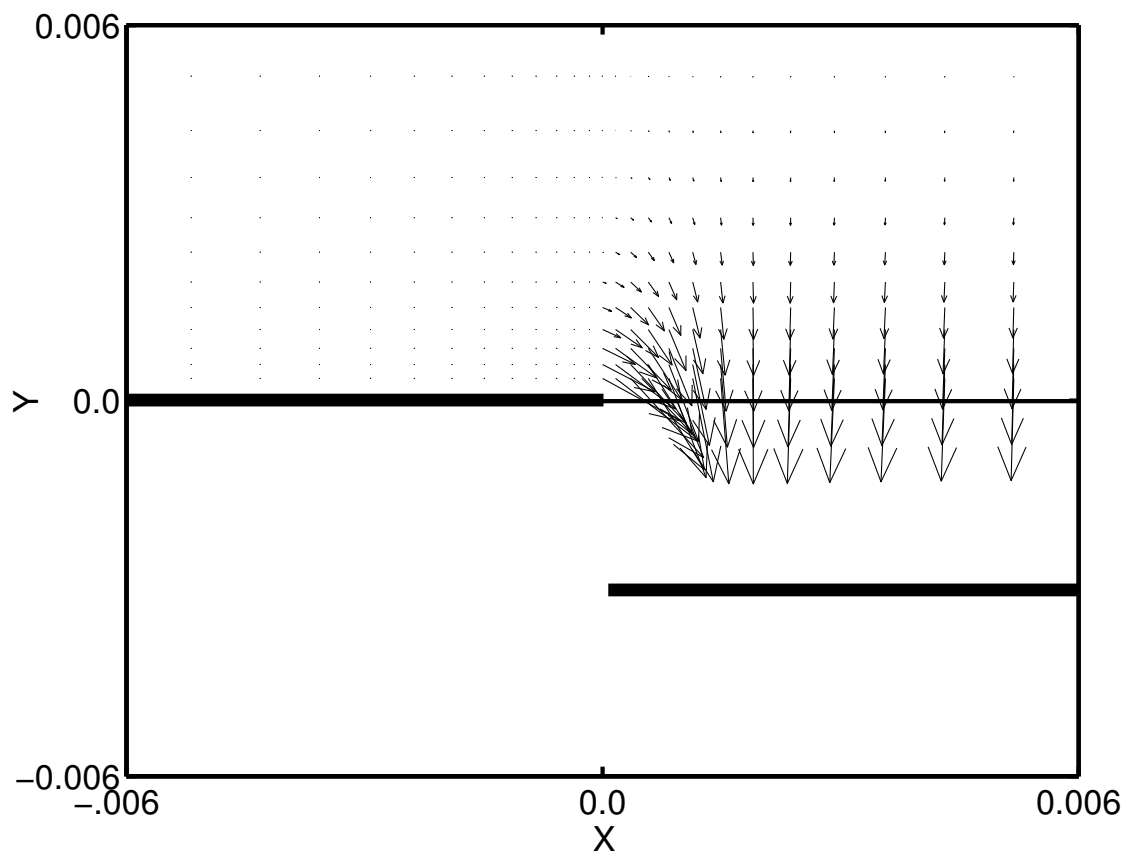


Figure 3.9. Body force as result of electro-static equation solution.

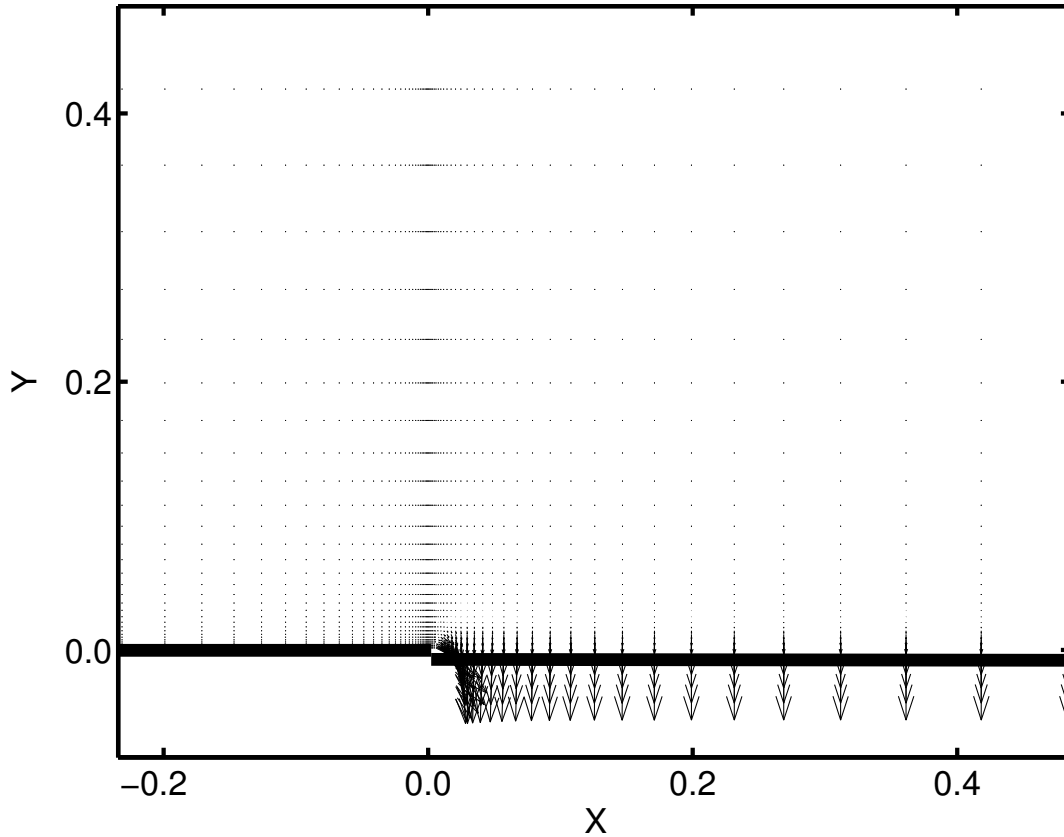


Figure 3.10. Body force on the fluid flow scale.

trode arrangement. In actuality it is localized to being very close to the dielectric surface, in the Debye region. This is shown in Figure 3.10.

Figure 3.10 would indicate that the body force vectors have significant magnitude everywhere above the insulated electrode, and that they are primarily directed downward.

The body force vectors were used in the Navier-Stokes flow simulation for the conditions of the actuator placed on the lower wall of an enclosed box with zero mean flow. This configuration simulates an experiment by Post [61]. In the simulation, the body force was impulsively started, similar to the Post experiment

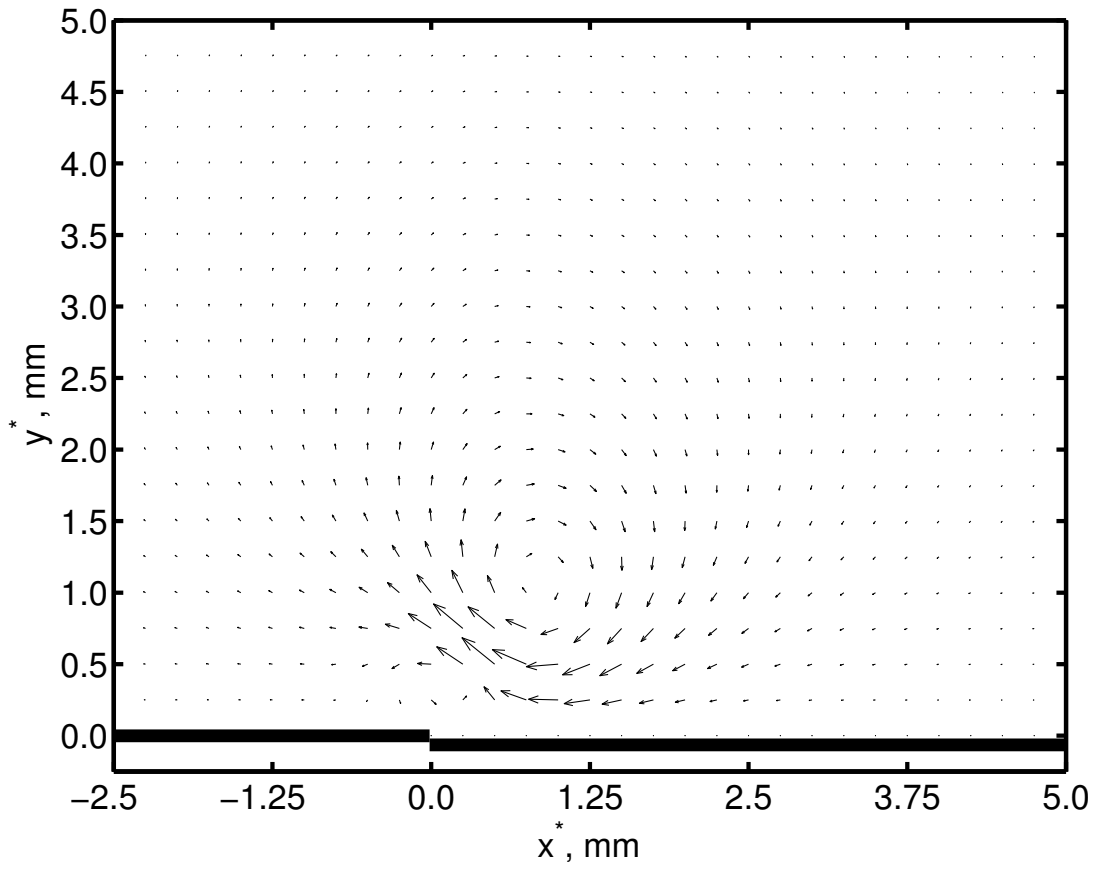


Figure 3.11. Incorrect flow resulting from non-weighted body force. The largest velocity vector corresponds to $|V| = 2$ m/s.

where the actuator was impulsively turned on. The result of the simulation is shown in Figure 3.11. The simulation with the body force vectors shown in Figure 3.10 indicates that the impulsive start results in a starting vortex with a circulation in a clockwise direction. In fact, the Post [61] experiment indicated that a starting vortex occurred in the counter-clockwise direction, opposite of the simulation.

The answer to the discrepancy comes by noting that the body force is per volume of plasma. Figure 2.4 showed that the light intensity from the plasma actuator was not uniform over the covered electrode but was a function of the distance from the edge of the exposed electrode. In addition, it was time dependent sweeping out over the covered electrode during the a.c. cycle. This was illustrated in the space-time maps of the light emission that were presented in Figures 2.8 to 2.14.

As a result, the time-averaged volume of plasma decreases with distance from the edge of the exposed electrode. The static analysis used in obtaining the body force in Figure 3.10 did not account for the decrease in plasma volume. In order to compensate for this, the body force magnitude was weighted spatially using a weighting function that was based on the spatial variation of the time-averaged plasma illumination. Figure 3.12 shows a fit to the spatial illumination that was used as a spatial weighting function, $w(x)$, where

$$w(x) = e^{-x/0.0127}. \quad (3.65)$$

This was then used to correct the spatial variation in the body force as

$$\vec{f}_b^*(x, y) = \vec{f}_b(x, y) * w(x). \quad (3.66)$$

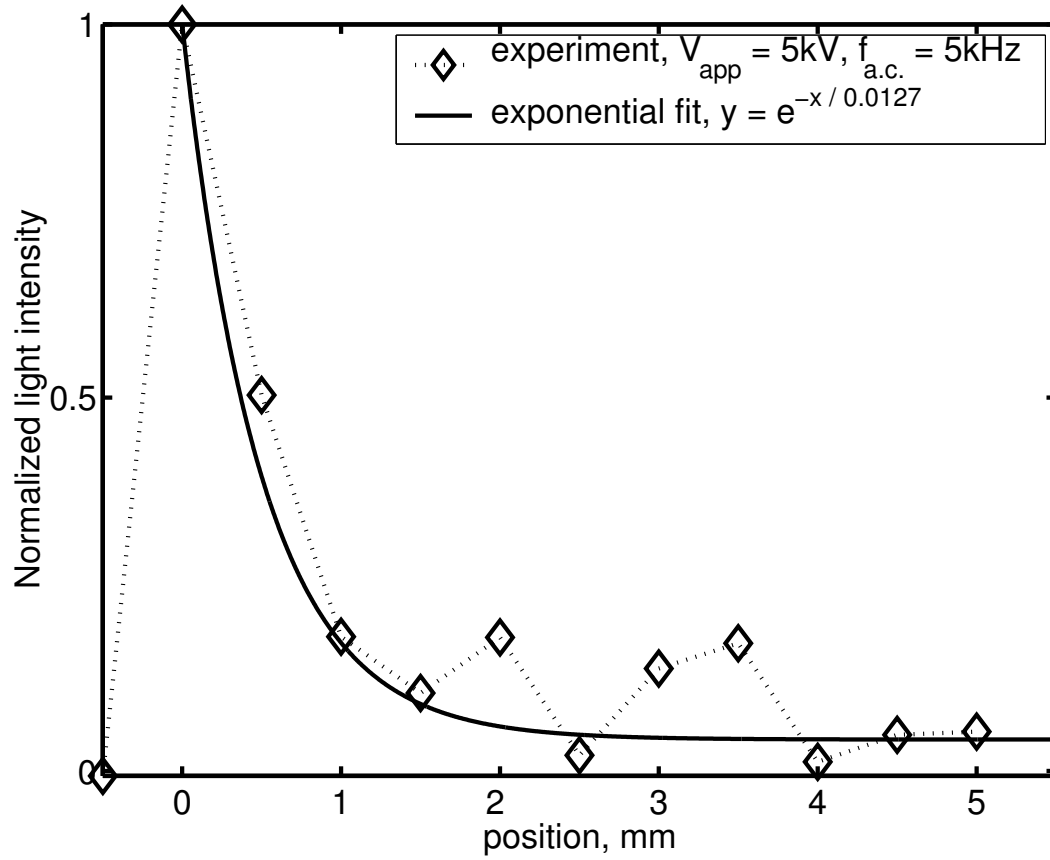


Figure 3.12. Spatial variation of light intensity from the plasma actuator.

The result of applying the spatial weighting to the electro-static body force that was shown in Figure 3.9 is shown in Figure 3.13. The weighting, which is the strongly decaying exponential function, quickly suppresses the body force vectors at distances away from the edge of the exposed electrode. The result is that only the body force vectors near the edge of the exposed electrode are significant. These vectors have a component that is directed along and away from the upper electrode. Simulations to follow will show that impulsively starting this weighted body force will result in a starting vortex that will produce counter-clockwise circulation that agrees with the experimental observations.

After a weighting function has been applied to the body force as

$$\vec{f}_b^*(x, y) = \vec{f}_b(x, y) * w(x), \quad (3.67)$$

where $w(x)$ is the weighting function, the resulting body force is shown in Figure (3.13). This body force is the force that comes into the Navier-Stokes equations.

3.2.2 Flow Problem Results with Spatially Weighted Body Force

The equations for the flow in stream function and vorticity form (3.39 - 3.40) were solved on the identical grid to the upper half domain used in the electro-static body force computations. This allows the body force values from the electro-static problem to be transported to the flow solution grid point-by-point, without any interpolation. The solution grid is shown in Figure 3.14.

The stream function and vorticity equations were solved numerically using the procedure that was described previously. The actuator is located at $X=0$ and the domain of the body force is 0 to 1 in X and 0 to 2 in Y . The Reynolds number based on the length of the actuator (0.5 in.), a characteristic velocity of 1 m/s,

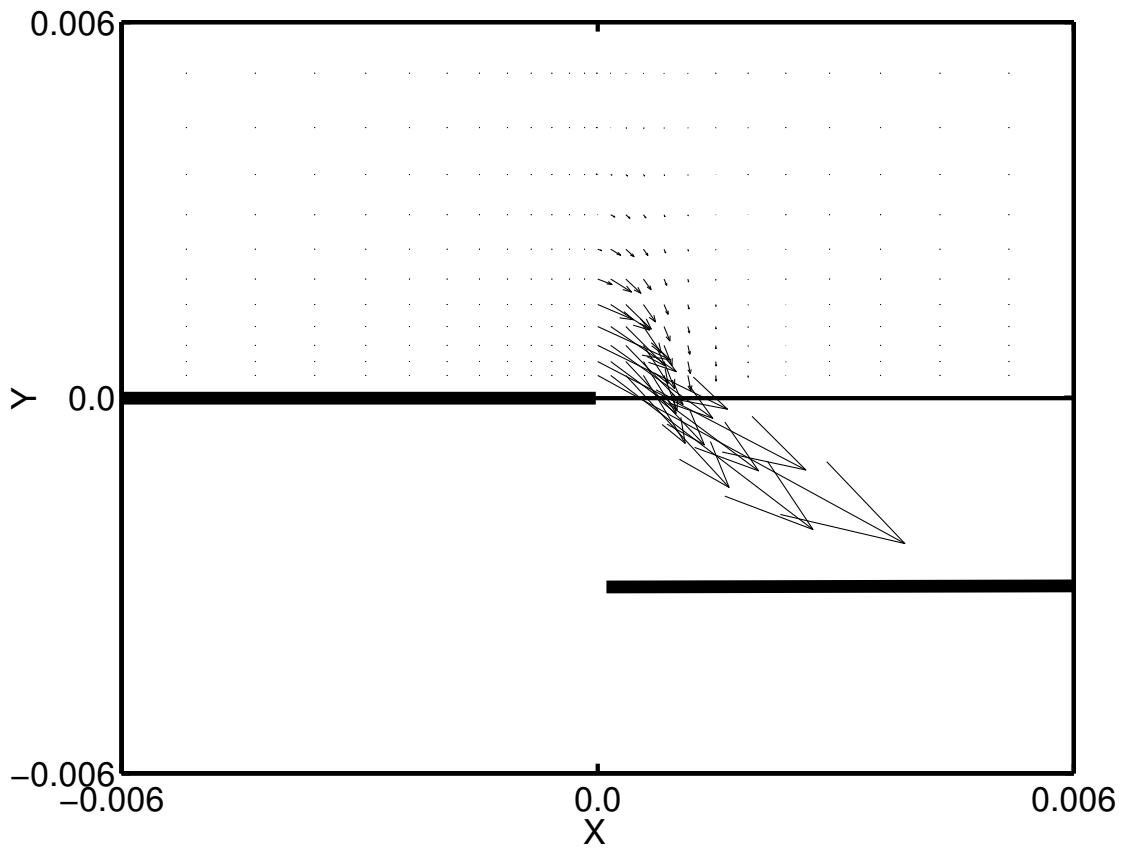


Figure 3.13. Spatially-weighted body force.

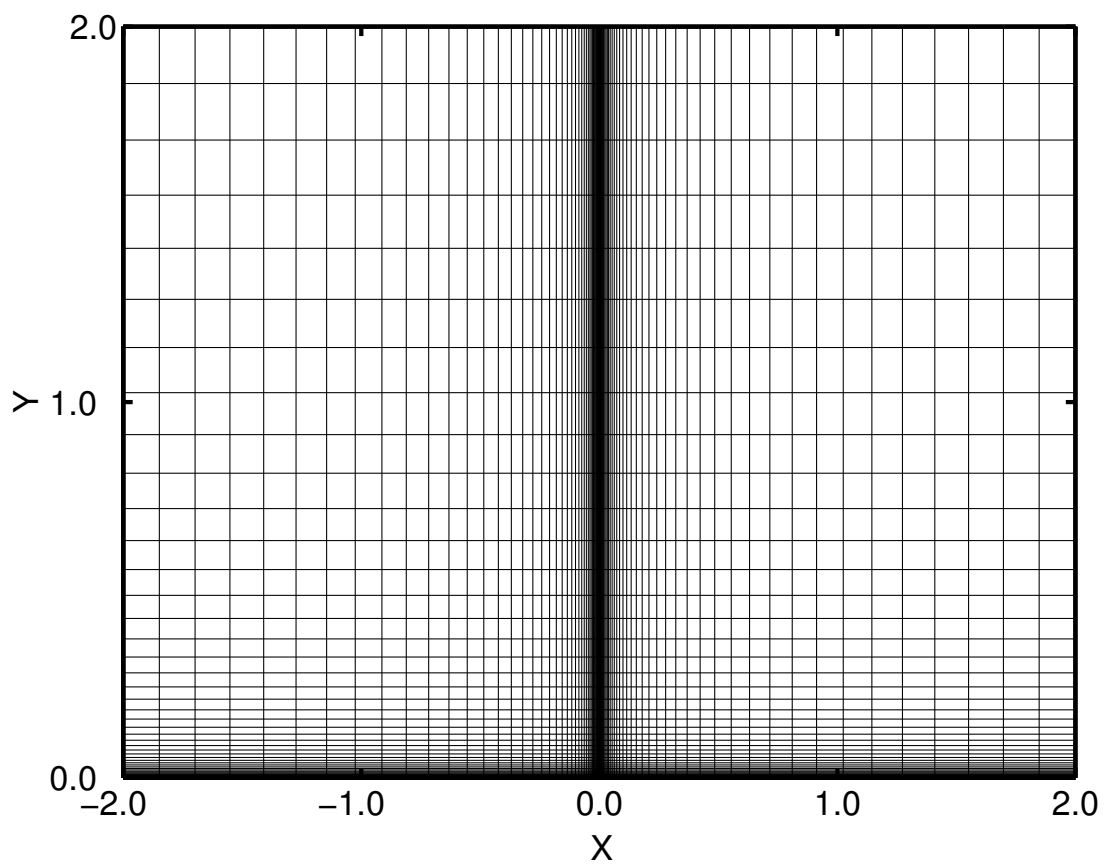


Figure 3.14. Computational domain, normalized by X_{max} and Y_{max} , actuator located on the bottom surface at $X = 0.5$.

and the kinematic viscosity of air at standard temperature and pressure used in the simulation, was 10^5 .

In the solution of equation (3.39) the error parameter was defined as the maximum absolute difference in the stream function variable in two consecutive pseudo-time steps, namely

$$ERR = \max(|\psi_{i,j}^{n+1} - \psi_{i,j}^n|) \quad (3.68)$$

Convergence was considered to be achieved when ERR was less than 10^{-16} . At this level of convergence, the convergence on vorticity given as the maximum difference between two consecutive pseudo-time steps

$$ERR = \max(|\omega_{i,j}^{n+1} - \omega_{i,j}^n|) \quad (3.69)$$

was on the order of 10^{-10} .

The boundary conditions were chosen as stated previously as no slip, no penetration on all the walls of the box. Still air conditions were taken for initial conditions:

$$u|_{t=0} = 0 \quad (3.70)$$

$$v|_{t=0} = 0$$

In order to simulate the impulsively started plasma actuator in the experiments by Post [61], the spatially-weighted body force was introduced into the stream function and vorticity equations as a step function. This is illustrated in Figure 3.15.

Having no external flow in the simulation, the actuator body force is the only source of fluid motion. The flow simulation a short time (0.25 ms) after the

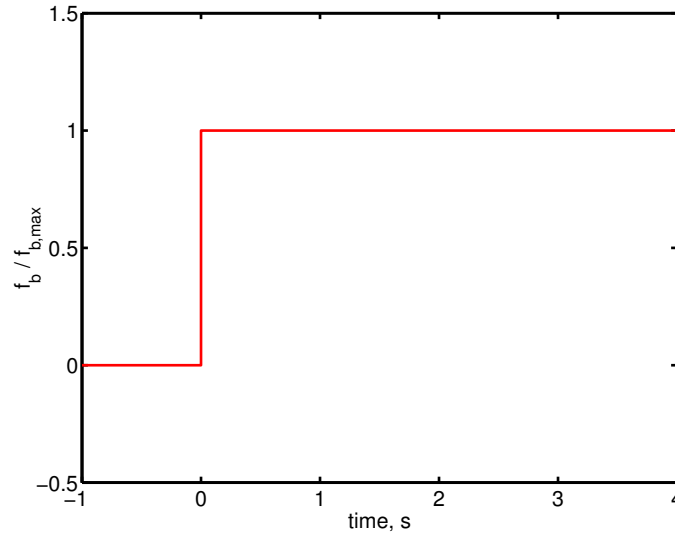


Figure 3.15. Body force is introduced into the Navier-Stokes equations at time $t = 0$.

body force has been switched on is shown in Figure 3.16. This shows a starting vortex that has a circulation in the counterclockwise direction. The simulation at a slightly later time of 1.25 ms is shown in Figure 3.17. This shows that the starting vortex has strengthened and expanded with the center further away from the wall.

As mentioned, the simulation was intended to compare to the experiments of Post [61]. Her experiment involved placing a plasma actuator, with an asymmetric electrode arrangement that was identical in size and configuration to the simulated actuator, on the floor in a sealed box. The actuator was impulsively started and left on over a long period that was much longer than the response time of the flow. Velocity measurements were made by her using PIV system. A photograph and a schematic of her experiment is shown in Figure 3.18.

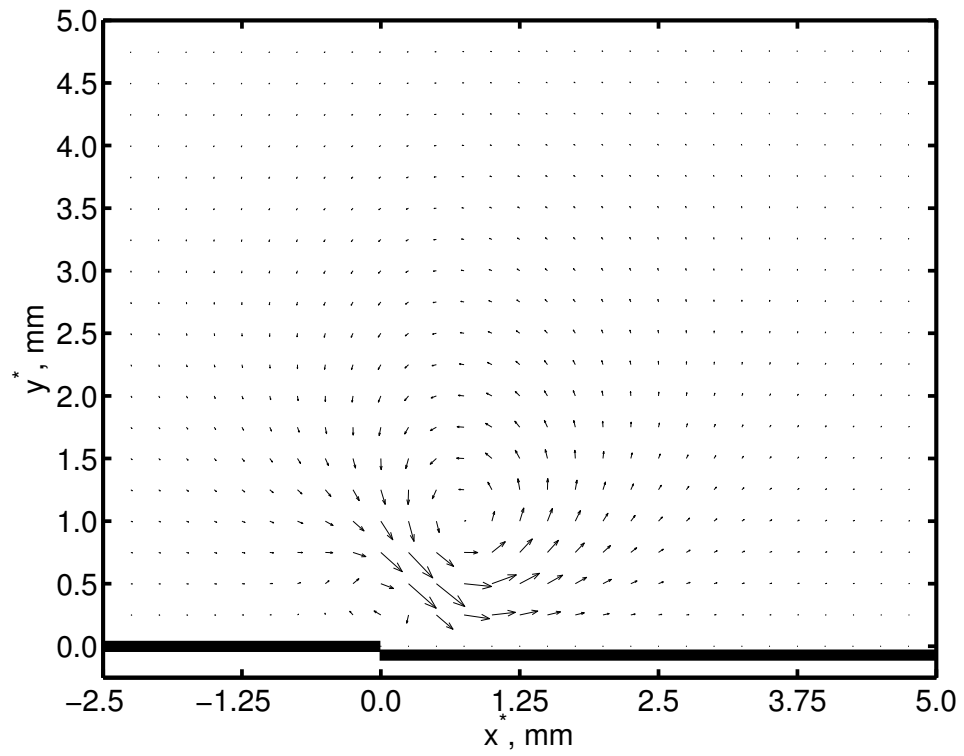


Figure 3.16. “Starting” vortex near actuators at $t = 0.25\text{ms}$. The largest velocity vector corresponds to $|V| = 1.5 \text{ m/s}$.

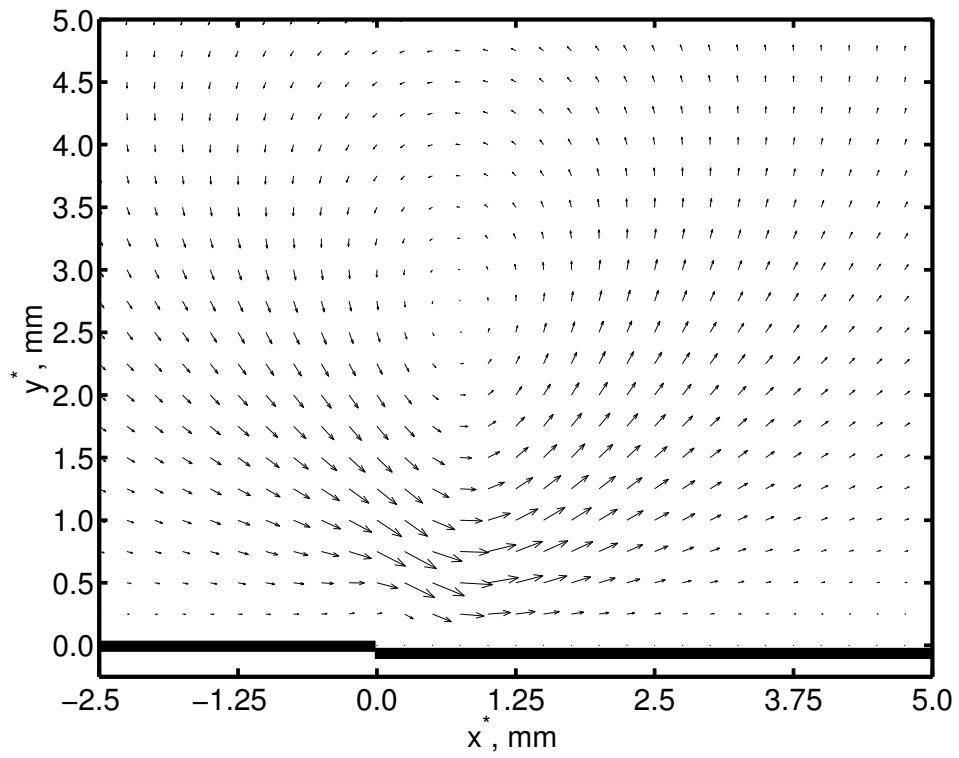


Figure 3.17. “Starting” vortex near actuators at $t = 1.25ms$. The largest velocity vector corresponds to $|V| = 3 \text{ m/s}$.

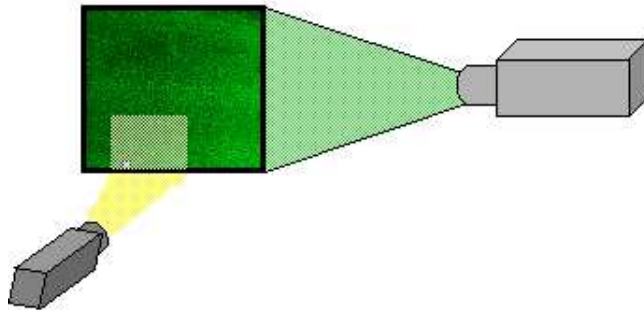


Figure 3.18. PIV setup by Post [61].

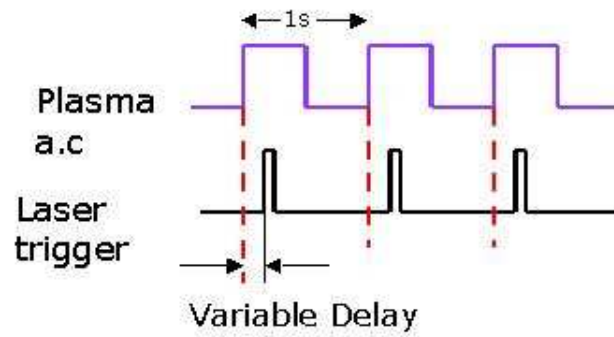


Figure 3.19. PIV laser trigger setup by Post [61].

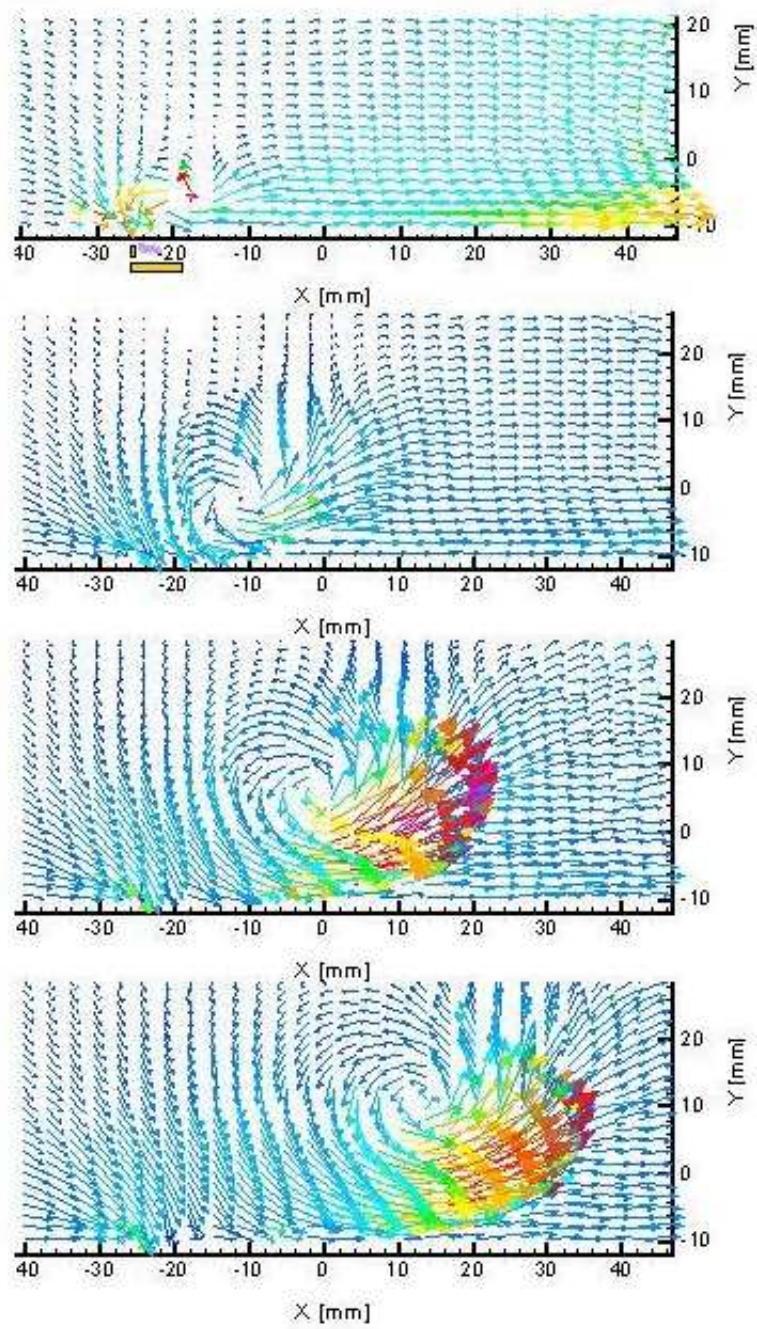


Figure 3.20. “Starting” vortex at $t = 2, 12, 35, 60$ ms, PIV results by Post [61].

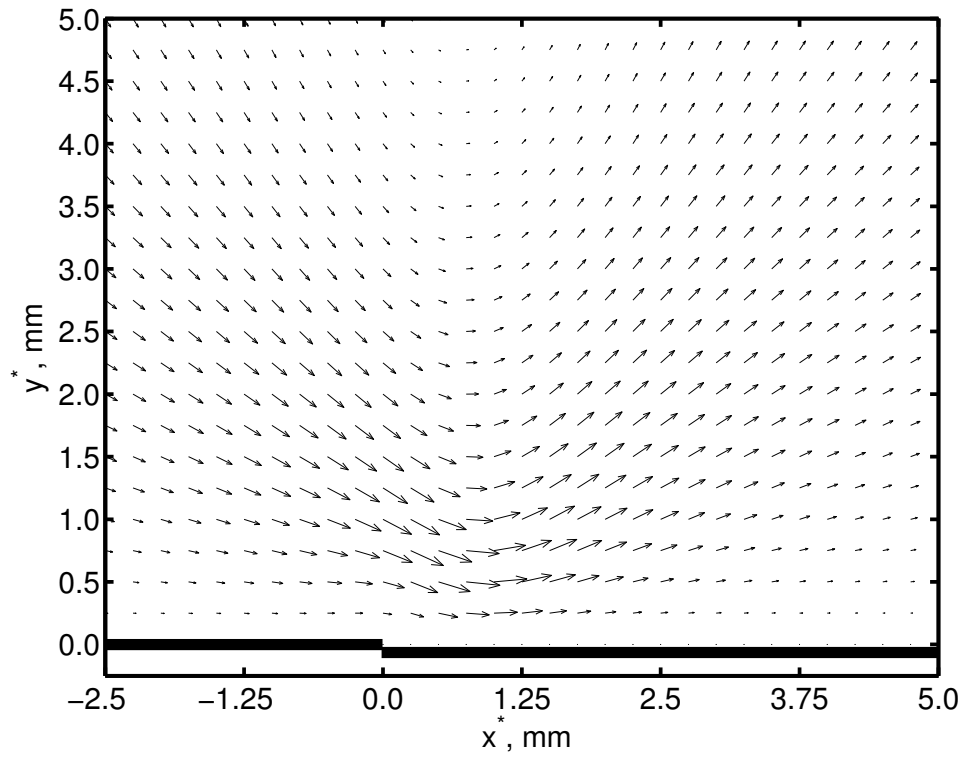


Figure 3.21. Velocity field of the developed jet flow at $T \rightarrow \infty$. The largest velocity vector corresponds to $|V| = 4.7$ m/s.

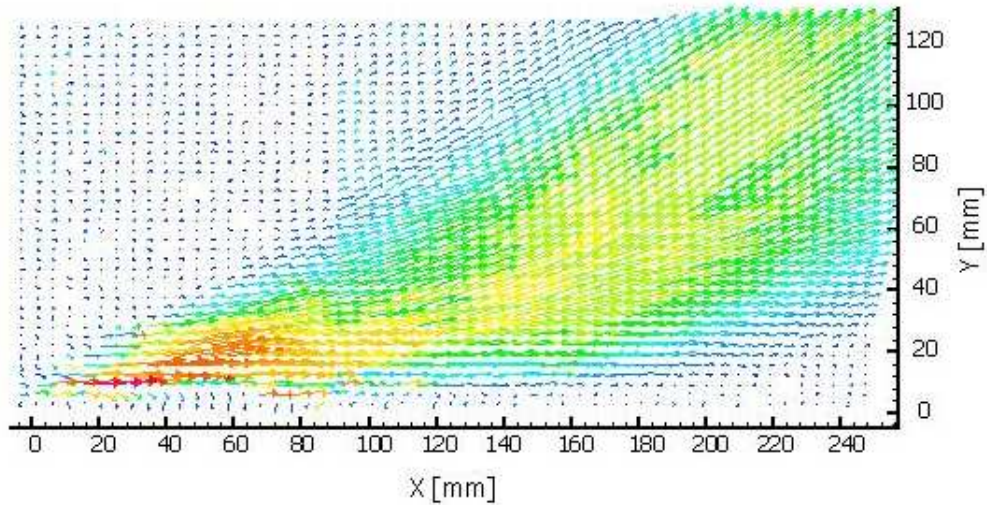


Figure 3.22. Developed jet flow at $T \rightarrow \infty$, PIV results by Post [61].

Post used a trigger signal on the PIV laser to capture the velocity field at certain time delays following the impulsive starting of the actuator. A schematic of the laser trigger timing is shown in Figure 3.19. She then obtained ensemble averages of the velocity field generated by the impulsively started actuator. Examples of those are shown in Figure 3.20. The actuator is located at $x = -26$ mm.

The experimental results correspond to time delays of 2, 12, 35 and 60 milliseconds. These show the initial development of a starting vortex with counter-clockwise circulation. As time progresses in the experiment, the starting vortex grows in size and convects to the right in the positive x -direction.

Qualitatively the velocity field obtained in the simulation, shown in Figures 3.16 and 3.17, looks similar. The size of the spatial domain of the simulations is approximately 6 by 6 mm. Therefore they are showing the starting vortex at a very initial stage which is closest to the smallest experimental time delay shown on the top plot in Figure 3.20.

The solution for the flow field a long time after the actuator was impulsively started is shown in Figure 3.21. The result from the experiment of Post [61] is shown in Figure 3.22. Both show that the flow is drawn down towards the actuator and then accelerated away from the actuator in the direction from the upper to the lower electrode. The size of the spatial domain of the simulation is only about one-tenth of the experimental domain in order to focus on the region closest to the actuator. However qualitatively at least, the vector field is very similar, indicating that the electro-static model for the actuator body force vector is reasonably good.

3.2.3 Flow Problem Results with Temporally-spatially weighted body force.

Looking more closely at the light intensity results from photomultiplier experiments, it can be noticed that the volume of plasma at any spatial location was very dependent on time within the a.c. cycle. For example, close to the edge of the upper (exposed) electrode, plasma light illumination intensity increased linearly with time in each half of the a.c. period. This is evident in the light intensity contours that were shown in Figure 2.5. This indicates that an improved body force model from the electro-static calculations would add a second body force weighting that would account for the time dependence of the ionization.

The temporally-spatially weighted electro-static body force was represented by the form

$$\vec{f}_b^*(x, y) = \vec{f}_b^*(x, y) \cdot w(x) \cdot a(t) \quad (3.71)$$

where $w(x)$ is the previously defined spatial weighting function, and $a(t)$ represents the linear temporal growth observed in the experiments. The total space-time

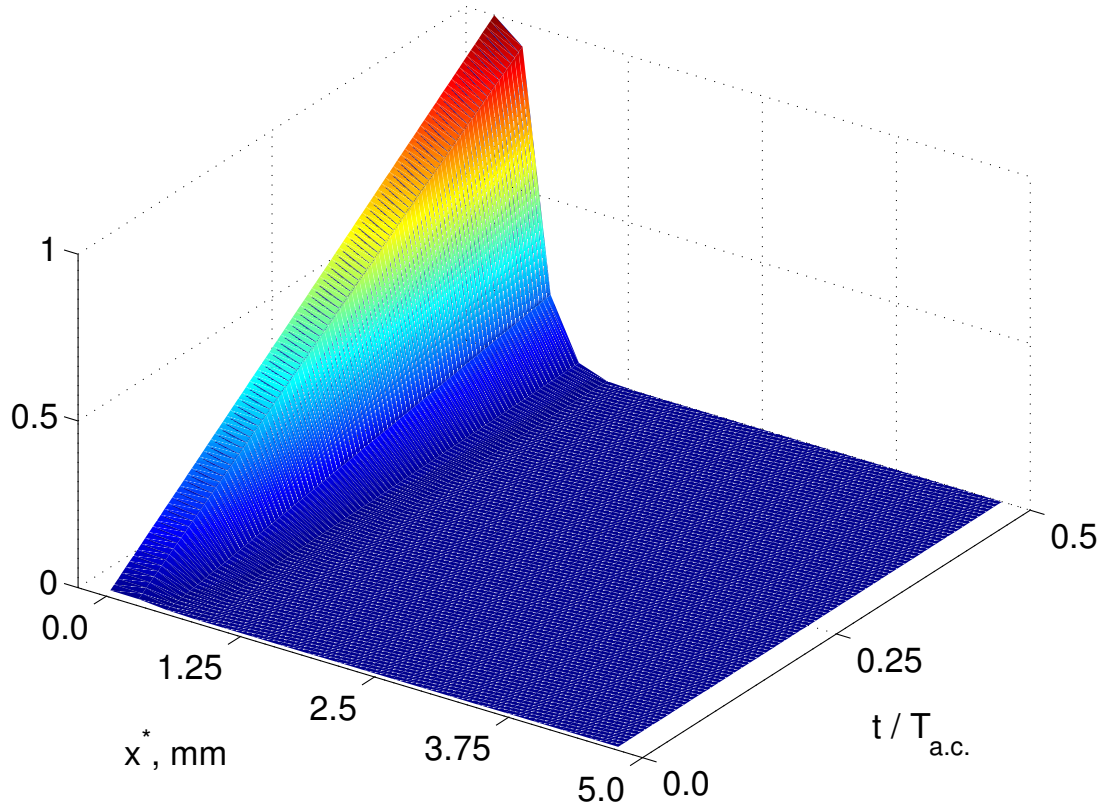


Figure 3.23. Magnitude of the space-time weighting function used on the electro-static body force for one half of the a.c. cycle.

weighting function , $w(x) \cdot a(t)$, is presented in Figure 3.23 for one half period of the a.c. cycle.

The results of the numerical simulation for the flow generated by the actuator on the bottom wall in a rectangular enclosure with the added temporal weighting on the body force is qualitatively similar to previous case with only the spatial weighting. When the actuator was impulsively started it produced a similar starting vortex with counterclockwise circulation that grows in size and convects away as before. At large solution times, the flow near the actuator again becomes a

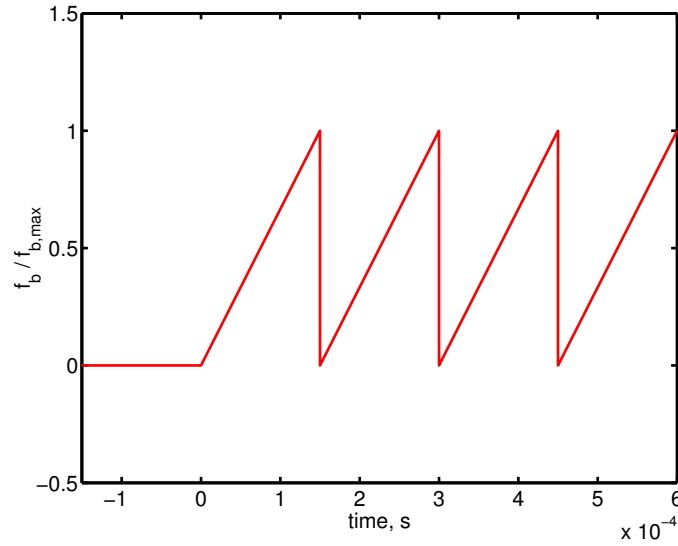


Figure 3.24. Method for introducing space-time weighting of electro-static body force during time-steps of the Navier-Stokes solver.

steady tangential wall jet in the direction towards and away from the covered electrode.

To compare the two cases of the two types of weighting on the body force, the long time steady solution was considered. In particular, wall-normal profiles of the x -component of velocity were compared. As a first step in comparing the profiles, the distance from the actuator where the flow was self-similar was determined. An example of this for the case with only spatial weighting for the steady (long-time) solution is shown in Figure 3.25. Here the profiles were taken at different x locations in the induced flow direction away from the actuator. The velocities in the profiles were normalized by the maximum at that x -location. The wall normal coordinate was normalized by the y -value of the velocity maximum. These are

defined in the following.

$$\begin{aligned}
 U_{norm} &= \frac{U}{U_{max}} \\
 y_{norm} &= \frac{y}{y(U_{max})}
 \end{aligned}
 \tag{3.72}$$

Focusing on the normalized profiles in Figure 3.25, we observe that by the fourth location away from the actuators, the profiles begin to fall onto a single curve. This is particularly evident in the lower part of the profiles up to the height corresponding to U_{max} . Based on this result, velocity profiles for the two body force weighting cases were compared at $X = 0.5938$. These are compared at different times after the impulsive start of the actuator body force in Figures 3.26 and 3.27.

Figure 3.26 shows the velocity profiles for the case with only spatial weighting of the body force. The profiles for the case with space-time weighting are shown in Figure 3.27. Both of these show the character of an accelerating wall jet. The outer part of the profile, above $y^* = 1$ cm, has negative velocities due to reverse flow produced by a flow recirculation in the box that was induced by the actuator.

One of the things that can be easily noticed on the comparison of the two cases is that the space-time weighted body force resulted in a maximum velocity that was approximately one-third that of the other weighting. This indicates that the time response of the ionization is significant to the performance of the actuator. It suggests that the performance would increase if the a.c. frequency is increased. This is an aspect that will be examined with the lumped-element circuit model in a section to follow.

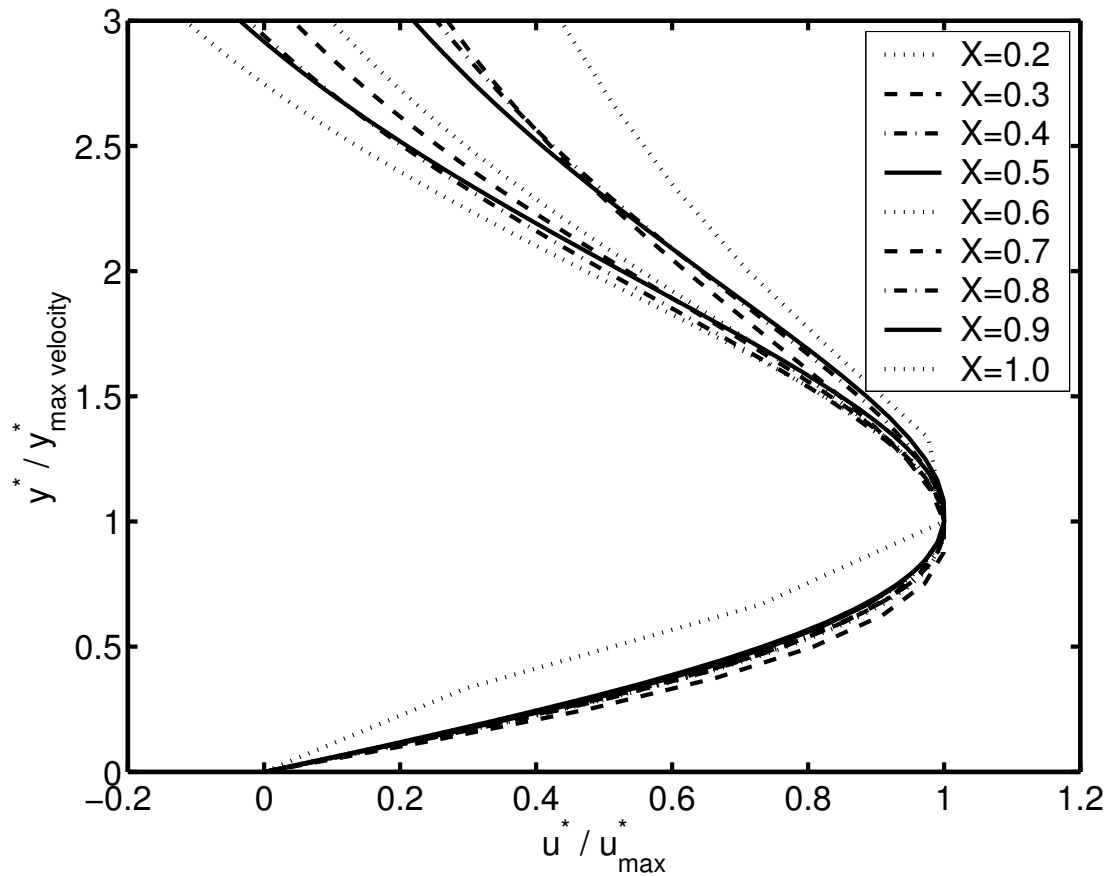


Figure 3.25. x -component velocity profiles normalized by maximum velocities and the locations of maximum velocities at different locations downstream of the simulated actuator with spatial weighting of the body force and the steady (long-time) solution.

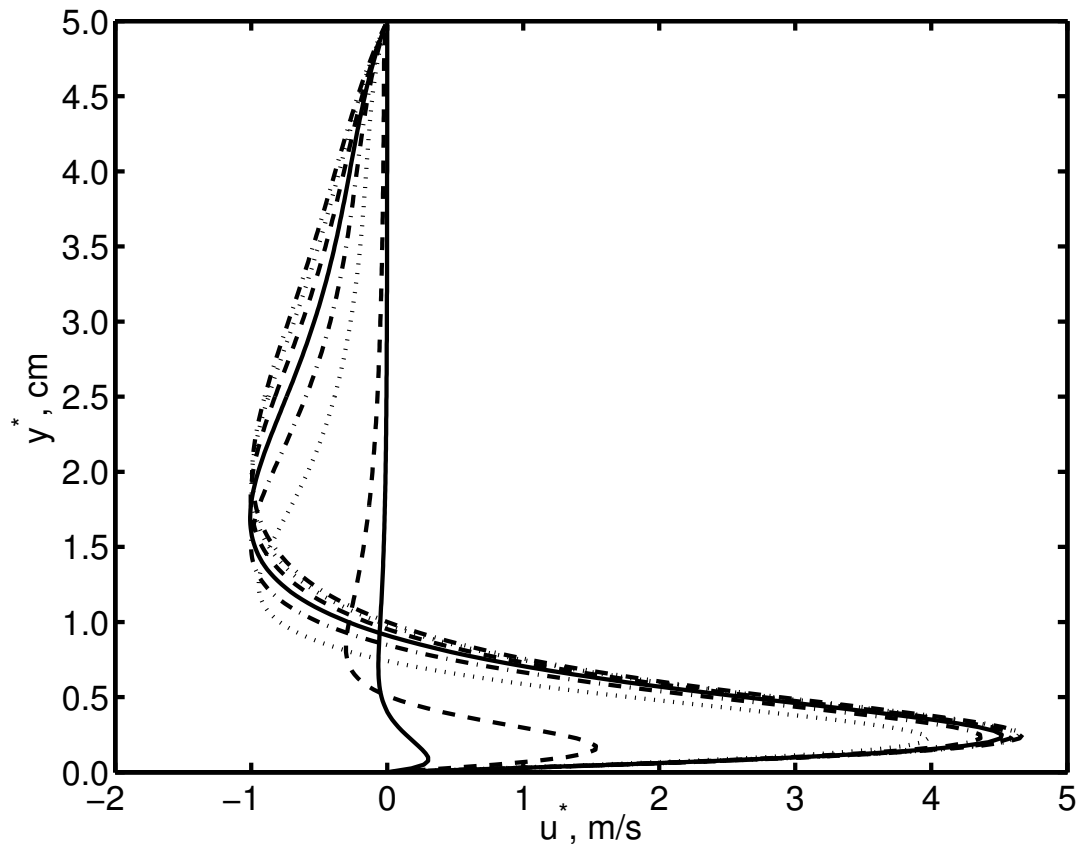


Figure 3.26. x -component velocity profiles taken at $X = 0.5938$ for different times following the impulsive start of the actuator body force. Body force is spatially weighted only.

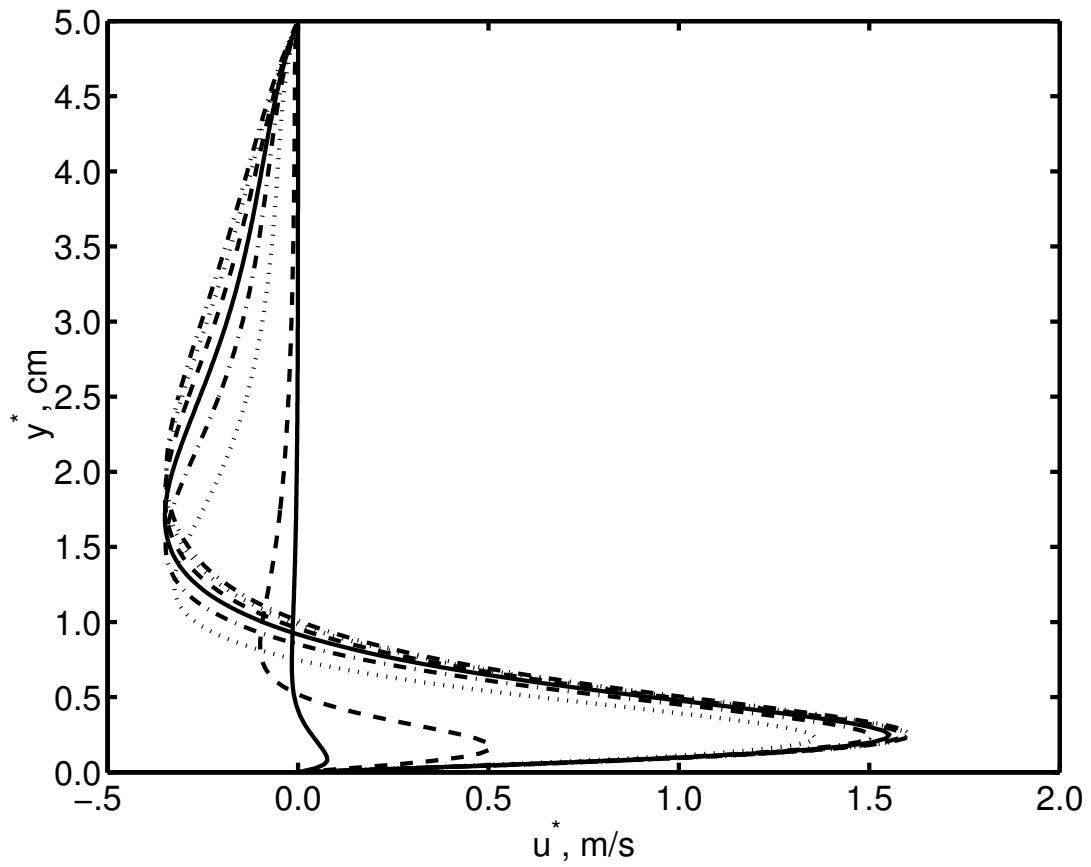


Figure 3.27. x -component velocity profiles taken at $X = 0.5938$ for different times following the impulsive start of the actuator body force. Body force is spatially-temporally weighted.

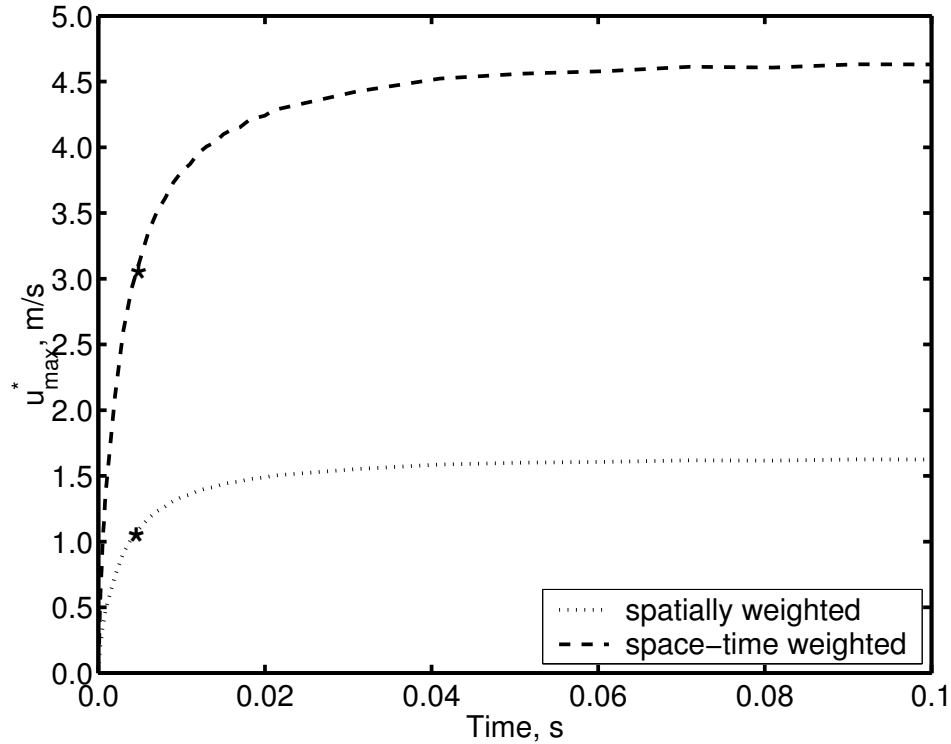


Figure 3.28. Maximum x -component velocity as a function of time for impulsively started actuator body force. Star indicates first-order time constant corresponding to where $\frac{U}{U_{t \rightarrow \infty}} = \frac{1}{e}$.

The temporal response of the flow can be characterized by its response to the impulsive (step) start of the actuator body force. To illustrate this, the maximum velocities from Figures 3.26 and 3.27 as a function of time were plotted in Figure 3.28. This indicates that the maximum velocity of the flow induced by the actuator reaches an asymptote after long time. If we consider this to be a first-order response to a step input, the time constant corresponds to the time when the velocity is 66.3 ($1/e$) of the values at large time. This point has been noted by the star symbol in the figure.

We observe that the time constant for the flow response is the same value for the two initial conditions. Although these initial conditions were obtained by using different weighting on the body force, they are essentially only different by the amplitude of the step input. Therefore we expect the time constant to be the same for the two trials with different initial amplitudes. The value of $\tau = 0.01$ s suggests a frequency response of 100 Hz. This result for the time constant value corresponds well to the result from the experiment by Post [61].

Although the electro-static model for the plasma actuator could correctly describe its effect on a neutral ambient fluid, it cannot model the effects of the input voltage amplitude or a.c. frequency. The success of the simulations in this section were due to experimentally determined ionization in space and time that corresponds to a particular a.c. frequency and amplitude.

To illustrate the problem, if one would use the electro-static model with different input voltage amplitudes, the dimensionless plasma body force would be [76]

$$f_b = \alpha \cdot \bar{\varphi} \cdot \nabla \bar{\varphi}, \quad (3.73)$$

where α is the dimensionless scaling parameter given as

$$\alpha = \frac{\varepsilon_0 \varphi_0^2}{\rho_\infty U_\infty^2 \lambda_D^2}. \quad (3.74)$$

As before φ_0 is the amplitude of the electrode potential, U_∞ is a characteristic fluid velocity, and ρ_∞ is a characteristic fluid density. Equations (3.73) and (3.74) suggest that the plasma body force will increase quadratically with the input voltage amplitude, namely

$$f_b \sim V_{app}^2. \quad (3.75)$$

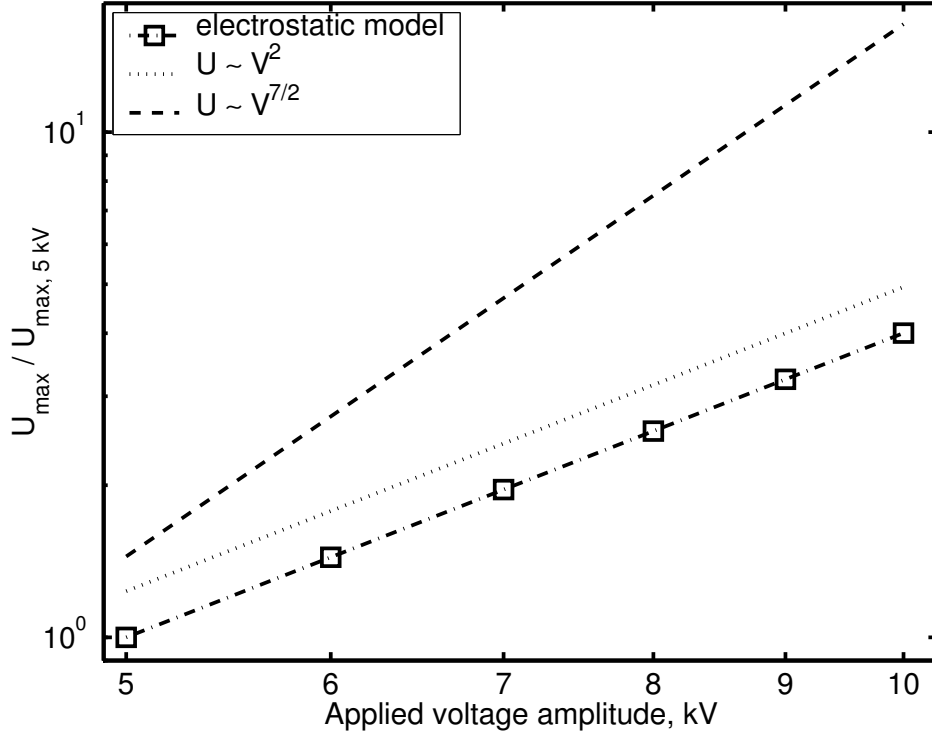


Figure 3.29. Maximum induced velocity in electro-static actuator model as a function of voltage.

If this form of the body force is used with the flow solver, the maximum induced velocity is found to increase in proportion to the square of the applied voltage. This is shown in Figure 3.29, in which $U_{max} \sim V_{app}^2$.

The problem with this result is that it contradicts all of the experimental observations where the thrust force produced by a plasma actuator [20] and the maximum velocity induced by the actuator [61] were observed to increase as $V_{app}^{7/2}$. The difference in the voltage dependence can be explained by the fact that the electro-static model does not account for charge build-up on the surface of the dielectric or change in the volume of the plasma produced as a function of the

input amplitude. Therefore there is the need for a better model that can account for these effects. That model is the topic of the next Chapter.

CHAPTER 4

LUMPED-ELEMENT CIRCUIT MODEL

In order to improve upon the electrostatic model for the plasma actuator presented in the previous chapter, two different lumped-element circuit models were examined. The purpose of the lumped element circuit approach was to account for the fact that the basic actuator configuration is a capacitive element (two electrodes separated by a dielectric layer). In addition, the air is a resistive element that has properties that depend on the degree to which it is ionized. Starting with this basic formulation, two types of lumped-element models were considered. The first is a temporal model with a fixed number of circuit elements. The second is a space-time model that uses a large number of elements and can determine such features as the plasma maximum extent and sweep velocity a priori.

4.1 Spatial Lumped-Element Circuit Model

4.1.1 Mathematical Formulation

The spatial lumped-element model uses a fixed number of circuit elements to represent the actuator and air. This method was first suggested by Enloe [17]. The model, shown in Figure 4.1, consists of a number of capacitive elements, and a single resistive element, representing the plasma. Each of these elements varies

in time as the plasma discharge evolves throughout the AC cycle of the applied voltage.

The exposed surface of the dielectric also plays a critical role in the circuit dynamics. Even before the air ionizes, the dielectric surface communicates the potential charge from the covered electrode. When the voltage potential is large enough to ionize the air, the surface of the dielectric collects or discharges additional charge. As a result we refer to the dielectric surface as a virtual electrode in the circuit.

Three capacitances can be established in the circuit. Capacitance C_1 represents the capacitance between the exposed electrode and the top surface of the dielectric. Capacitance C_2 represents the capacitance between the top surface of the dielectric and the encapsulated electrode. Capacitance C_3 represents the capacitance between the two physical electrodes.

When the air is ionized, a portion of capacitance C_1 is bypassed by the conductivity of the plasma. This can be accounted for by splitting the capacitance C_1 into two elements: C_{1A} , which is bypassed when the plasma is present, and C_{1B} , which is not. The total capacitance remains constant throughout the discharge cycle, namely

$$C_{1A} + C_{1B} = C_1 = \text{Const.} \quad (4.1)$$

The same stipulation is made for the capacitance C_2 .

The values of the capacitancies C_{2A} and C_{2B} can be calculated as

$$C_{2A}(t) = \frac{\varepsilon_0 z x(t)}{d} \quad (4.2)$$

$$C_{2B}(t) = \frac{\varepsilon_0 z [L - x(t)]}{d}, \quad (4.3)$$

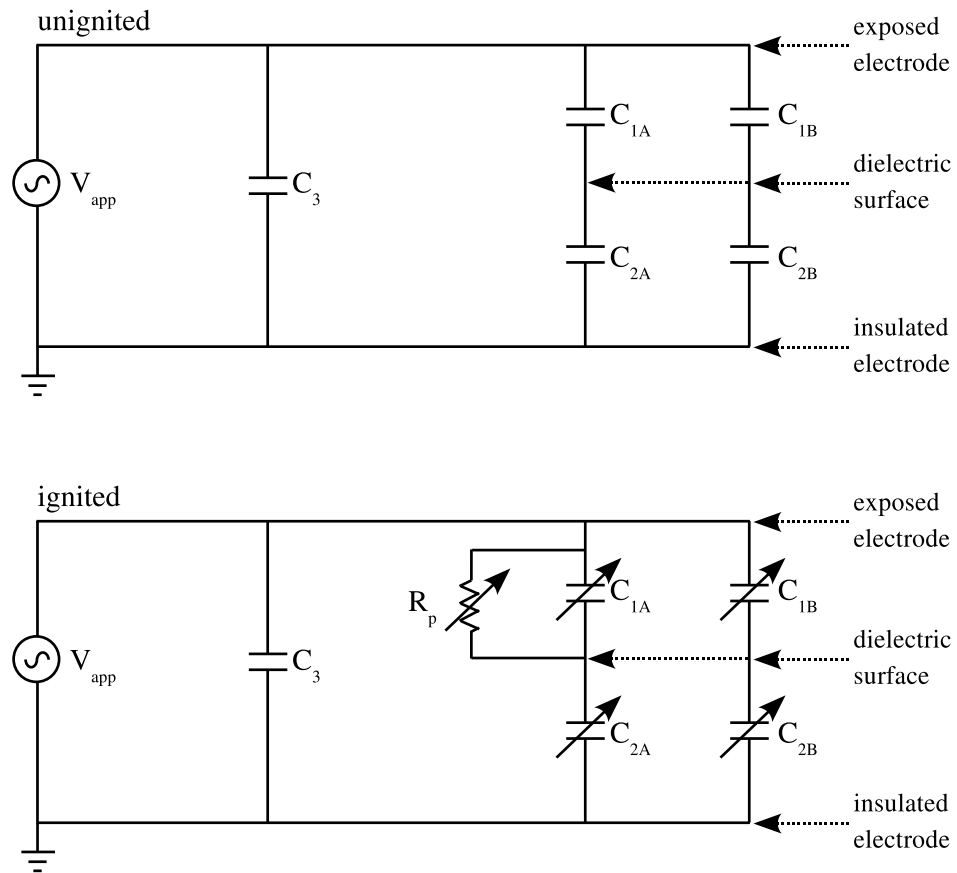


Figure 4.1. Spatial lumped-element circuit model of a single dielectric barrier discharge plasma actuator.

where d is the thickness of the dielectric, z is the span-wise length of the actuator, ϵ_0 is the permittivity of the free space, L is the length of the encapsulated electrode, and x is the extent of the plasma. Variables x , C_{2A} and C_{2B} are explicitly identified as functions of time, t .

Due to the complexity of the electrode geometry, calculating the capacitances C_{1A} and C_{1B} from first principles is less straightforward. But an assumption can be made that these C_{1A} and C_{1B} are proportional to C_{2A} and C_{2B} , respectively. Thus

$$C_{1A}(t) = \alpha C_{2A}(t) \quad (4.4)$$

and

$$C_{1B}(t) = \alpha C_{2B}(t) \quad (4.5)$$

where α is a constant that can be estimated from experiments. The capacitance C_3 is a constant that is given from the dielectric material properties and the area of the electrodes. it is easily estimated or found from experiment.

As the plasma expands over the dielectric, its resistance drops as the conduction path becomes wider. This variable resistance can be treated in the model by making the conductance of the plasma, G_p proportional to the extent of the plasma namely,

$$G_p(t) = \frac{1}{R_p(t)} = \left(\frac{G_0}{L} \right) x(t), \quad (4.6)$$

where G_0 is the conductance of the plasma when the plasma reaches its maximum extent at $x = x_{max}$. The value of G_0 depends on the geometry of the actuator, and the density and the temperature of the plasma. The conductance of the plasma can be measured in the experiment.

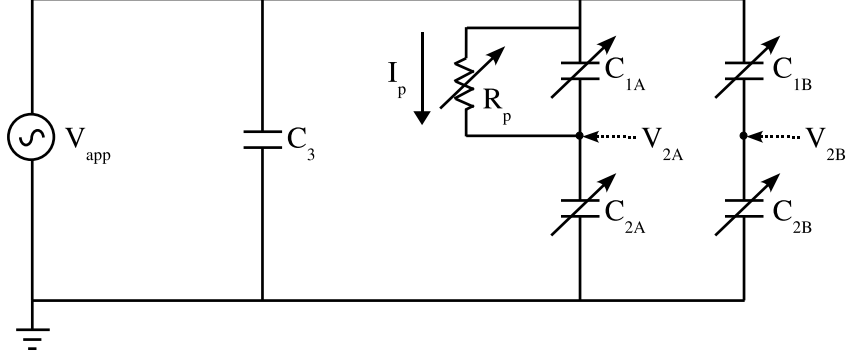


Figure 4.2. Schematic showing three node points where voltage is followed in the circuit in the spatial lumped-element circuit model of a single dielectric barrier discharge plasma actuator.

To implement the model, it is necessary to follow the voltage at three node points in the circuit as shown in Figure 4.2: the applied voltage V_{app} , which appears across the entire network, the voltage at the virtual electrode covered by plasma which is designated as V_{2A} , and the voltage at the virtual electrode not covered by plasma which is designated as V_{2B} . Due to the presence of the capacitances in the circuit, it is necessary to define the applied voltage V_{app} in terms of its time derivative. In the case of a simple sinusoidal input, this is

$$\frac{dV_{app}(t)}{dt} = V_0\omega \cos(\omega t), \quad (4.7)$$

where V_0 is the amplitude of the applied voltage and ω is its angular frequency.

The capacitance C_{2B} is charged and discharged by the displacement current flowing through the capacitance C_{2A} . The voltage across capacitor C_{2B} is V_{2B} which is governed by

$$\frac{dV_{2B}(t)}{dt} = \frac{dV_{app}(t)}{dt} \left(\frac{C_{1B}(t)}{C_{1B}(t) + C_{2B}(t)} \right). \quad (4.8)$$

The voltage at the virtual electrode covered by the plasma discharge is given by

$$\frac{dV_{2A}(t)}{dt} = \frac{dV_{app}(t)}{dt} \left(\frac{C_{1A}(t)}{C_{1A}(t) + C_{2A}(t)} \right) + \frac{I_p(t)}{C_{1A}(t) + C_{2A}(t)}. \quad (4.9)$$

This includes the real current through the plasma which is proportional to the plasma's conductance, G . The current flowing through the plasma is given as

$$I_p(t) = G_p(t) [V_{app}(t) - V_{2A}(t)]. \quad (4.10)$$

Starting from the moment of air ionization, the extent of spreading of the plasma over the dielectric covering of the lower electrode is given as

$$\frac{dx(t)}{dt} = \nu_V |V_{app}(t) - V_{2A}(t)|, \quad (4.11)$$

where ν_V is the coefficient representing the increase in the sweep velocity with the increase in applied voltage amplitude. The proportionality factor ν_V is empirically determined from experiments. In the present work, $\nu_V = 10 \frac{\text{m/s}}{\text{kV}}$ as seen in Figure 2.6. Because velocity of the plasma edge involves the absolute value of the voltage difference across the plasma, the plasma expands in essentially the same way regardless of the polarity of the ionization.

By solving the system of equations given by equations (4.7) through (4.11), the voltages at each node in the circuit, and the physical extent of the plasma can be determined as function of time. Examples of these and the sensitivity they have on some of the empirically determined variables are presented in the next section.

4.1.2 Numerical Formulation of Temporal Lumped-Element Circuit Model

The governing equations of the lumped-element circuit model, given by equations (4.9), (4.9) and (4.10), can be rewritten as

$$\begin{aligned}\frac{dV_{2B}(t)}{dt} &= \frac{dV_{app}(t)}{dt} \left(\frac{C_{1B}(t)}{C_{1B}(t) + C_{2B}(t)} \right), \\ \frac{dV_{2A}(t)}{dt} &= \frac{dV_{app}(t)}{dt} \left(\frac{C_{1A}(t)}{C_{1A}(t) + C_{2A}(t)} \right) + \frac{G_p(t) [V_{app}(t) - V_{2A}(t)]}{C_{1A}(t) + C_{2A}(t)}.\end{aligned}\tag{4.12}$$

From the first equation, the value of V_{2B} can be evaluated directly since the values of the capacitances are known at the time step t . The second equation is the initial value problem, which can be written in a more general case of a first-order ordinary differential equation as

$$\frac{dV_{2A}}{dt} = f(t, V_{2A}).\tag{4.13}$$

This initial value problem is solved using the standard IMSL routine IVPAG which implements the Adams-Moulton's method [1].

For this IVPAG routine, the time interval was specified along with the initial values of the voltage V_{2A} . As a solution we get the value of the voltage at the next time step.

The numerical procedure consists of the following steps:

1. Specify initial values for the temporal lumped-element circuit model at time $t = 0$;
2. Compute the voltage difference across the actuator, compare the value to the plasma ignition threshold value which determines the plasma presence on the dielectric surface;

3. Solve the lumped-element circuit model equations at time t for the non-ionized air if the plasma is not present and for the ionized air if the plasma is present on the surface;
4. Get the values of the voltage on the surface of the dielectric V_{2A} and V_{2B} at time t and the extent of the plasma $x(t)$ at time $t + \delta t$;
5. Increase the time t by δt and return to Step 2.

4.1.3 Results

In the results presented here, the a.c. input had an amplitude of $V_{app} = 20$ kV _{$p-p$} , and a frequency $f = 3$ kHz. The threshold voltage at which the ionization initiated was taken to be $V_{on} = 2$ kV.

There are two unknown parameters in the system: the ratio of the capacitances of the air and the dielectric defined as α , and the maximum conductivity of the plasma, defined as G . These two parameters were estimated by making comparisons between the simulation results and experiments. Examples of the dependence of the simulation results on these two parameters are shown by the voltage traces in Figures 4.3 and 4.4. This shows time series plots of the applied voltage, V_{app} , the voltage at the dielectric surface, V_{2A} , and the voltage difference across the plasma, $V_{app} - V_{2A}$, for a value of $G = 10^{-4}$ mho and values of $\alpha = 0.1, 0.2, 0.3, 0.4$.

The voltage on the surface of the dielectric follows the applied voltage with some small phase shift. The difference between the applied voltage and the voltage on the surface of the dielectric defines if the air is ionized in the region. When this difference is less than the threshold level, the air is not ionized. When the

voltage difference, $V_{app} - V_{2A}$, exceeds the threshold, the air is ionized. As noted in experiments presented earlier, the air is ionized twice during the a.c. cycle.

The simulations indicate that a change in the parameter G (for any fixed α) has a more significant effect on the solution behavior than a change in α for a given value of G . In particular, G has a large effect on the maximum extent of the plasma, and therefore, on the value of the plasma resistance. Based on experiments, the plasma resistance for typical actuator configuration was of the order of $10\text{ k}\Omega$. This gives a value of $G = 0.0001\text{ mho}$. We observed that for $G = 10^{-4}$ and a range of α from 0.1 to 0.4, the phase shift and extent of when the plasma formed with respect to the applied voltage a.c. period was similar to what we observed in experiments. As an example to illustrate this, time traces of the applied voltage and measured current passing between the electrodes from an experiment is shown in Figure 4.5. The current in this case was rectified before plotting to simulate the time series we would obtain from the PMT that is proportional to the plasma illumination. As previously shown, the current through the plasma correlates with the presence of the ionized air. In the time series of the current, the band with the high frequency spikes defines the period of time where the air was ionized. Comparing the points in the a.c. period of the applied voltage where the air was ionized in the experiment to points in the simulation where the voltage difference is above the threshold shows a qualitative similarity. We chose to use $\alpha = 0.2$ for the results to follow, although any value between 0.1 and 0.4 would have been equally as satisfactory.

The total current flowing through the actuator is a sum of the current flowing through the plasma, I_p , and the displacement currents in the dielectric capacitive

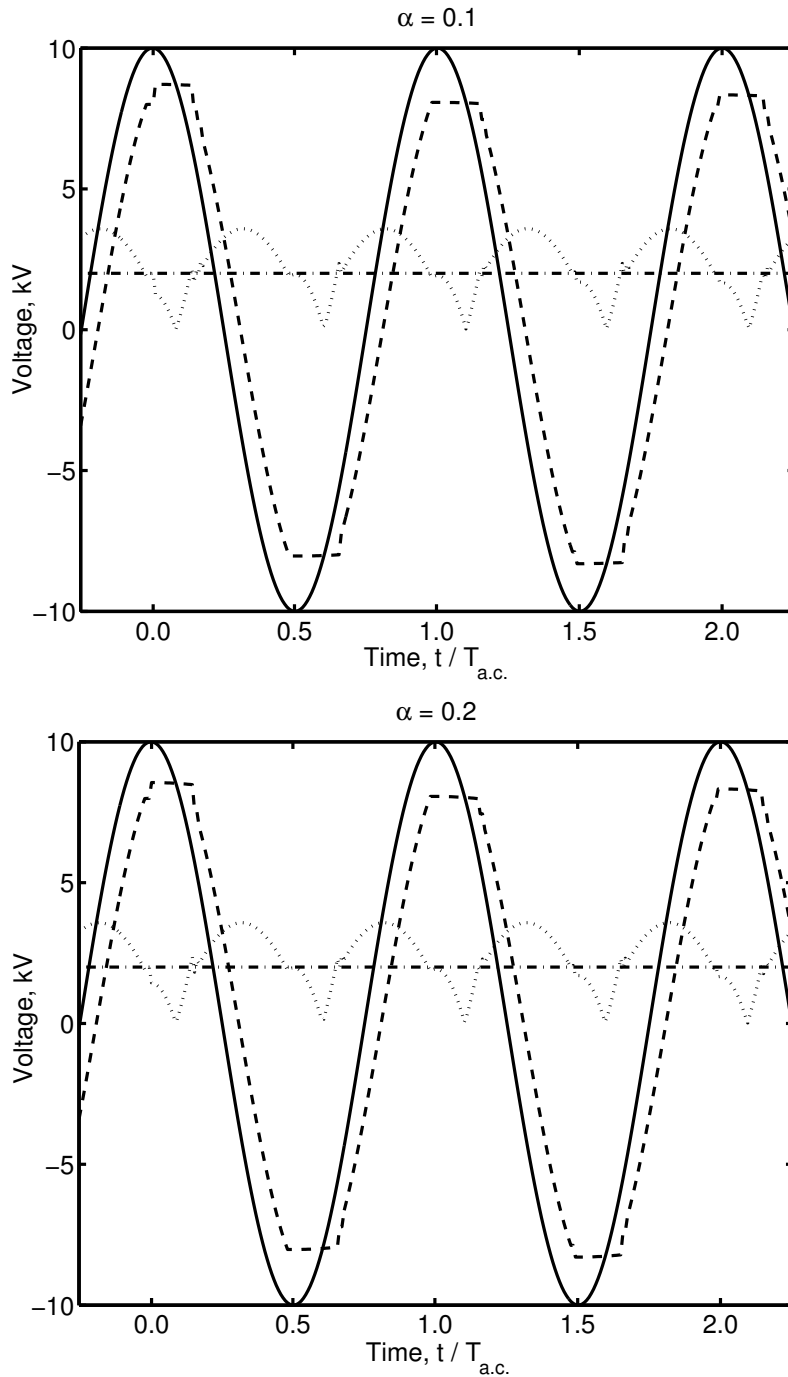


Figure 4.3. Voltage time series for $\alpha = 0.1$ and $\alpha = 0.2$: applied voltage (solid line), surface voltage (dashed line), voltage difference (dotted line), and plasma threshold (dash-dotted line).

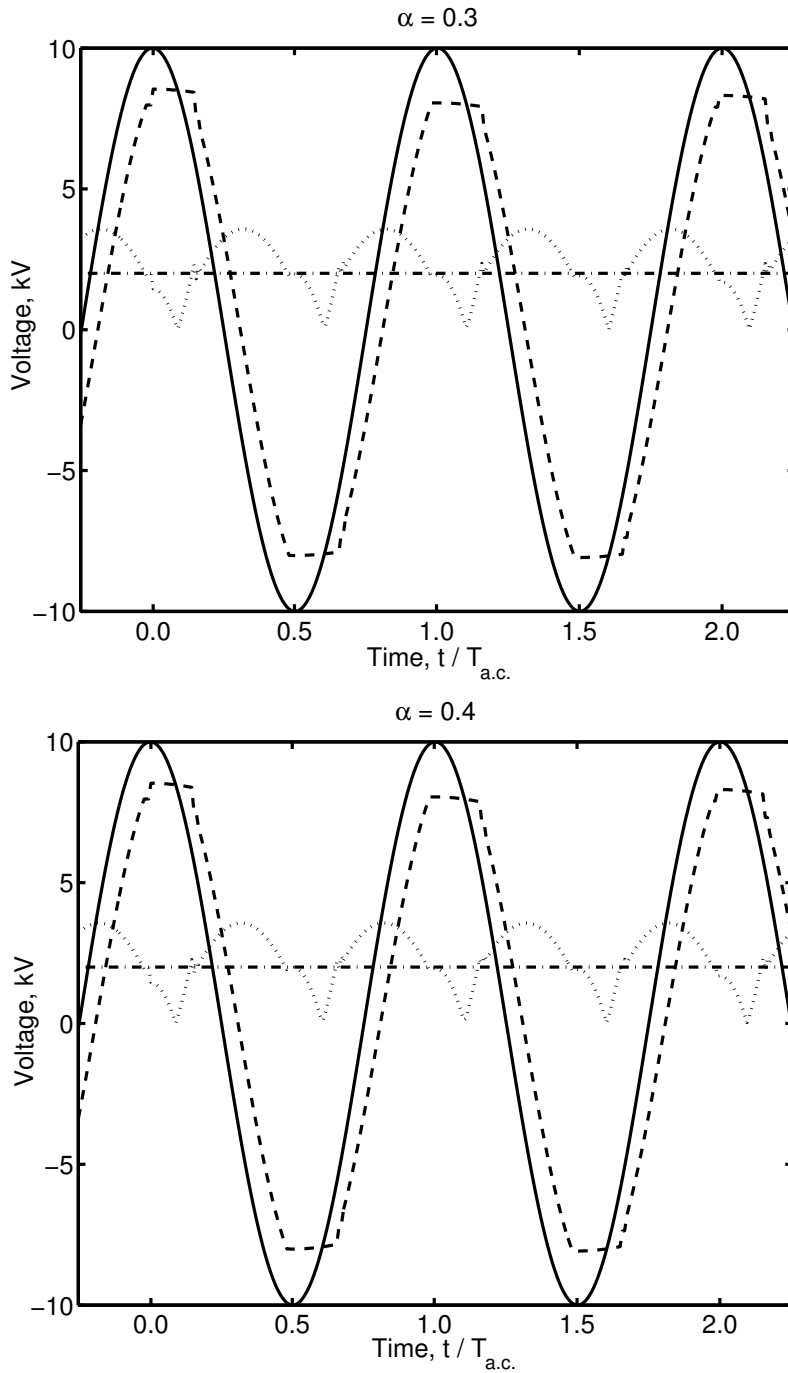


Figure 4.4. Voltage time series for $\alpha = 0.3$ and $\alpha = 0.4$: applied voltage (solid line), surface voltage (dashed line), voltage difference (dotted line), and plasma threshold (dash-dotted line).

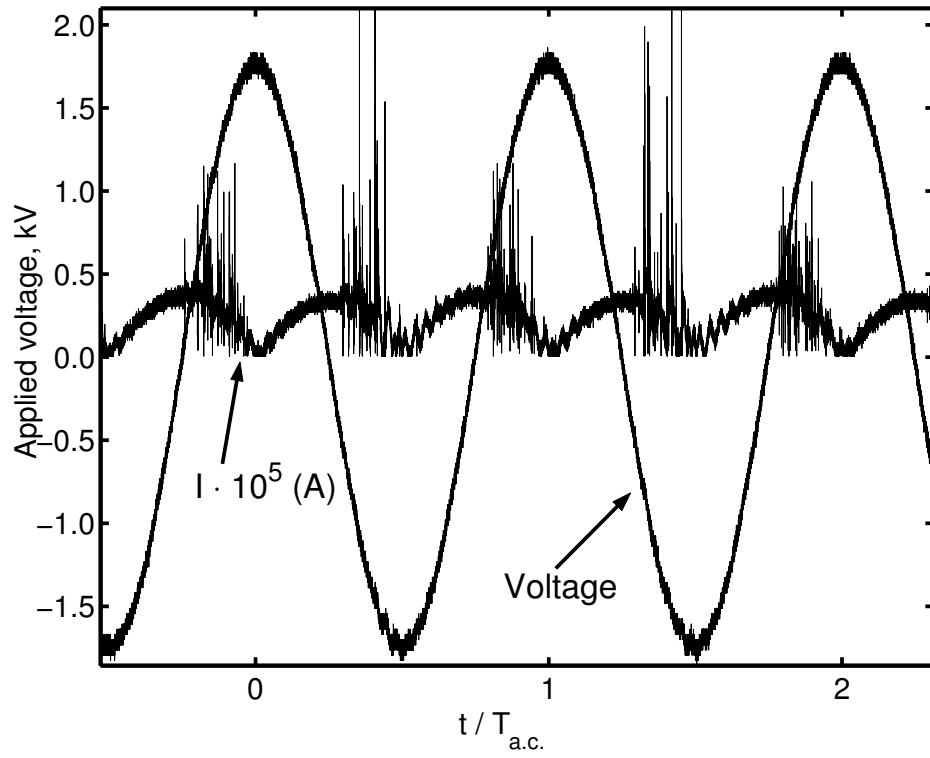


Figure 4.5. Applied voltage and rectified current in the circuit, experimental results.

element. This is given as

$$I_{total} = I_p + \frac{d(C_1 U_{1A})}{dt} + \frac{d(C_2 U_{2A})}{dt} + C_3 \frac{dV_{app}}{dt}. \quad (4.14)$$

The current flowing through the plasma was given by Equation (4.10). We note that the displacement currents in the dielectric capacitor elements are several orders of magnitude smaller than I_p . This current will be used to determine the power dissipated by the plasma.

The plasma is the only dissipative element in the circuit. Due to this, the instantaneous power $P(t)$ is given as

$$P(t) = I_p(t) |V_{app}(t) - V_{2A}(t)|. \quad (4.15)$$

The average dissipated power as a function of the applied voltage is shown in Figure 4.6. This is plotted on log axes to illustrate the power law relation between the dissipated power and voltage. Except for the lowest voltage, the dissipated power is proportional to the applied voltage to the 7/2 power. This is consistent with actuator thrust measurements by Enloe [20] and induced velocity measurements from Post [61] that both showed a 7/2 power-law dependence with the applied voltage.

The total volume of plasma is proportional to the plasma extent, $x(t)$. The dependence of the plasma extent on the input voltage amplitude has been examined in the previously discussed experiments. Model simulations were performed for a range of voltage from 10 kV_{p-p} to 40 kV_{p-p}. Figure 4.8 shows the model predictions for maximum extent of the plasma. Shown for comparison are the experimental values from our experiment and from Enloe *et al.* [20]. All agree

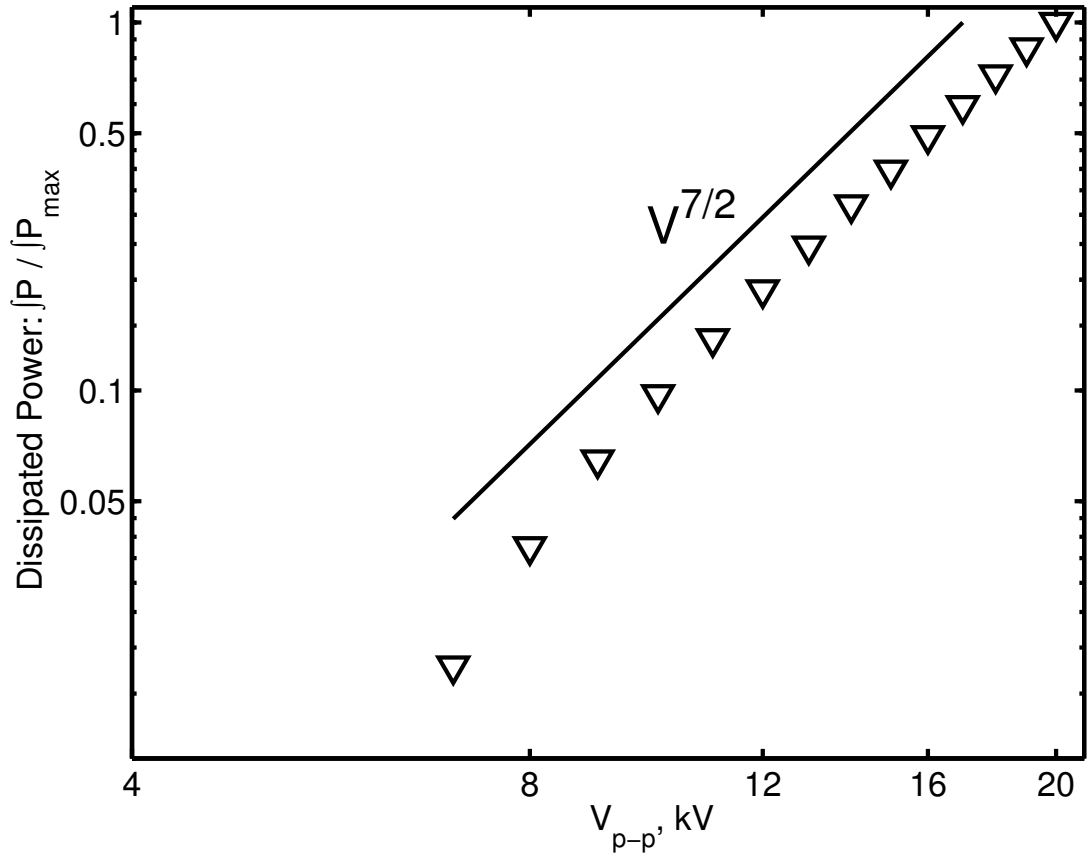


Figure 4.6. Average dissipated power as a function of the applied voltage based on the actuator model.

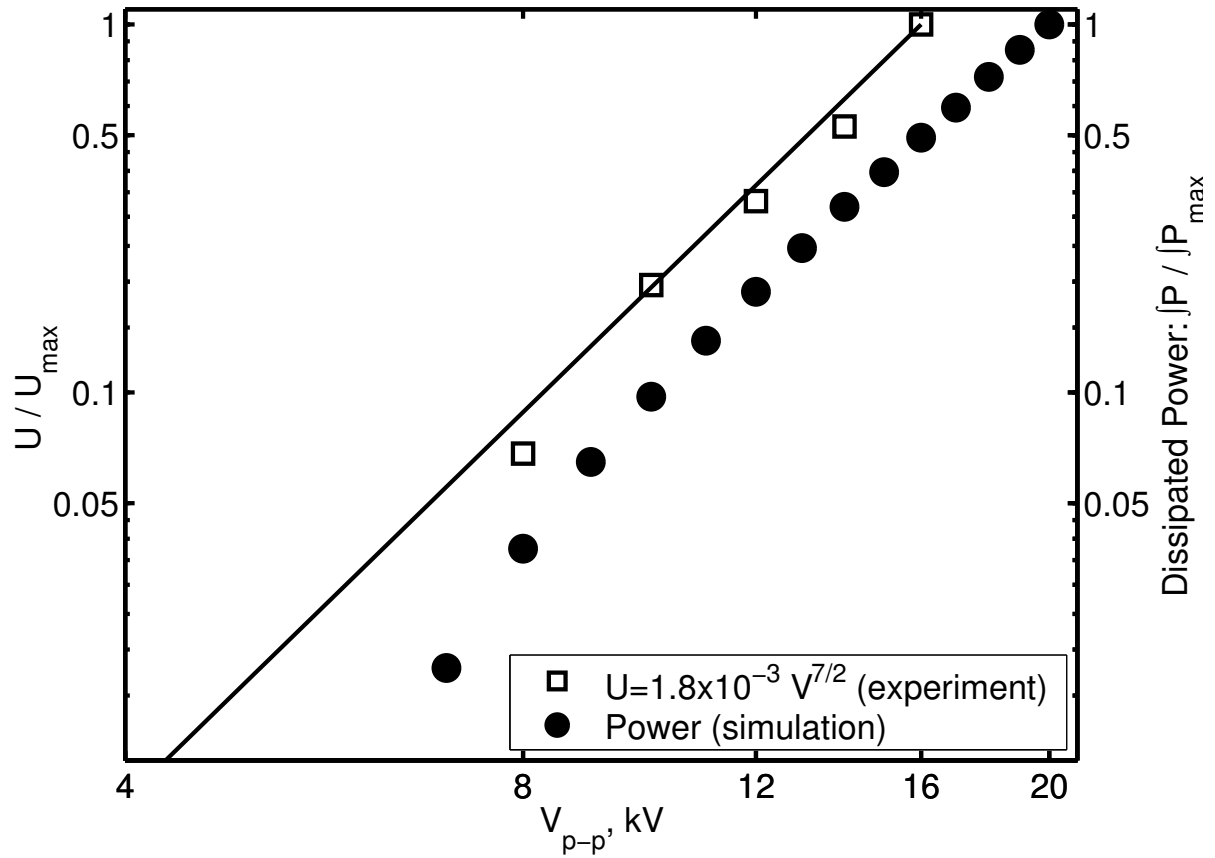


Figure 4.7. Dependence of plasma actuator maximum induced velocity (open symbols) and plasma dissipated power based on lumped-element circuit model (closed symbols) as a function of applied a.c. voltage.

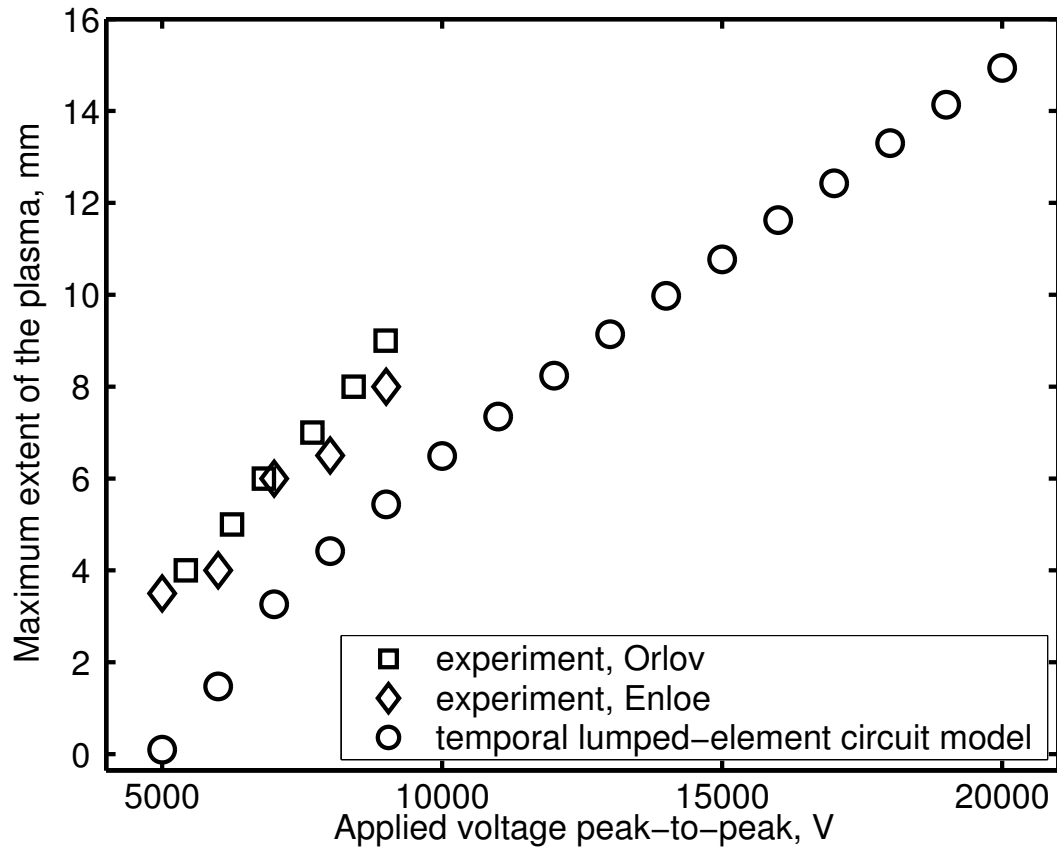


Figure 4.8. Maximum extent of the plasma as function of applied voltage amplitude for temporal lumped-element circuit model simulation and experiments (Enloe [20] and present).

reasonably well. They indicate that the maximum extent increases linearly with the applied voltage at a rate of approximately 1.25 mm/kV. This is important because it has been shown by Enloe *et al.* [20] that the thrust of the actuator was limited if sufficient area of the covered electrode was not provided. That minimum area is a function of the voltage.

The present model was successful at estimating the effect of voltage amplitude on the body force and power dissipated by the plasma. In particular, the voltage

dependence of the body force was found to agree with the experimental observations by Enloe [20] and Post [61]. A shortcoming of the model was that it needed some empirically determined coefficients that were shown in experimental results presented in Chapter 2, to be functions of frequency. Thus the present model is only valid for the single frequency. Although, it might be possible to modify this model to include a broader set of coefficients, the desire was to develop a model that embodies more of the physics of the DBD process without the need of experimental coefficients. The attempt at that model which we term the space-time lumped-element model, is presented in the next section.

4.2 Spatial-Temporal Lumped-Element Circuit Model

4.2.1 Mathematical Formulation

As it has been shown previously, the spatial lumped-element circuit model correctly describes many of the characteristics of the SDBD plasma actuator. By comparisons with experimental results, it was shown that the model predicts that the power dissipated in the plasma resistive element increases with the $7/2$ power of the applied voltage. This correlates with the experimental results by Enloe *et al.* [20] and Post [62] that showed that thrust and maximum velocity generated by the asymmetric electrode arrangement of the SDBD plasma actuator varied as $V_{app}^{7/2}$.

Despite all the advantages of the earlier model, it had a significant limitation in that the dynamics of the ionization relied on empirical coefficients that were functions of the applied voltage amplitude and frequency. Therefore the model was not able to predict the actuator dependence outside its empirical calibration space.

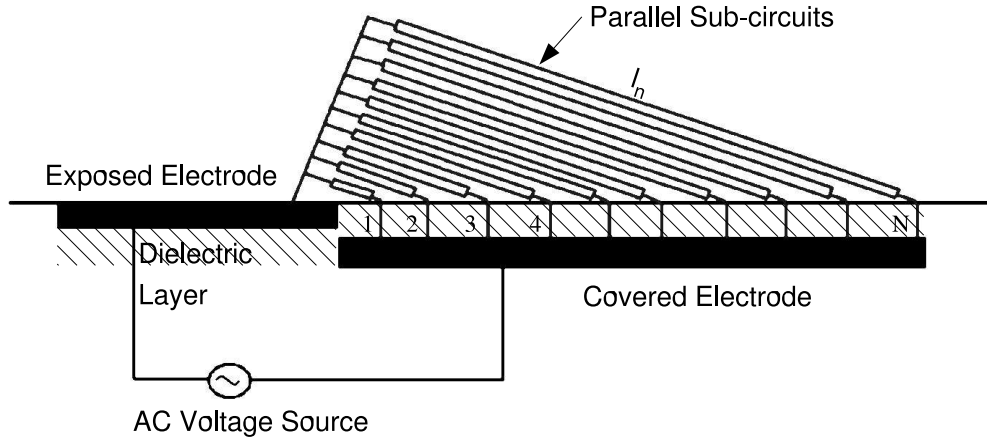


Figure 4.9. The physical space over the encapsulated electrode is divided into N sub-regions.

The space-time lumped-element circuit model presented here is intended to model the details of the ionization process to provide predictions of the body force for a range of parameters without the need of experimental calibration. The space-time lumped-element model follows from the previous model in that the air and dielectric are represented as a network of resistors and capacitors. The difference comes in that rather than being represented by a single parallel network, the domain over the covered electrode is divided into N parallel networks, such as illustrated in Figure 4.9. The characteristics of each parallel network depend on its distance from the exposed electrode. For example, parallel network 1 is closest to the exposed electrode and extends the shortest distance over the covered electrode. Parallel network N extends the farthest distance over the covered electrode.

Each parallel network consists of an air capacitor, a dielectric capacitor, and a plasma resistive element as in the previous model. In addition to these, zener diodes were added to set the threshold voltage levels at which the plasma initiates, and to switch in the different plasma resistance values based on the current

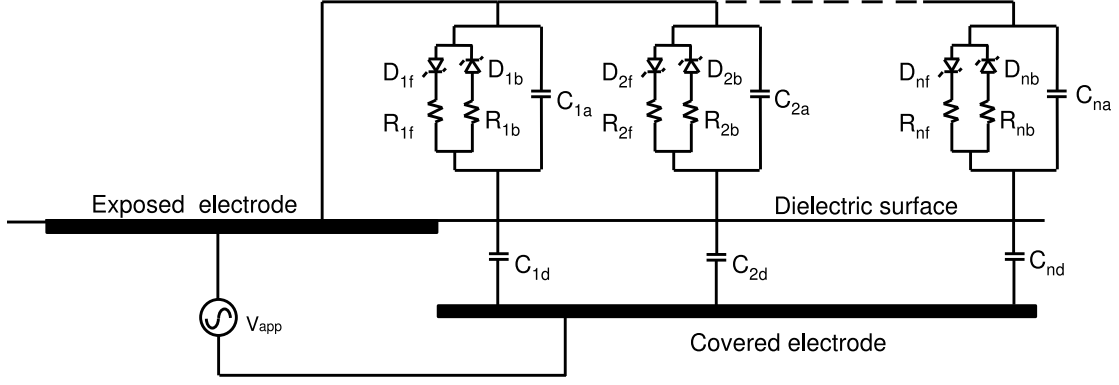


Figure 4.10. Electric circuit model of a single dielectric aerodynamic plasma actuator.

direction, namely from the exposed electrode to the dielectric, or from the dielectric to the exposed electrode, that experiments have shown to be important. The N-circuit arrangement is shown in Figure 4.10.

The value of the air capacitor in the n -th sub-circuit is based on its distance from the edge of the exposed electrode. This is given by equation (4.16)

$$C_{an} = \frac{\varepsilon_0 \varepsilon_a A_n}{l_n} \quad (4.16)$$

where ε_a is the dielectric coefficient of air, l_n is the representative distance over the dielectric surface, and A_n is the cross section of this air capacitor. The cross-section A_n is the product of the span-wise size of the actuator, z_n , and the height of the capacitive element, h_n . The schematic of this capacitive element is shown in Figure 4.11.

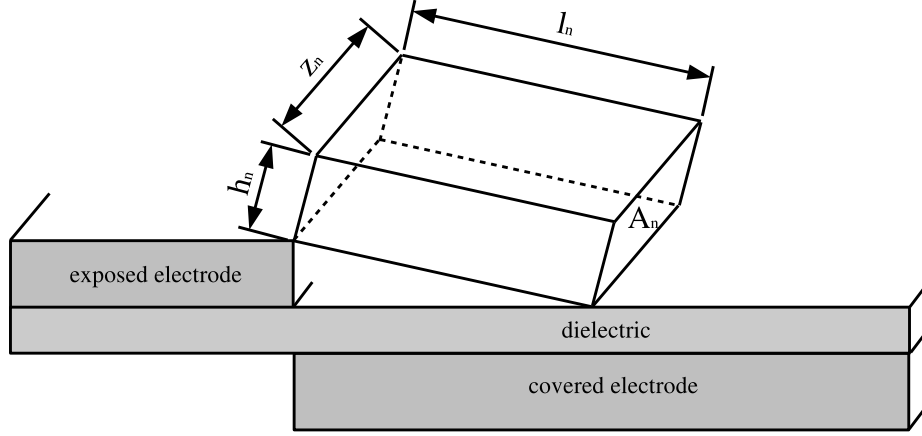


Figure 4.11. Schematic drawing of the n -th air capacitor.

The resistance value in the n -th sub-circuit is similarly based on its distance from the exposed electrode. It is given by equation (4.17)

$$R_n = \frac{\rho_a l_n}{A_n} \quad (4.17)$$

where ρ_a is the effective resistivity of the air.

The value of the dielectric capacitor for each sub-circuit is similar to the air capacitance except that it is based on the properties of the dielectric material. It is given by equation (4.18)

$$C_{dn} = \frac{\varepsilon_0 \varepsilon_d A_d}{l_d} \quad (4.18)$$

where ε_d is the dielectric coefficient of the dielectric material, l_d is the thickness of this material, and A_n is the cross section which is equal to the product of the span-wise size of the actuator, z_n , and the width of the dielectric capacitive element, d_n , as shown in Figure 4.12.

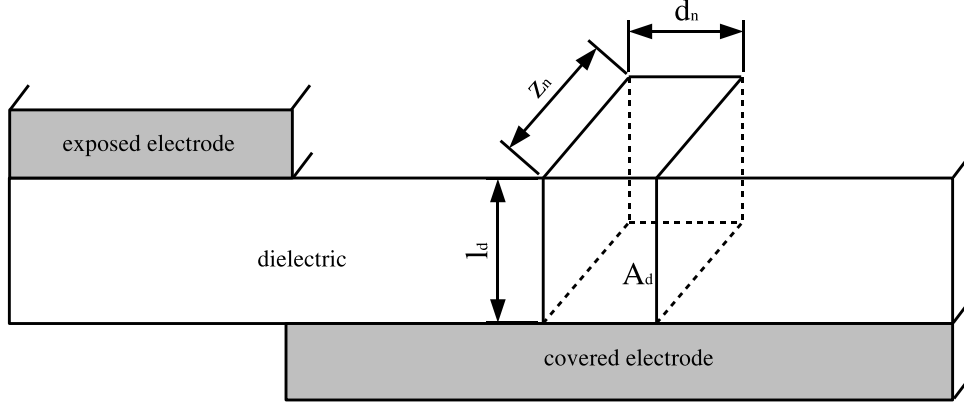


Figure 4.12. Schematic drawing of the n -th dielectric capacitor.

If we assume that the paths are parallel to each other, and the length of path l_n is proportional to its position number n , then it follows that the the air capacitance of the n -th sub-circuit, C_{an} , is proportional to $1/n$, and the air resistance of the n -th sub-circuit is proportional to n . Therefore sub-circuits that are furthest from the edge of the electrodes, would have the lowest air capacitance and the largest air resistance.

For a time-varying applied voltage, the voltage on the surface of the dielectric at the n^{th} parallel network is given as

$$\frac{dV_n(t)}{dt} = \frac{dV_{app}(t)}{dt} \left(\frac{C_{an}}{C_{an} + C_{dn}} \right) + k_n \frac{I_{pn}(t)}{C_{an} + C_{dn}}, \quad (4.19)$$

where $I_{pn}(t)$ is the time varying current through the plasma resistor. The zener diode in the parallel network has two functions. The first is setting a threshold on the voltage differential between the exposed electrode and the dielectric surface above which the air is ionized (plasma formed). In equation (4.19), the diodes are

represented by the variable k_n . When the threshold voltage is exceeded, $k_n = 1$. Otherwise $k_n = 0$.

The second function of the zener diodes was to switch in either one of the resistances representing the plasma resistance based on the direction of the current, from the exposed electrode to the dielectric surface or vice versa. This is meant to represent the experimental observations that the current and corresponding plasma illumination were different based on the current direction. The resistance values are designated as R_{nf} or R_{nb} (representing forward or backward going current). The ratio of the two plasma resistances used in the simulation were $\frac{R_{nf}}{R_{nb}} = 5$. This was based on the difference in the estimated current observed in experiments. With this background, the current through the plasma resistance, $I_p(t)$ is given as

$$I_{pn}(t) = \frac{1}{R_n} [V_{app}(t) - V_n(t)]. \quad (4.20)$$

where $R_n = R_{nf}$ or R_{nb} based on the current direction.

This space-time formulation of the lumped-element circuit model has many advantages over the previous model. One advantage is that it allows us to specify the number of the sub-circuits N making up the actuator. Ideally, as $N \rightarrow \infty$, the numerical solution should approach the asymptotic solution. As the tests of the code showed, values of $N \approx 10^2$ appear to be sufficient to capture the essential physics. This is shown in Figure 4.13.

A second advantage of this formulation is that it is temporal. Therefore the effect of the a.c. frequency or wave form can be examined. Dynamics such as the sweep-out velocity of the plasma can then be determined a priori.

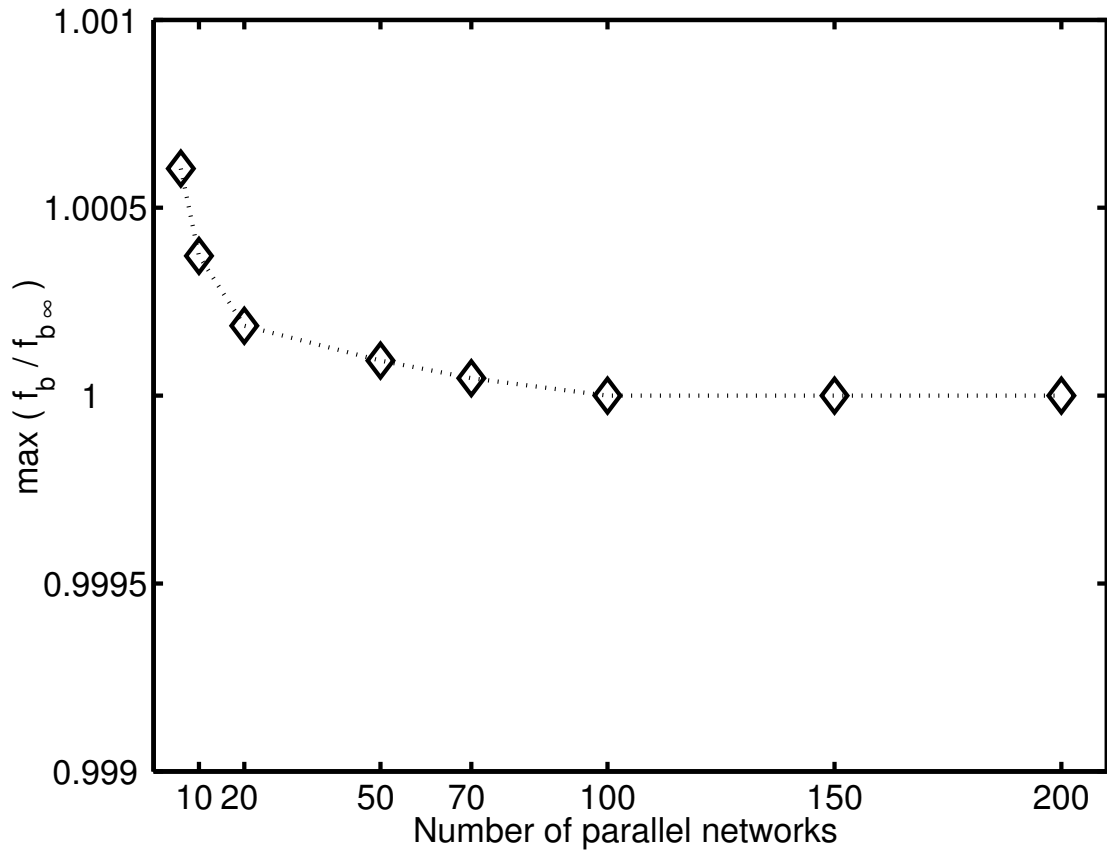


Figure 4.13. Maximum value of the plasma body force as function of the number of parallel networks.

4.2.2 Numerical Formulation of Space-Time Lumped-Element Circuit Model

The governing equations of the lumped-element circuit model, given by equations (4.19) and (4.20), can be rewritten as

$$\frac{dV_n(t)}{dt} = \frac{dV_{app}(t)}{dt} \left(\frac{C_{an}}{C_{an} + C_{dn}} \right) + k_n \frac{\frac{1}{R_n} [V_{app}(t) - V_n(t)]}{C_{an} + C_{dn}}. \quad (4.21)$$

This is a typical initial value problem, and it can be written in general form as

$$\frac{dV_n}{dt} = f(t, V_n), \quad (4.22)$$

or as a finite difference equation

$$\delta V_n = f(t, V_n) \delta x \quad (4.23)$$

This equation is solved using the standard Runge-Kutta 45 method. In this method, we made two mid-point derivative evaluations, which led us to the following equations:

$$\begin{aligned} k_1 &= \delta t f(t^m, V_n^m), \\ k_2 &= \delta t f\left(t^m + \frac{1}{2}\delta t, V_n^m + \frac{1}{2}k_1\right), \\ k_3 &= \delta t f\left(t^m + \frac{1}{2}\delta t, V_n^m + \frac{1}{2}k_2\right), \end{aligned} \quad (4.24)$$

$$k_4 = \delta t f\left(t^m + \frac{1}{2}\delta t, V_n^m + \frac{1}{2}k_3\right), \quad (4.25)$$

and the voltage on the next time step can be calculated from the previous time step using the following equation

$$V_n^{m+1} = V_n^m + \frac{k_1}{6} + \frac{k_2}{3} + \frac{k_3}{3} + \frac{k_4}{6} + O(\Delta t^5). \quad (4.26)$$

This method is implemented using the standard MATLAB function *ode45* [5]. In MATLAB the Runge-Kutta routine uses a variable, continuously adjusted time step. The adaptive time-stepping algorithm takes small steps where the function is changing rapidly and can take really big time steps where the function is smooth and not varying much.

For the initial conditions at $t = 0$ we took $V_n = 0$ on the surface of the dielectric. On each of the next time steps the initial conditions on V_n were taken from the solution on the previous time step.

Thus, the procedure consists of the following step.

1. Calculate the values of resistances and capacitances in each of the parallel networks;
2. Specify initial values of the voltage on the dielectric surface at time $t = 0$;
3. Specify the time step δt ;
4. Specify the time interval: $[t, t + \delta t]$;
5. Solve the ODE given by equation (4.21) using the *ode45* routine in MATLAB on the specified time interval;
6. Check for the plasma presence in all the parallel networks, if the plasma is present in the n -th network, set the plasma presence coefficient $k_n = 1$,

- if the threshold for the plasma ignition is not reached in the n -th parallel network, then set $k_n = 0$;
7. Calculate the plasma current and set the resistance of the plasma depending on the direction of the plasma current;
 8. Reinitialize the initial values of the voltage on the surface for the ODE solver solution on this time step;
 9. Increase time by δt ;
 10. Return to Step 4.

4.2.3 Results of Space-Time Lumped-Element Circuit Model

As an example, the electric circuit equations (4.19) were solved for 100 parallel circuit elements making up a SDBD actuator. For this, the applied voltage was a sine wave with amplitude of $5 kV_{p-p}$, and a frequency of 5000 Hz. In order to resolve the dynamic motions of the plasma, a computational time step of $8 \cdot 10^{-7}$ seconds was used. This corresponded to 250 time steps within each cycle of the a.c. input period.

The solution of the model equations gives the voltage on the surface of the dielectric, V_n , for each parallel circuit element. An example of this for the first five circuit elements, closest to the exposed electrode, is shown in Figure 4.14. We observe that there is a shift in time of the peak voltage in successive current elements. This reflects the sweep out of the plasma over the dielectric surface.

Figure 4.15 shows the time series in the current through the first five circuit elements in the model. Plasma is formed where the current is non-zero. This is observed to occur twice per a.c. period at the time periods when the voltage

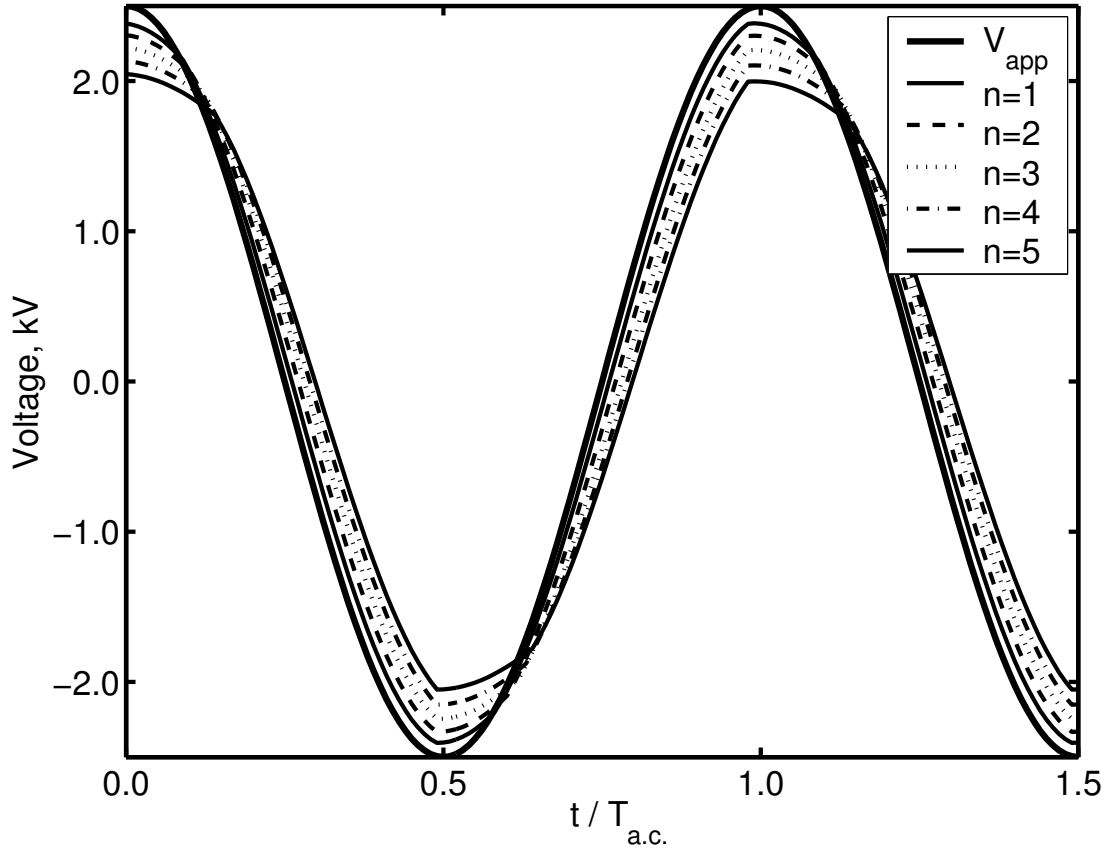


Figure 4.14. Voltage on the surface of the dielectric in the first five sub-circuits ($n=1,2,3,4,5$) obtained from space-time lumped element circuit model.

difference between the exposed electrode and dielectric surface exceeds a threshold level. Again we observe that the time when the plasma first forms increases as the sub-circuit is further from the exposed electrode. As with the voltage, this reflects the sweep out of the plasma during the input a.c. cycle.

It may be noticed that the plasma current is not symmetric during the a.c. cycle - the current going through the plasma resistive elements is larger during one half of the cycle than the current going in the opposite direction during the other half of the cycle. But the total current in the circuit is the sum of the real

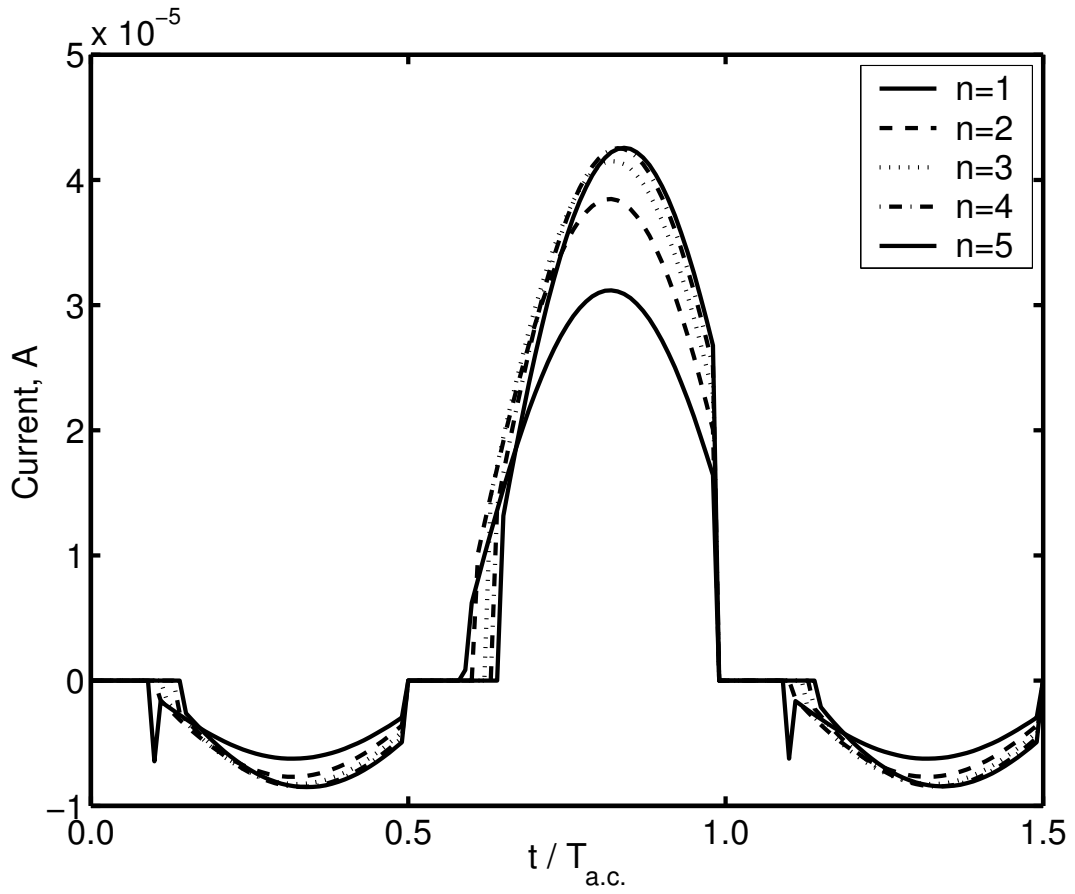


Figure 4.15. Plasma current in the first five sub-circuits ($n=1,2,3,4,5$) obtained from space-time lumped element circuit model.

and displacement currents in the parallel networks, and it can be written as

$$I_{total}(t) = \sum_{n=1}^N \left(I_{pn}(t) + \frac{d(C_{na}(V_{app}(t) - V_n(t)))}{dt} \right). \quad (4.27)$$

The charge transferred through the circuit is given by

$$Q_{total} = \int_{t=0}^1 I_{total}(t) dt. \quad (4.28)$$

Integrating the total current for one a.c. period, as given by Equations (4.27) and (4.28), we get

$$Q_{total} = 0. \quad (4.29)$$

This results signifies the conservation of charge in the system.

As has been noted previously in the experiments, the electric current in the plasma relates directly to the light emission from the SDBD, and thus is an indication of the volume of the plasma. Therefore to compare to the experiments, the rectified plasma current from the model in time and space above the dielectric-covered electrode is shown in Figure 4.16. Zero on the space axis corresponds to the edge of the exposed electrode. The time axis is shown as a fraction of the input a.c. period. This can be directly compared to Figure 2.4 that showed the space-time variation of the plasma illumination. The rectified current from the model is very similar to the experimental result. It clearly shows the largest current at the edge of the exposed electrode and the rapid decay when moving away from electrode's edge. In addition, the model simulates ionization occurring twice during the a.c. cycle, and the difference in the magnitude of the current in the two halves of the cycle.

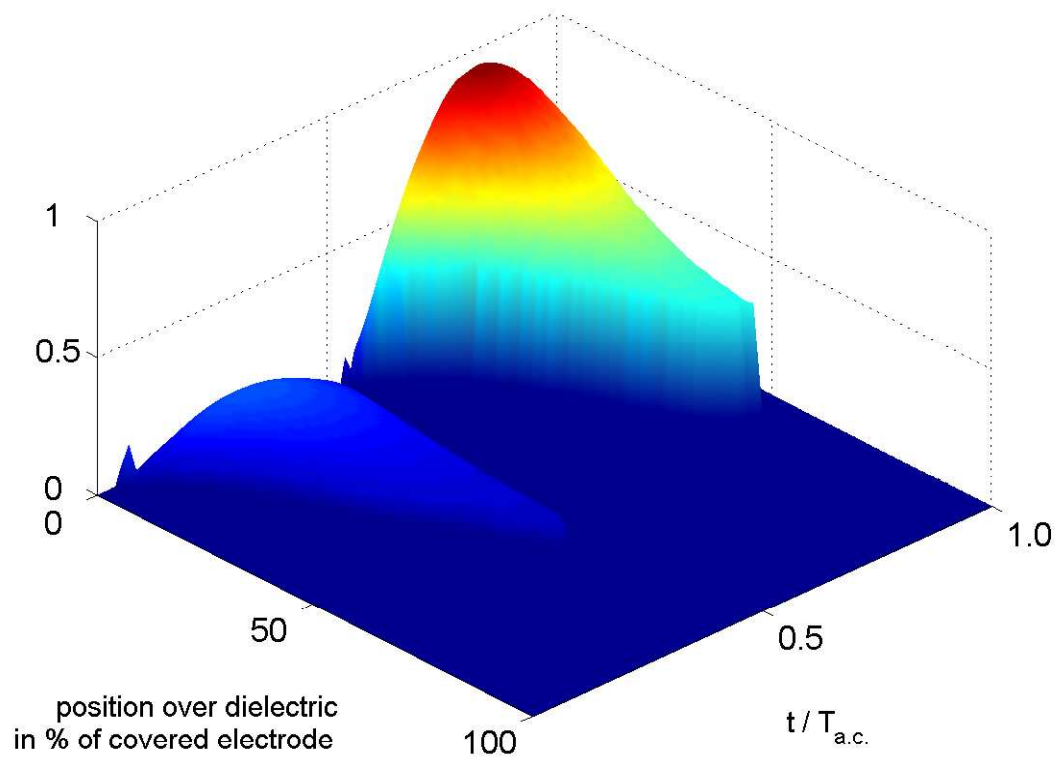


Figure 4.16. Rectified plasma current for one a.c. period of input obtained from space-time lumped element circuit model.

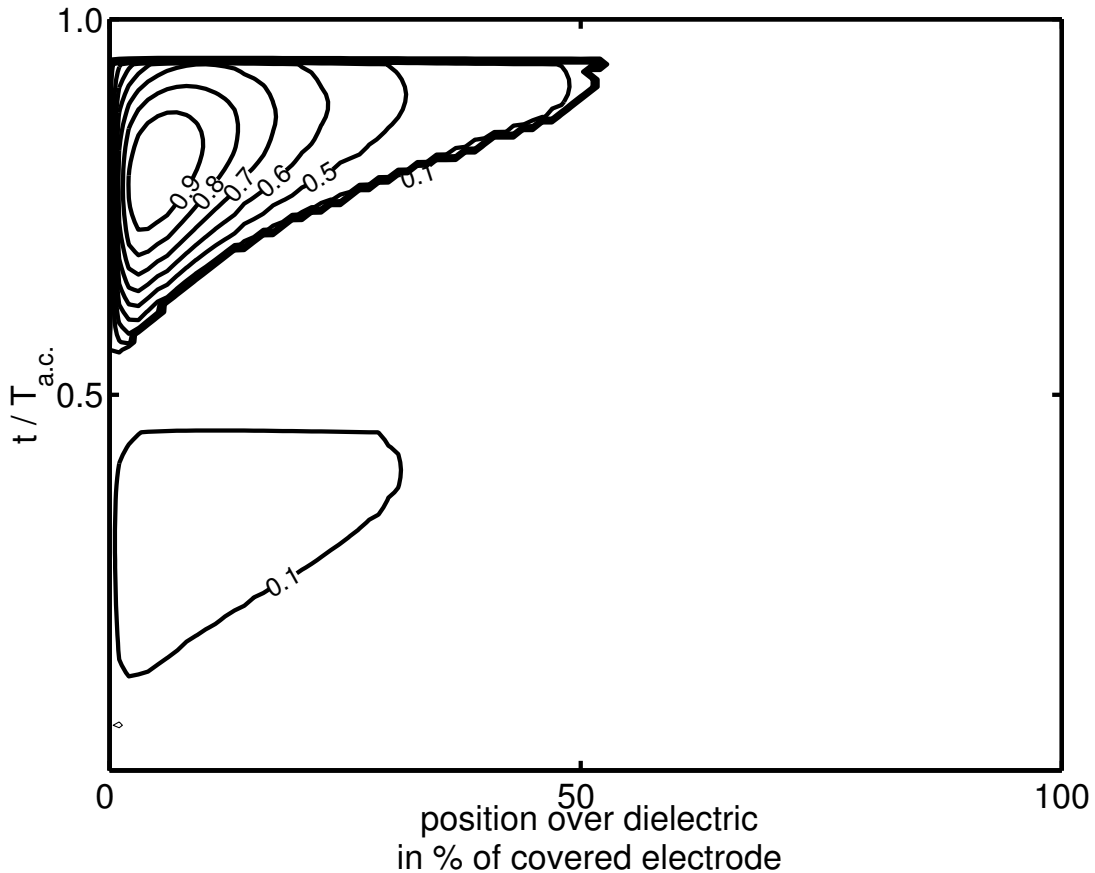


Figure 4.17. Contour lines of constant rectified plasma current obtained from space-time lumped element circuit model.

The same result shown in Figure 4.16 is plotted in Figure 4.17 as contour lines of the constant plasma current. This again illustrates the good agreement between the model and the photomultiplier experiments shown in Figure 2.5.

The results from the photomultiplier experiments and from the space-time lumped-element circuit model can be compared quantitatively. There are two important characteristics of the plasma discharge that can be extracted from this data. The first is the maximum extent of the plasma over the surface of the dielectric. The results from the model and experiments are shown in Figure 4.18.

Also included in the figure are experimental results from Enloe *et al.* [21]. The figure shows the extent of the plasma as a function of the peak-to-peak voltage. First, we notice that the plasma extent varies approximately linearly with the input voltage. Second, we observed very good agreement between the model results and the experimental results. The agreement with our experiment is better because the model used a dielectric coefficient for PC board material (glass-epoxy) which was used in our experiments. The experiments by Enloe *et al.* [21] used Kapton film which has a different dielectric coefficient and thickness.

This result is very important for the design of plasma actuator. Post [61] noted that at higher voltages, if the width of the covered electrode was too small, the magnitude of the induced velocity would asymptote. A similar result was found for the thrust produced by the actuator in experiments by Enloe *et al.* [21].

Another distinctive feature that can be compared is the sweep out velocity. This corresponds to the space-time slope of the outer edge of the light intensity contours. A comparison for the plasma sweep velocity between the space-time simulations and plasma illumination experiments are shown in Figure 4.19. Also included in the figure are results from the experiments of Enloe *et al.* [21]. The simulation shows that the plasma sweep velocity increases slightly with the applied voltage amplitude. The agreement with the experiment is very good. The range of sweep velocities is from 75 to 110 m/s.

Another set of numerical simulation has been performed to study the dependence of the major plasma characteristics, such as the maximum plasma extent over the surface of the dielectric and the plasma sweep velocity, on the applied a.c. frequency. These results were again compared to the experimental results. The comparison between the experimental results and the space-time lumped-element

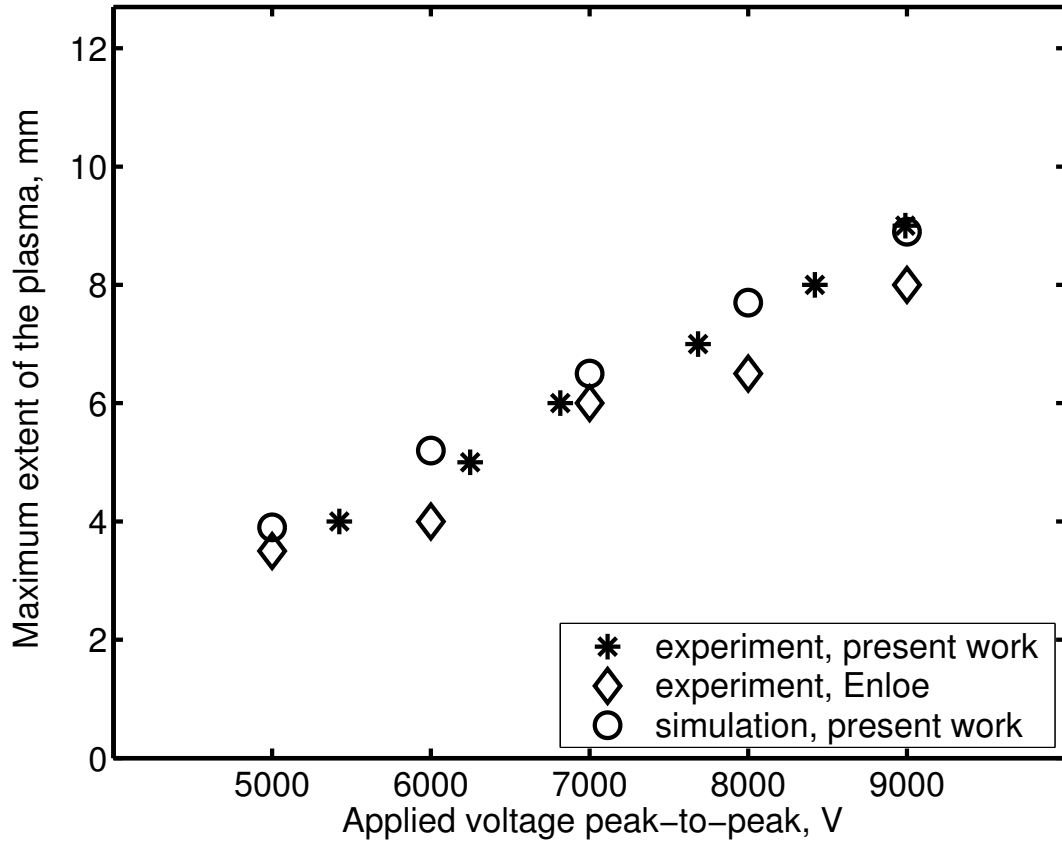


Figure 4.18. Comparison between space-time model and experiments for the maximum plasma extent over covered electrode as function of voltage.

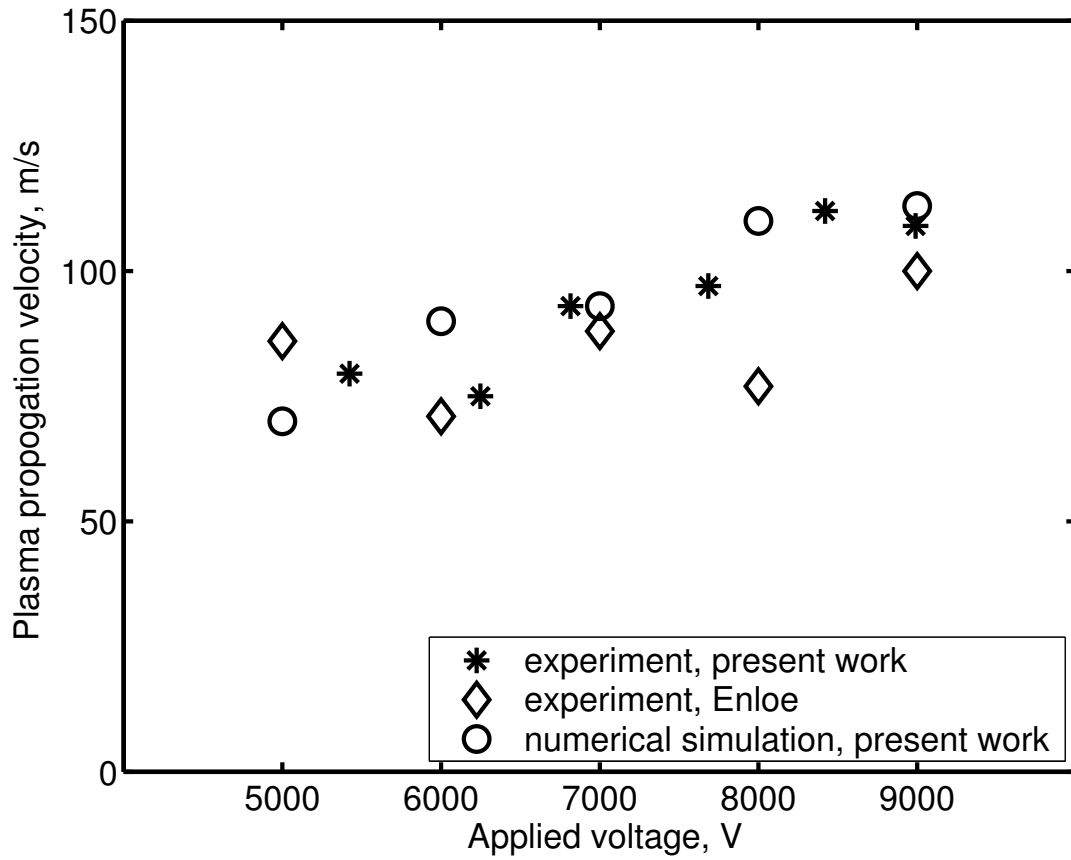


Figure 4.19. Comparison between space-time model and experiment for plasma sweep velocity as function of voltage.

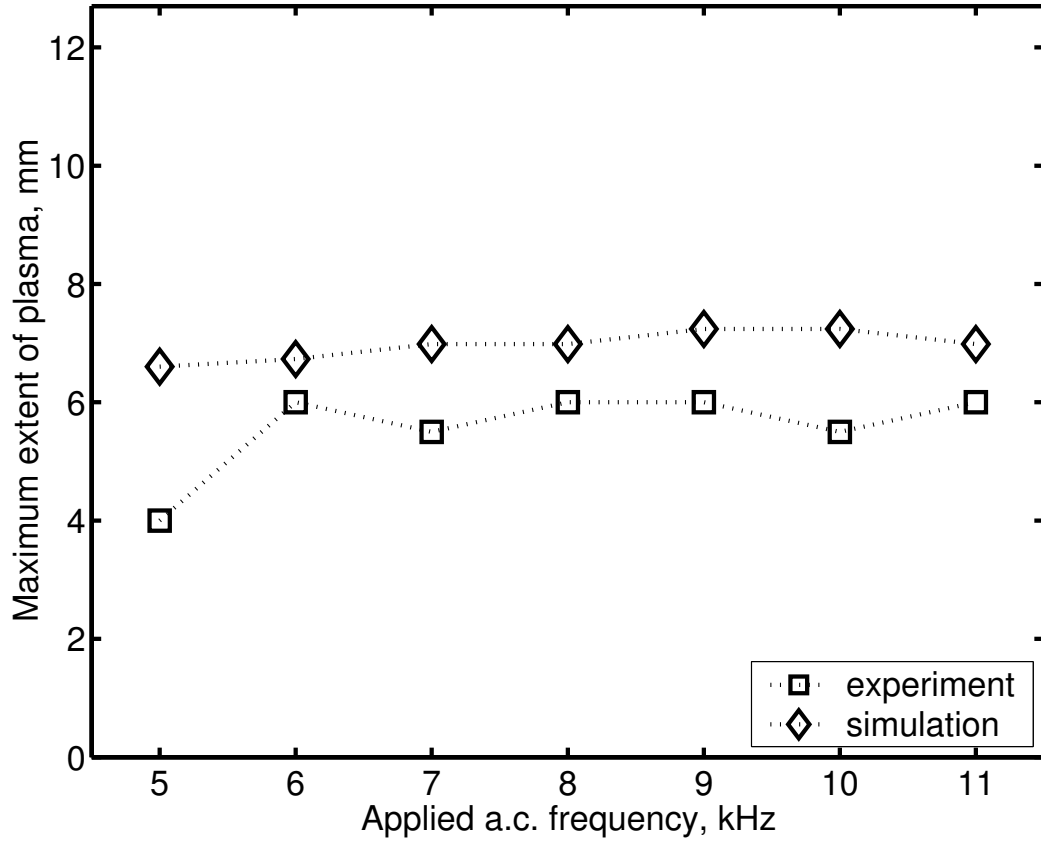


Figure 4.20. Comparison between space-time model and experiment for maximum extent of the plasma as function of applied a.c. frequency.

circuit model simulation are presented in Figures 4.20 and 4.21. As it can be seen in these figures, the model predicts that the maximum plasma extent over the encapsulated electrode does not increase with the increasing a.c. frequency. This also means that the plasma propagation velocity would increase linearly with the applied frequency. This is consistent with the experimental observations. The results obtained from the numerical simulation for the plasma sweep velocity are in the range of 75-200 m/s and match the experimental result very well.

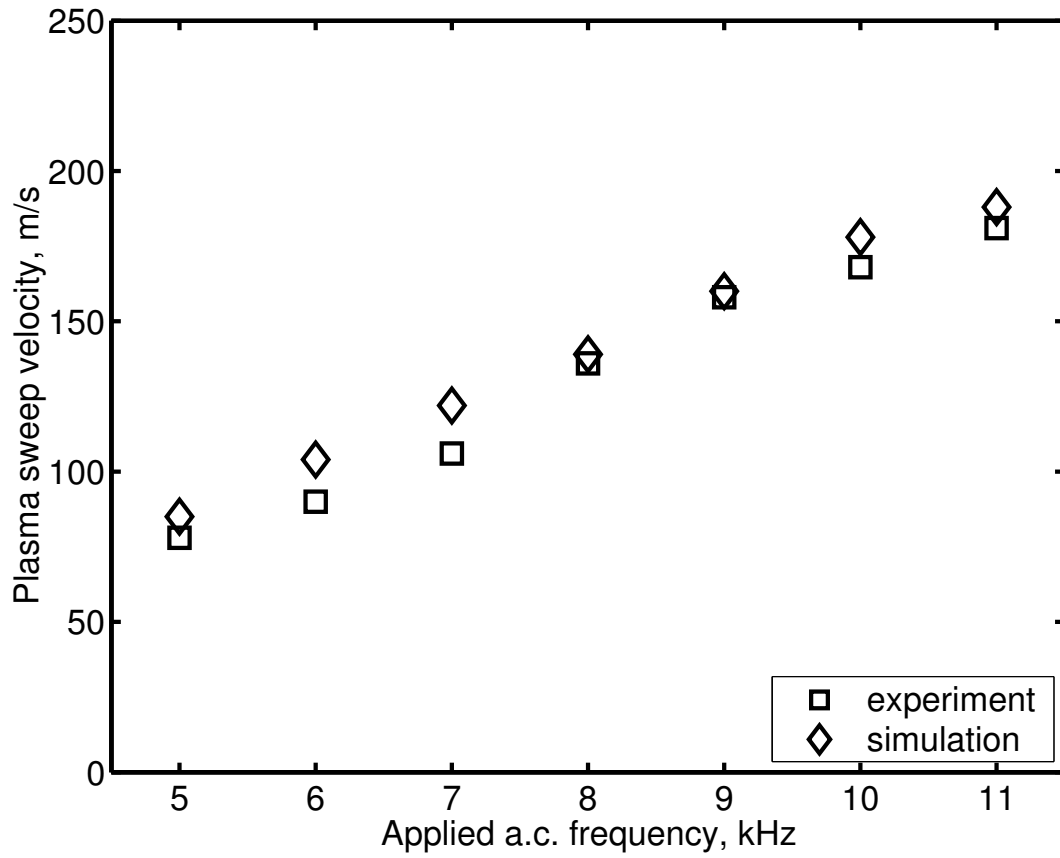


Figure 4.21. Comparison between space-time model and experiment for plasma sweep velocity as function of applied a.c. frequency.

These results are necessary to obtain the plasma body force. The solution for the voltage on the surface of the dielectric serves as the time-dependent boundary condition of the electric potential, φ , in the electrostatic equation (4.30) at the electrodes. The extent of the plasma on the surface of the dielectric specifies the region of the presence of charges above the encapsulated electrode, as shown in Figure 4.22. The value of the electric potential on the exposed electrode are specified to be the applied voltage $V_{app}(t)$. The boundary conditions at the outer boundaries are set to the “infinity” boundary conditions ($\varphi = 0$). With these boundary conditions, the electrostatic equation

$$\nabla(\varepsilon\nabla\varphi) = \frac{1}{\lambda_D^2}\varphi \quad (4.30)$$

is solved as previously described in Chapter 2. This is done at each time step of the lumped-element circuit model to account for the time dependence of the ionization. The solution of the electrostatic equation is then used to calculate the time-dependent body force produced by the plasma, given as before as

$$\vec{f}_b^* = \rho_c\vec{E} = -\left(\frac{\varepsilon_0}{\lambda_D^2}\right)\varphi\vec{E}. \quad (4.31)$$

The procedure for the body force computation then consists of the following steps:

1. Specify initial values for the Lumped-element Circuit Model at time t ;
2. Solve the Lumped-element Circuit Model equations at time t ;
3. Get the values of the voltage on the surface of the dielectric V_n at time t and the extent of the plasma x_p at time t ;

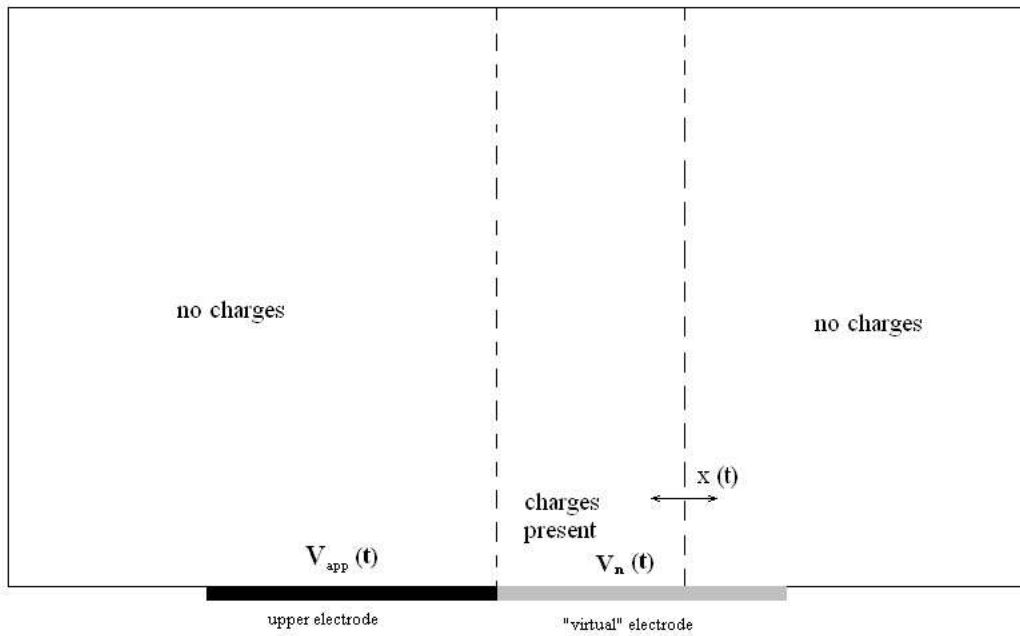


Figure 4.22. Computational domain for calculation of unsteady plasma body force.

4. Set the boundary conditions for the electric potential on the dielectric surface “virtual electrode” equal to the voltage values V_n , and for the electric potential on the upper electrode equal to the applied voltage V_{app} ;
5. Define the region of the charges presence over the surface of the dielectric between the junction of the electrodes and the extent of the plasma x_p ;
6. Solve the electrostatic equation for the electric potential φ as described in Chapter 3;
7. Calculate the plasma body force \vec{f}_b at time t as described in Chapter 3;
8. Increase the time t by δt and return to Step 1.

Following this procedure, an example of the normalized magnitude of the plasma body force for the asymmetric electrode arrangement illustrated in Figure 4.22 is shown in Figure 4.23. This shows the body force distribution in space and time. It can be noticed that the largest magnitude of the plasma body force is near the edge of the exposed electrode. From that location the magnitude decays rapidly over the surface of the dielectric. Recall that experiments indicated that the plasma illumination decreased exponentially. This is consistent with the decay that comes from the solution of the lumped-element circuit model. It justifies the exponential weighting that was used in the electrostatic model described in Chapter 3.

Another feature that can be noticed from Figure 4.23 is that the body force peaks four times during one a.c. cycle. This is clearly seen in Figure 4.24 where the maximum value of the body force near the edge of the electrode is plotted as a function of time for one a.c. period. The fact that the body force has four peaks is resulting from the body force formulation (4.31) and the fact that during the

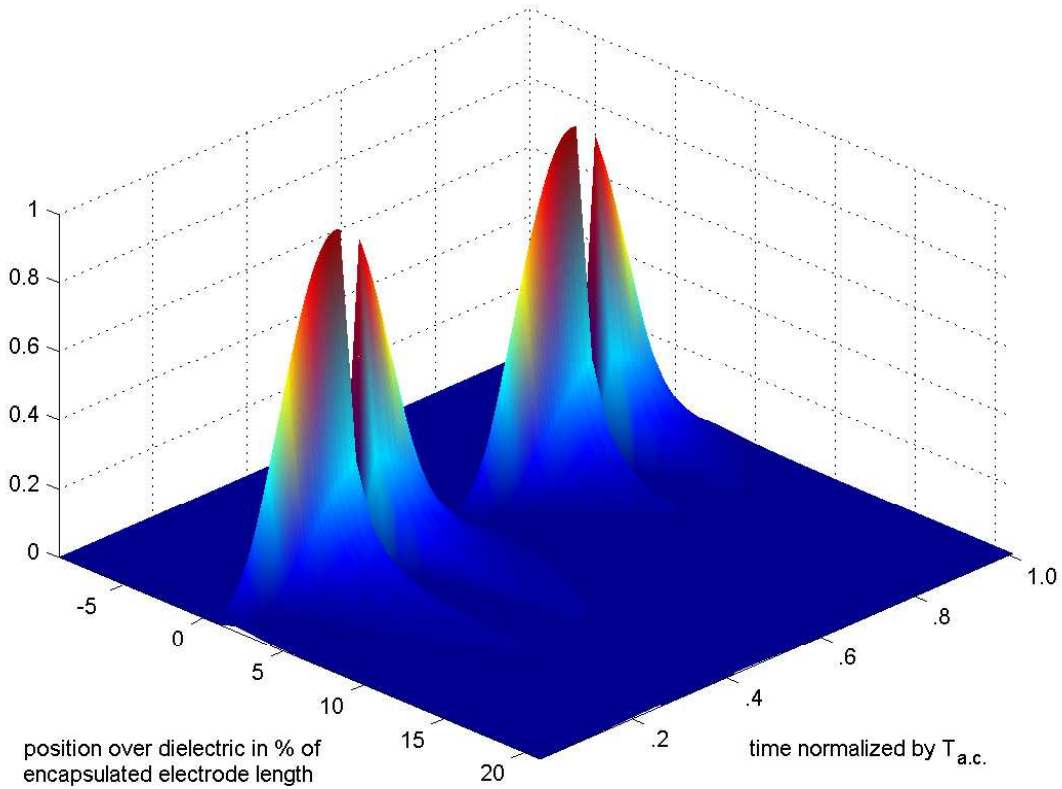


Figure 4.23. Normalized plasma bodyforce magnitude as function of time and position over covered electrode.

a.c. cycle the electric potential, φ , is equal to 0 when $V_{app} = 0$, and the electric field, \vec{E} is equal to 0 when applied voltage reaches its maximum and minimum values.

Another important feature of the plasma body force is the direction of the force vector during the A.C. cycle. To illustrate this, the body force vectors and amplitudes have been plotted at four time locations corresponding to four peaks in the body force. This is shown in Figures 4.25 - 4.28. This illustrates that the actuator force vector is always in one direction, from the exposed electrode towards the covered electrode. Because the body force magnitude peaks four times within

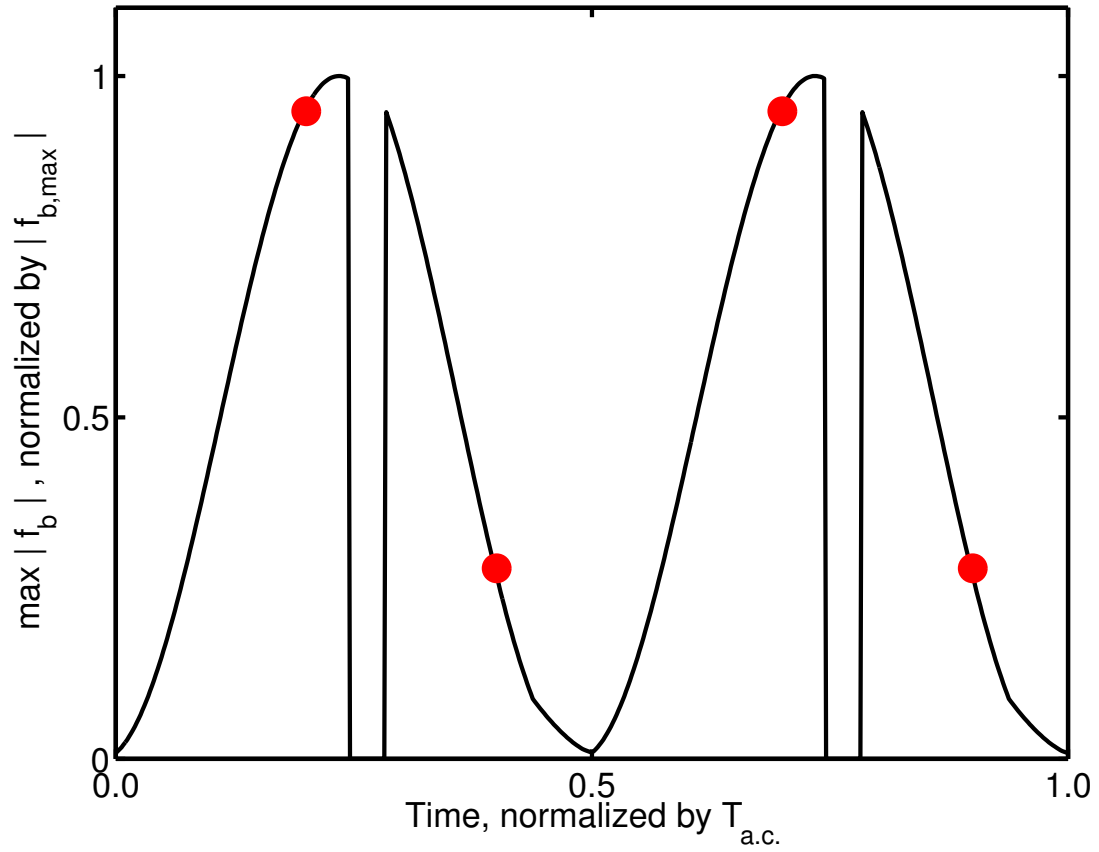


Figure 4.24. Normalized maximum value of the plasma bodyforce magnitude as function of time. Dots indicate where the snapshots of the body force vector fields are taken.

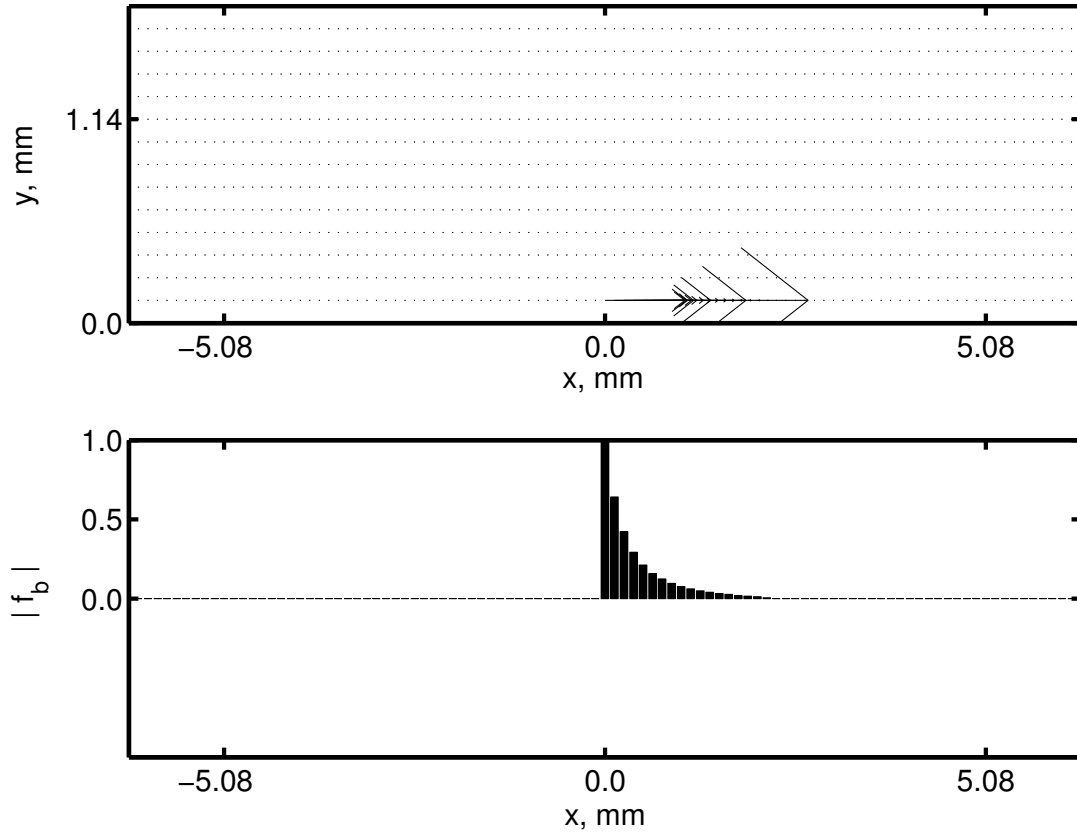


Figure 4.25. Plasma body force vector field and body force amplitude at $t = 0.2 \cdot T_{a.c.}$. The body force is normalized by the maximum value in the a.c. cycle.

the a.c. period and two of the peaks are slightly smaller this might be represented as “Push-push-Push-push” for one a.c. period

These observations suggest that the spectral analysis of the body force may reveal important features of the plasma discharge and also serve as a tool for comparison with the experimental data. For example, the spectrum results can be directly compared to the acoustic or accelerometer measurements of the plasma actuator [57].

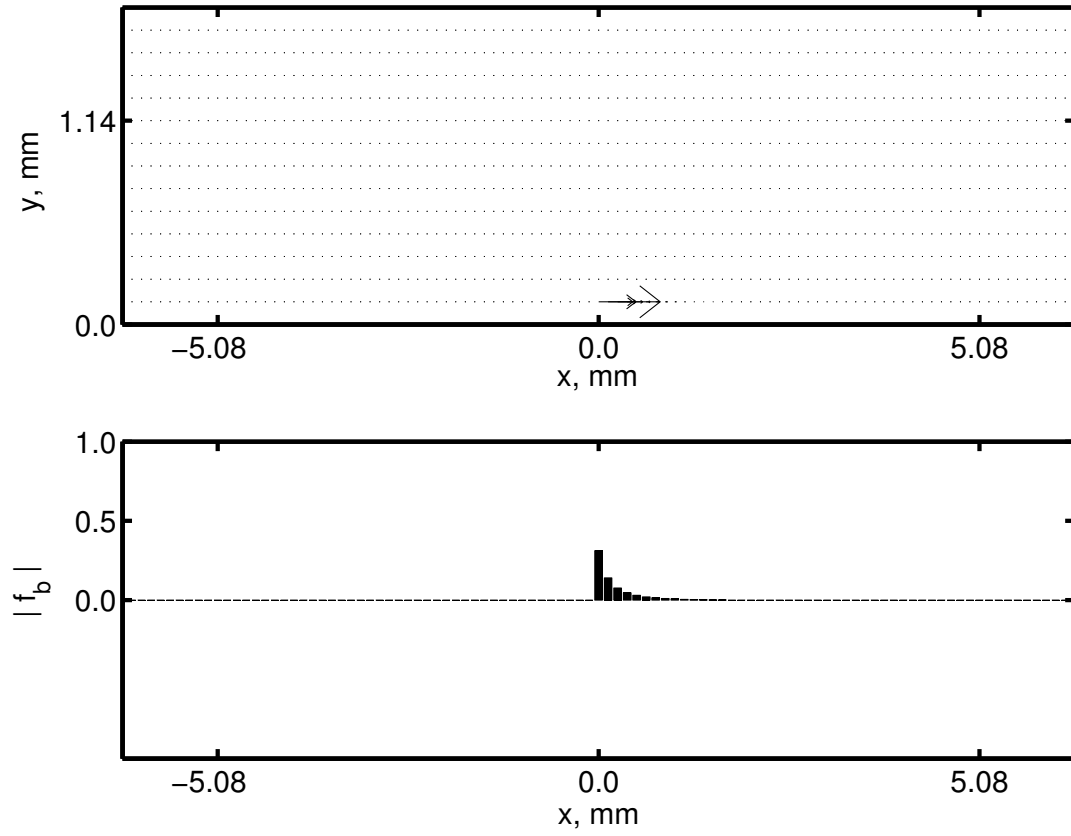


Figure 4.26. Plasma body force vector field at $t = 0.4 \cdot T_{a.c.}$. The body force is normalized by the maximum value in the a.c. cycle.

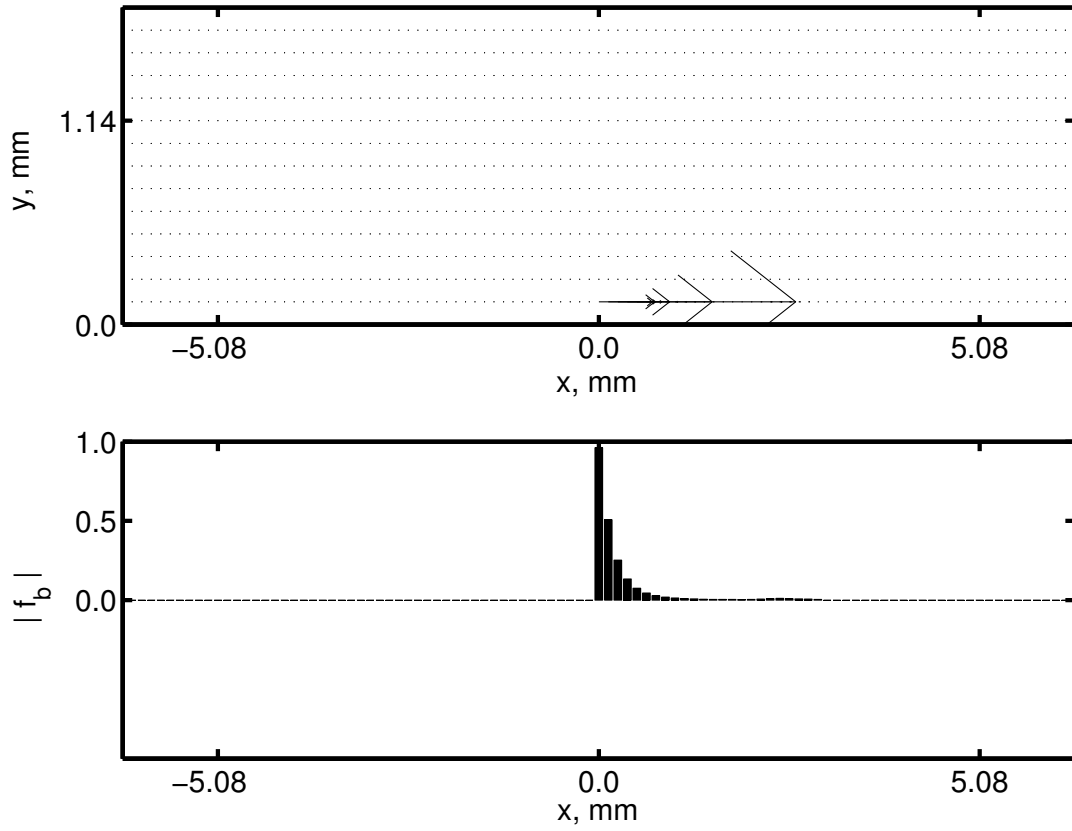


Figure 4.27. Plasma body force vector field at $t = 0.7 \cdot T_{a.c.}$. The body force is normalized by the maximum value in the a.c. cycle.

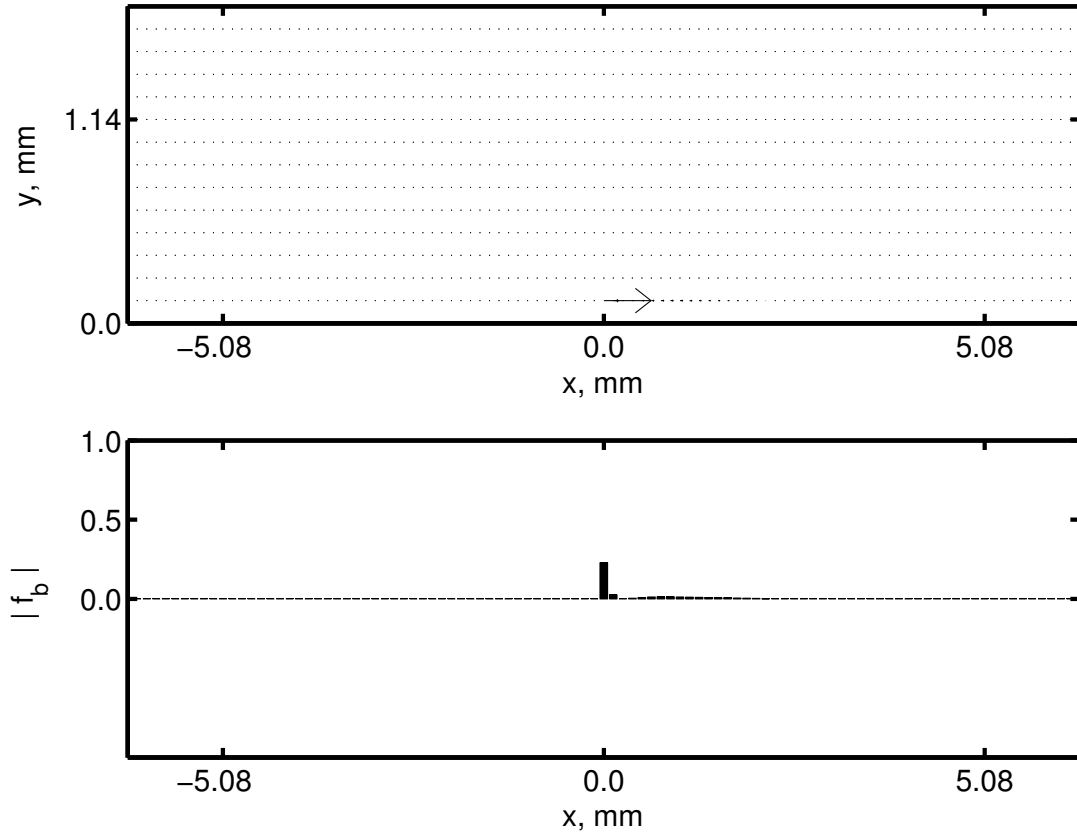


Figure 4.28. Plasma body force vector field at $t = 0.9 \cdot T_{a.c.}$. The body force is normalized by the maximum value in the a.c. cycle.

We performed the spectral analysis of the plasma body force signal shown previously in Figure 4.24. The resulting spectrum is shown in Figure 4.29. It can be noticed that the dominating frequency in this spectrum is twice the frequency of the plasma actuator. This result is consistent with the body force signal shown in Figure 4.24 where the both peaks of the body force are approximately equal. This domination of the second harmonic was also noticed in the experiments by Porter *et al.* [57]. In their experiment, the spectrum of the accelerometer signal showed the dominance of the second harmonic in one of the studied cases (7 kHz), but not in the other two cases (5 and 6 kHz). This difference in their observations may be explained by the transfer to the filamentary regime at lower frequencies when the plasma becomes non-uniform.

Using the space-time lumped-element circuit model we were able to study the effect that different dielectric materials had on the plasma body force. Three different materials were tested with the dielectric coefficients $\varepsilon = 10, 100,$ and 1000 . A set of numerical simulations has been carried out for a range of a.c. frequencies from 1 Hz to 10 kHz. The results of these simulations are presented in Figures 4.30 and 4.31 for the plasma body force and the power dissipated by the actuator.

From the body force results we notice that for each material tested there exists the optimal frequency at which the plasma actuator output is maximum in terms of the force produced. This result is consistent with the general theory of the RC circuits. On the other hand, it has been noticed that the dissipated power increases with the a.c. frequency, and reaches its maximum values at high a.c. frequencies. This suggested that at the higher a.c. frequencies this power does not turn into the body force any more. Instead, it goes into the ohmic heating.

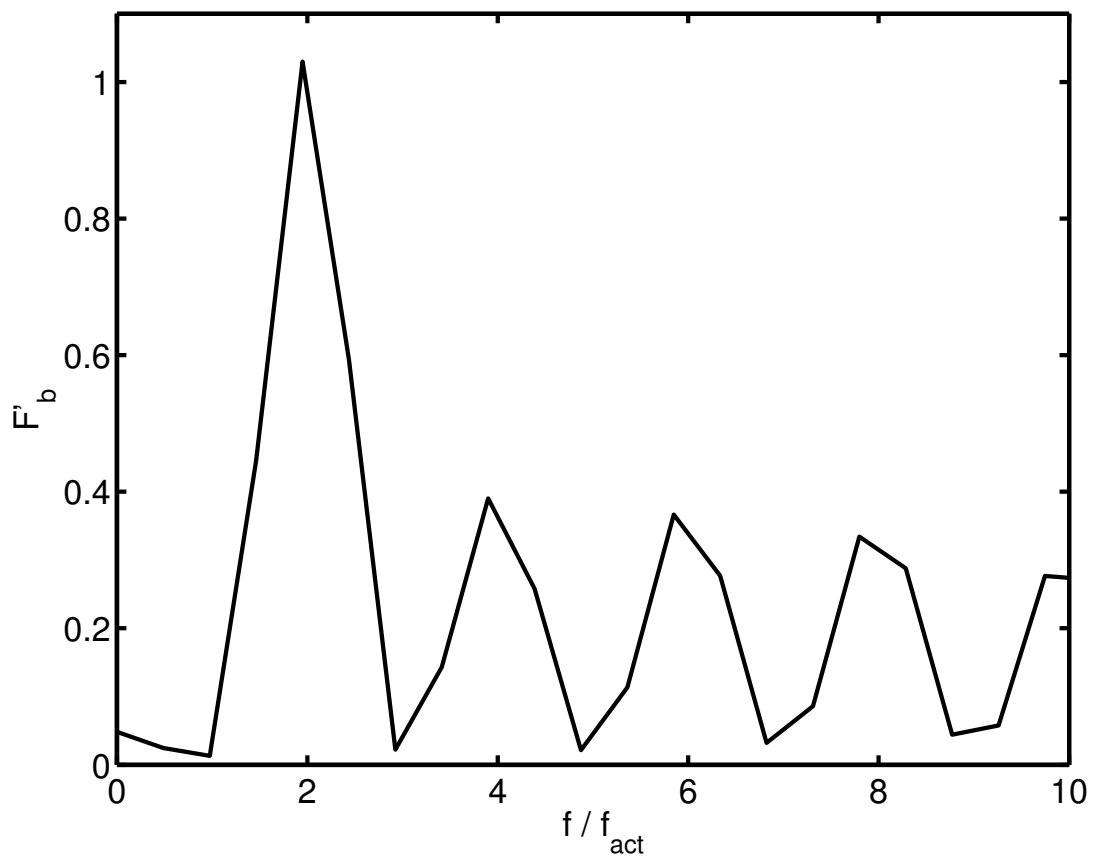


Figure 4.29. Spectrum of the plasma body force obtained with space-time lumped-element circuit model.

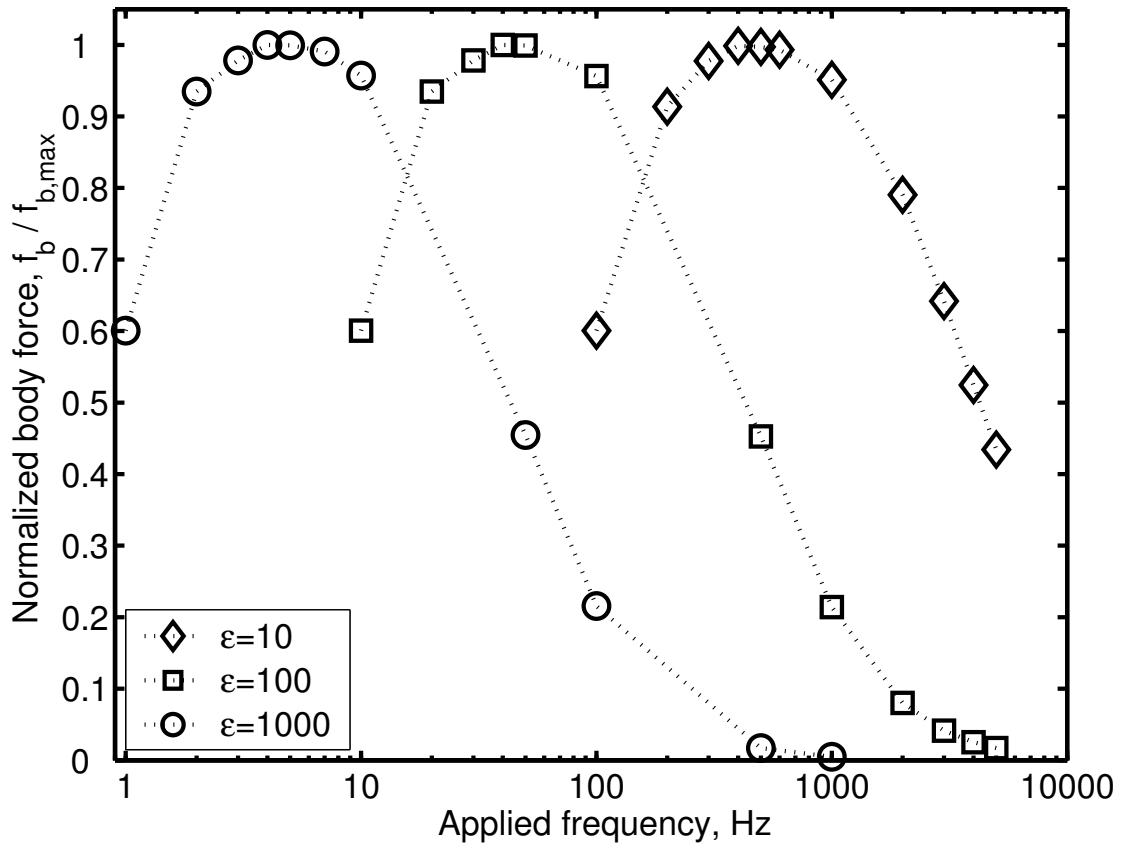


Figure 4.30. Effect of dielectric material on plasma body force.

The other interesting feature that can be noticed here is that the optimum frequency of the plasma actuator depends on the dielectric properties of the material, and decreases with the increasing dielectric coefficient. Our simulations showed that it shifts from the kHz range to the Hz range for ϵ changing from 10 to 1000.

The space-time lumped-element circuit model showed excellent agreement with the experimental results. It allowed us to calculate the time-dependent volume of the plasma over the electrodes during the a.c. cycle. It also provided an efficient

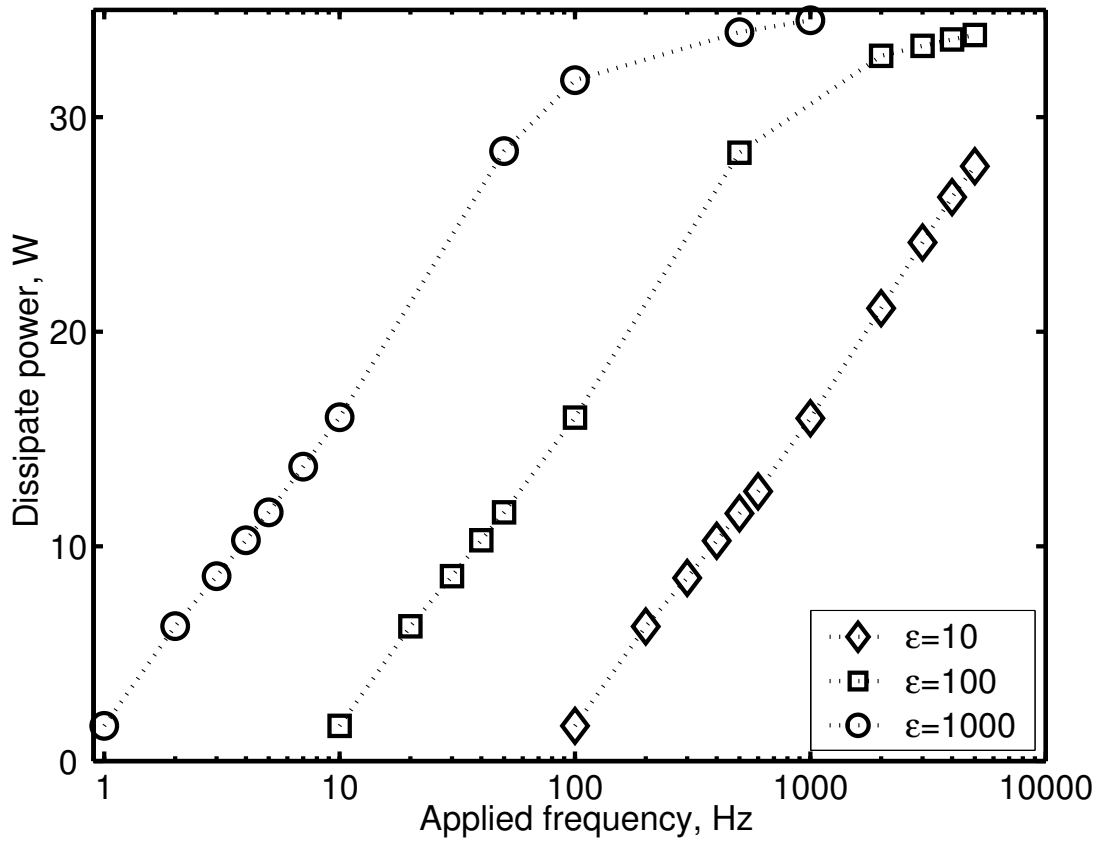


Figure 4.31. Effect of dielectric material on power dissipated by the plasma actuator.

manner for calculating the plasma body force that could be easily incorporated into the Navier-Stokes flow solvers.

CHAPTER 5
MODELING OF LEADING-EDGE SEPARATION CONTROL USING
PLASMA ACTUATORS.

5.1 Background

The maximum lift and stall characteristics of a wing affect many performance aspects of aircraft including take-off and landing distance, maximum and sustained turn rates, climb and glide rates, and flight ceiling [11]. In a 2-D wing, the maximum achievable lift is ultimately limited by the ability of the flow to follow the curvature of the airfoil which affects the pressure gradient. When the pressure gradient becomes too adverse, the flow separates. In many cases at extreme angles of attack, this occurs at the leading edge.

One approach to prevent leading-edge separation is to increase the leading edge radius. This is the principle effect of a leading edge flap. An example is a Krueger flap, which consists of a hinged surface on the lower side of the wing that can extend out and ahead of the wing leading edge. A slotted leading-edge flap (slat) is the leading-edge equivalent of the trailing-edge slotted flap. It works by allowing air from the high-pressure lower surface to flow to the upper surface to add momentum to the boundary layer to overcome an adverse pressure gradient, and prevent flow separation.

Conventional multi-element wings and wings with movable control surfaces such as the leading-edge slats contain gap regions that are a major source of air-

frame noise and unsteady structural loading, especially at high deflection angles. Most of the noise originates from the separated flow in the gap regions. It is also known that the hinge gaps contribute to as much as 10% of the form drag component of the viscous drag on the wing [11]. In order to improve the aerodynamic performance of the wing, it is desirable to either completely replace the traditional moving surfaces with hingeless control surfaces, or limit the deflections of moving surfaces without compromising the wing's performance. Both these alternatives necessitate other approaches for controlling flow separation over the surface of the wing. The following simulation addresses one such approach by using a single-dielectric barrier discharge (SDBD) plasma actuator to control leading-edge flow separation on the wing in a manner that might potentially replace leading-edge slats.

5.2 Problem Formulation

The numerical simulation was performed on a NACA 0021 airfoil with chord length of .3048 m. This was intended to match an experiment on a NACA 0021 airfoil with a plasma actuator on the leading edge. The experiment investigated a range of free-stream speeds from 10 to 30 m/s giving a range of chord Reynolds numbers of $0.205 \cdot 10^6$ to $0.615 \cdot 10^6$. Lift and drag measurements in the experiment were measured using a force balance. Lift and drag coefficients were measured for a range of angles of attack from 0 to 25 degrees. Therefore these experimental results provide a basis for comparison to the numerical simulations.

The first step in the simulations was to compute the body force produced by the actuator at the leading edge. For this the electro-static model described in Chapter 3 of the thesis was used. As pointed out in the discussion of this

model and the motivation of the space-time lumped-element model, the electrostatic model does not include the spatial variation of the charged air over the dielectric-covered electrode. However we can compensate for that effect by adding an experimental decay weighting of the body force as discussed in 3.2.2. The experimental spatial weighting agreed well with experimental observations of the plasma light illumination presented in Figure 3.12, and the space-time simulations presented in Chapter 4, Figure 4.23.

Using the electro-static SDBD actuator model, the body force computations were performed on an unstructured grid using COMSOL Multiphysics (FemLab) [2]. The center line of the actuator was located at the leading edge ($x/C = 0$). A schematic of the actuator arrangement on the airfoil is shown in Figure 5.1. The exposed actuator was located on the pressure side of the airfoil, and the embedded electrode was placed on the suction side. In order to represent the experiment, the electrodes were 1/2 in. wide. The dielectric material was a thick layer of a 3 mil Kapton.

For the simulation, the grid was manually refined near the location of the actuator. The final numerical grid for the body force calculations is shown in Figure 5.2.

The boundary conditions were the same as discussed in the electrostatic model section 3.1.1.1. This was a static electric potential equal to the applied voltage to the electrodes of $5 kV_{p-p}$. The electric potential far from the electrodes at the boundaries of the computational domain was set to zero. As before with body force calculations, the plasma was taken to be only over the dielectric that covers the electrode. The governing equation for the region over the exposed electrode

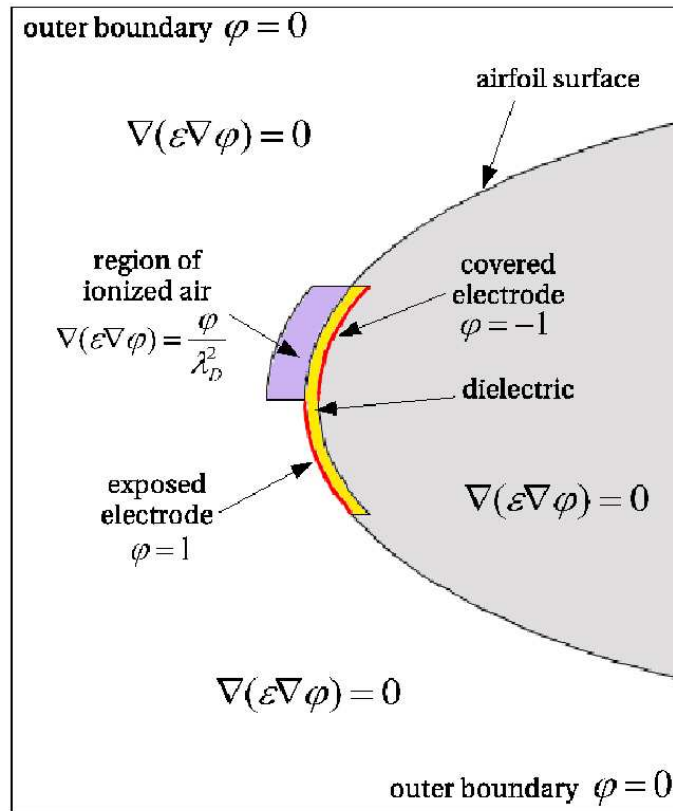


Figure 5.1. Schematic of the plasma actuator on the leading edge of NACA 0021 airfoil for body force computations.

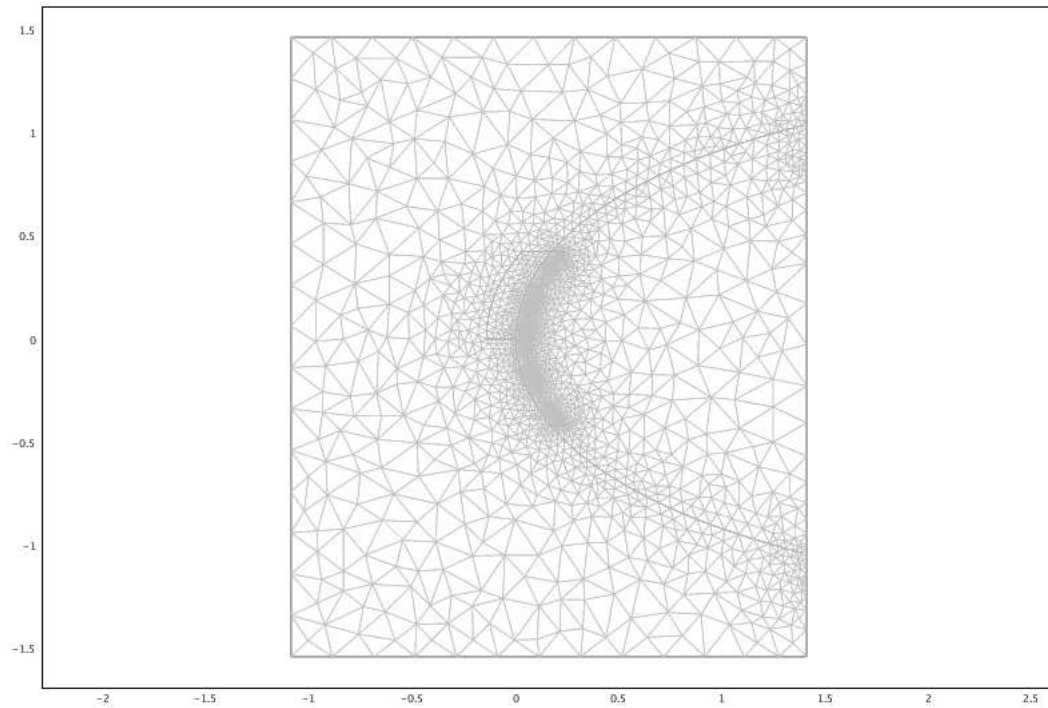


Figure 5.2. Unstructured grid near leading edge of NACA 0021 airfoil for plasma body force computations.

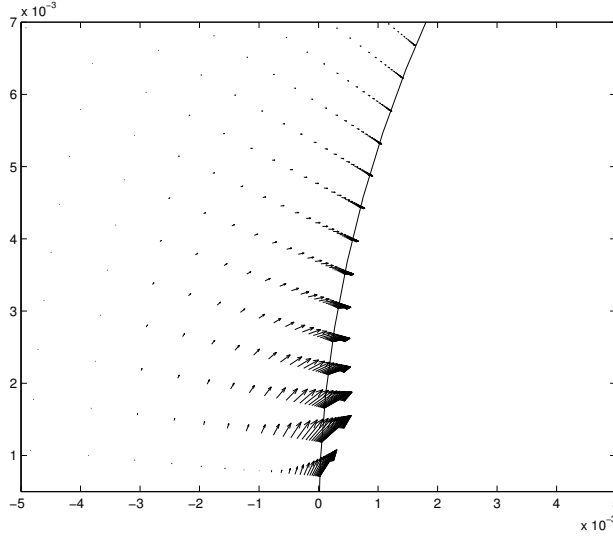


Figure 5.3. Computed steady plasma body force vectors near leading edge of NACA 0021 airfoil, shown on structured computational grid used for flow solver.

was Laplace equation given as

$$\nabla(\varepsilon\nabla\varphi) = 0. \quad (5.1)$$

The governing equation for the region over the covered electrode was Poisson's equation given as

$$\nabla(\varepsilon\nabla\varphi) = \frac{\varphi}{\lambda_d^2}. \quad (5.2)$$

The solution gives the body force magnitude and vector directions. These are shown in Figure 5.3. In this case, the body force values were taken from the unstructured grid and interpolated onto a structured grid used in the solution of the flow field. For this, the experimental spatial weighting (equation (3.65) in section 3.2.1) has been applied.

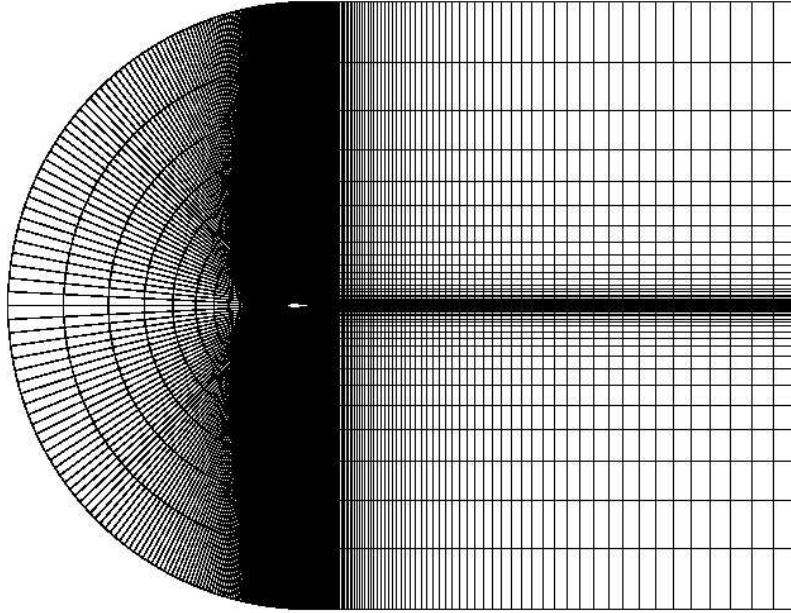


Figure 5.4. Full view of computational grid used for the flow simulation of the NACA 0021 airfoil.

The flow simulation was performed using FLUENT. The structured *C*-type grid was meshed around the airfoil using GAMBIT [4]. The surface of the airfoil was meshed with 400 grid points. There were 100 grid points used in the direction normal to airfoil surface, with a majority of the grid points located in the region of the boundary layer. The inlet boundary was located 10 chord lengths from the airfoil leading edge, and the outflow boundary was located 20 chord lengths downstream the airfoil trailing edge. The full computational grid used in the flow simulations is shown in Figure 5.4. A zoomed-in view near the airfoil is shown in Figure 5.5.

The governing model equations for the flow were 2-D unsteady Reynolds-averaged Navier-Stokes (RANS) equations. Our intention was that the flow be incompressible. In FLUENT, if the density is defined using the ideal gas law for

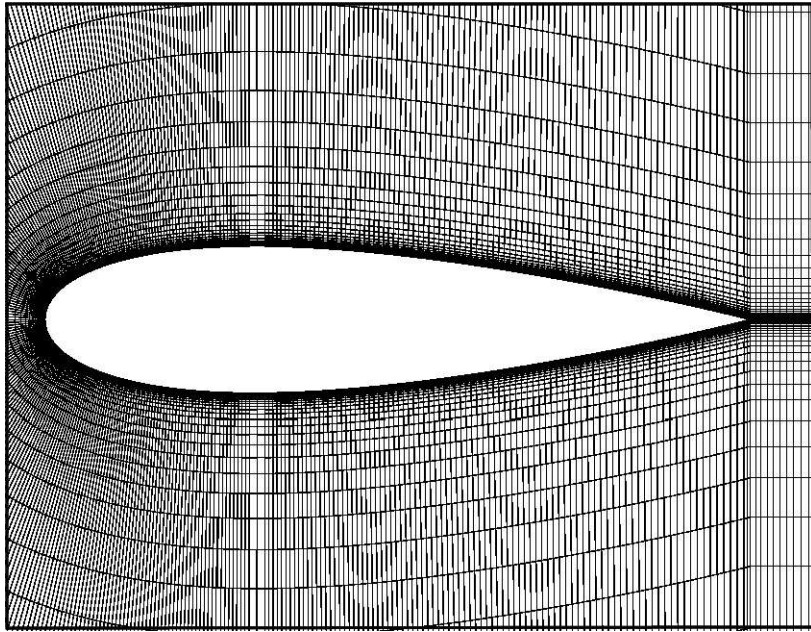


Figure 5.5. Zoomed-in view of computational grid showing grid point clustering in the region of the boundary layer.

an incompressible flow, the solver computes the density as

$$\rho = \frac{p_{\text{op}}}{\frac{R}{M_w} T} \quad (5.3)$$

where, R is the universal gas constant, M_w is the molecular weight of the gas, and p_{op} is the operating pressure. In this form, the density depends only on the operating pressure and not on the local relative pressure field.

FLUENT solves conservation equations for mass and momentum. The equation for conservation of mass has the form

$$\frac{\partial \rho}{\partial t} + \nabla \cdot (\rho \vec{v}) = S_m. \quad (5.4)$$

Conservation of momentum in an inertial (non-accelerating) reference frame is given as [10]

$$\frac{\partial}{\partial t}(\rho \vec{v}) + \nabla \cdot (\rho \vec{v} \vec{v}) = -\nabla p + \nabla \cdot (\bar{\bar{\tau}}) + \rho \vec{g} + \vec{F} \quad (5.5)$$

where p is the static pressure, $\bar{\bar{\tau}}$ is the stress tensor, and $\rho \vec{g}$ and \vec{F} are the gravitational body force and external body forces, respectively. \vec{F} also contains other model-dependent source terms such as user-defined sources. The stress tensor $\bar{\bar{\tau}}$ is given by

$$\bar{\bar{\tau}} = \mu \left[(\nabla \vec{v} + \nabla \vec{v}^T) - \frac{2}{3} \nabla \cdot \vec{v} I \right] \quad (5.6)$$

where μ is the molecular viscosity, I is the unit tensor, $\nabla \vec{v} = \frac{\partial u_i}{\partial x_j}$ and $\nabla \vec{v}^T = \frac{\partial u_j}{\partial x_i}$, and the second term on the right hand side is the effect of volume dilation. The plasma actuator body force is introduced into the momentum equation as the body force vector \vec{F} .

The standard boundary conditions were used. They induced no-slip and no-penetration on the airfoil surface. Pressure far-field conditions are used in FLUENT to model the free-stream condition at infinity. This is where the free-stream Mach number and static conditions were specified. The pressure far-field boundary condition is a non-reflecting boundary condition based on the introduction of Riemann invariants for a one-dimensional flow normal to the boundary. For flow that is subsonic, there are two Riemann invariants, corresponding to incoming and outgoing waves:

$$R_\infty = v_{n_\infty} - \frac{2c_\infty}{\gamma - 1} \quad (5.7)$$

$$R_i = v_{n_i} + \frac{2c_i}{\gamma - 1} \quad (5.8)$$

where v_n is the velocity magnitude normal to the boundary, c is the local speed of sound and γ is the ratio of specific heats (ideal gas). The subscript ∞ refers to conditions being applied at infinity (the boundary conditions), and the subscript i refers to conditions in the interior of the domain (i.e., in the cell adjacent to the boundary face). These two invariants can be added and subtracted to give the following two equations:

$$v_n = \frac{1}{2}(R_i + R_\infty) \quad (5.9)$$

$$c = \frac{\gamma - 1}{4}(R_i - R_\infty) \quad (5.10)$$

where v_n and c become the values of normal velocity and sound speed applied on the boundary.

At a face through which flow exits, the tangential velocity components and entropy are extrapolated from the interior. At an inflow face, these are specified as having free-stream values. Using the values for v_n , c , tangential velocity components, and entropy, the values of density, velocity, temperature, and pressure

at the boundary face can be calculated. For the present simulation, the inflow was set at 35 m/s (corresponding to $M = 0.1$). The angle of attack was varied by changing the angle of the flow at the inflow boundary. The turbulence parameters were defined at the far-field boundary in terms of the turbulence intensity and turbulence viscosity ratio. The turbulence intensity of the inflow was set to 0.1%. This value corresponds to the maximum value of the turbulence intensity in the experiments. The turbulence viscosity ratio was set to be 10. This value was suggested in FLUENT documentation for outer flows.

An additional equation for energy conservation was included in formulation. FLUENT solves the energy equation in the following form:

$$\frac{\partial}{\partial t}(\rho E) + \nabla \cdot (\vec{v}(\rho E + p)) = \nabla \cdot \left(k_{\text{eff}} \nabla T - \sum_j h_j \vec{J}_j + (\vec{\tau}_{\text{eff}} \cdot \vec{v}) \right) + S_h \quad (5.11)$$

where k_{eff} is the effective conductivity equal to $k + k_t$, where k_t is the turbulent thermal conductivity, defined according to the v^2 - f turbulence model, and \vec{J}_j is the diffusion flux of species j . The first three terms on the right-hand side of Equation 5.11 represent energy transfer due to conduction, species diffusion, and viscous dissipation, respectively. S_h includes the heat of chemical reaction, and any other volumetric heat sources defined. In Equation 5.11,

$$E = h - \frac{p}{\rho} + \frac{v^2}{2} \quad (5.12)$$

where sensible enthalpy h is defined for ideal gases as

$$h = \sum_j Y_j h_j, \quad (5.13)$$

where Y_j is the mass fraction of species j and

$$h_j = \int_{T_{\text{ref}}}^T c_{p,j} dT \quad (5.14)$$

and T_{ref} is 298.15 K.

A second order implicit formulation was used for time and space discretizations. The SIMPLE algorithm was used for the pressure-velocity coupling. This algorithm uses a relationship between velocity and pressure corrections to enforce mass conservation and to obtain the pressure field. In the SIMPLE algorithm, an approximation of the velocity field is obtained by solving the momentum equations. The pressure gradient term is calculated using the pressure distribution from the previous iteration or an initial guess. The pressure equation is formulated and solved in order to obtain the new pressure distribution. From this the velocities are corrected and a new set of conservative fluxes are calculated. A more detailed description of the SIMPLE algorithm may be found in the Fluent documentation files [3].

The first simulation was performed at 0 degrees angle of attack. The flow was initialized from the inflow boundary. Afterwards, the solution at higher angles of attack used the previous converged solution at one degree smaller as the initial condition for the simulation.

The identification of vortical structures has been performed using the $-\lambda_2$ technique developed by Hussain [36]. In this technique, the eigenvalues of the symmetric tensor $S^2 + \Omega^2$ are considered: here S and Ω are the symmetric and antisymmetric parts of the velocity gradient tensor ∇u . The vortex region is identified by the negative values of the second eigenvalue, λ_2 .

In planar flow, the velocity gradient can be written in general form as

$$\nabla u = \begin{pmatrix} a & b \\ c & -a \end{pmatrix}, \quad (5.15)$$

where $a = u_x$, $b = u_y$ and $c = v_x$. Therefore, we get that the $S^2 + \Omega^2$ matrix in this case would be given as

$$\nabla u = \begin{pmatrix} a^2 + bc & 0 \\ 0 & a^2 + bc \end{pmatrix}, \quad (5.16)$$

and the characteristic equation can be written as

$$(a^2 + bc - \lambda)(a^2 + bc - \lambda) = 0. \quad (5.17)$$

This equation has the solution

$$\lambda_{1,2} = a^2 + bc. \quad (5.18)$$

Thus, negative λ_2 requires that

$$u_x^2 + u_y v_x < 0. \quad (5.19)$$

5.3 Results

During the first phase of the simulations, the base flow without flow control was modeled. The behavior of the lift and drag coefficients was taken to be the convergence criteria for the flow problem. The lift and drag coefficients conver-

gence time series are shown in Figure 5.6 for the low angle of attack (5 degrees) and in Figure 5.7 for high angle of attack when the airfoil is completely stalled (25 degrees).

As the simulations showed, at lower angles of attack, below approximately 12 degrees, the linear airfoil theory holds and the slope, $\frac{dC_L}{d\alpha} = 2\pi$. Therefore at least in this region the solution is known. In addition, the experimental results for this airfoil gave an indication of the stall angle of attack.

The $v^2 - f$ turbulence model was used in these simulations. This model has been shown to predict the boundary layer separation correctly [16]. Our calculations performed with the $v^2 - f$ turbulence model showed decrease in lift and increase in drag at 18 degrees. This agreed best with the experiment. Based on these tests, the $v^2 - f$ turbulence model was used for all of other calculations with and without the plasma actuators.

The v^2-f model [16] is quite similar to the standard $k-\epsilon$ model, but incorporates near-wall turbulence anisotropy and non-local pressure-strain effects. The v^2-f model is a turbulence model that is valid all the way up to solid walls, and therefore does not need to make use of wall functions. Although the model was originally developed for attached or mildly separated boundary layers, it also accurately simulates flows dominated by separation. The distinguishing feature of the v^2-f model is its use of the velocity scale, $\overline{v^2}$, instead of the turbulent kinetic energy, k , for evaluating the eddy viscosity. The $\overline{v^2}$ can be thought of as the velocity fluctuation normal to the streamlines. It has been shown to provide the right scaling in representing the damping of turbulent transport close to the wall, a feature that k does not provide.

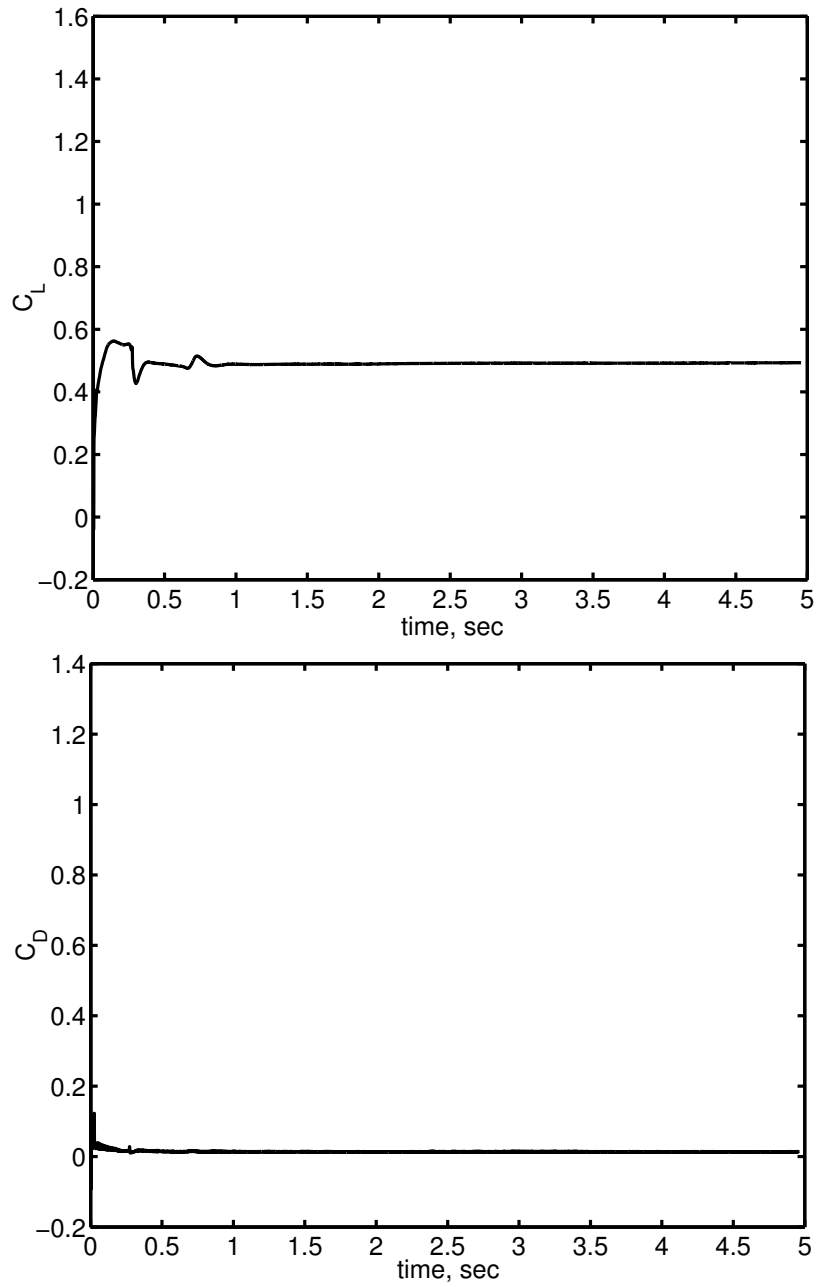


Figure 5.6. Lift and drag coefficients convergence history at 5 degrees angle of attack, $U_{fs} = 35$ m/s, uncontrolled flow.

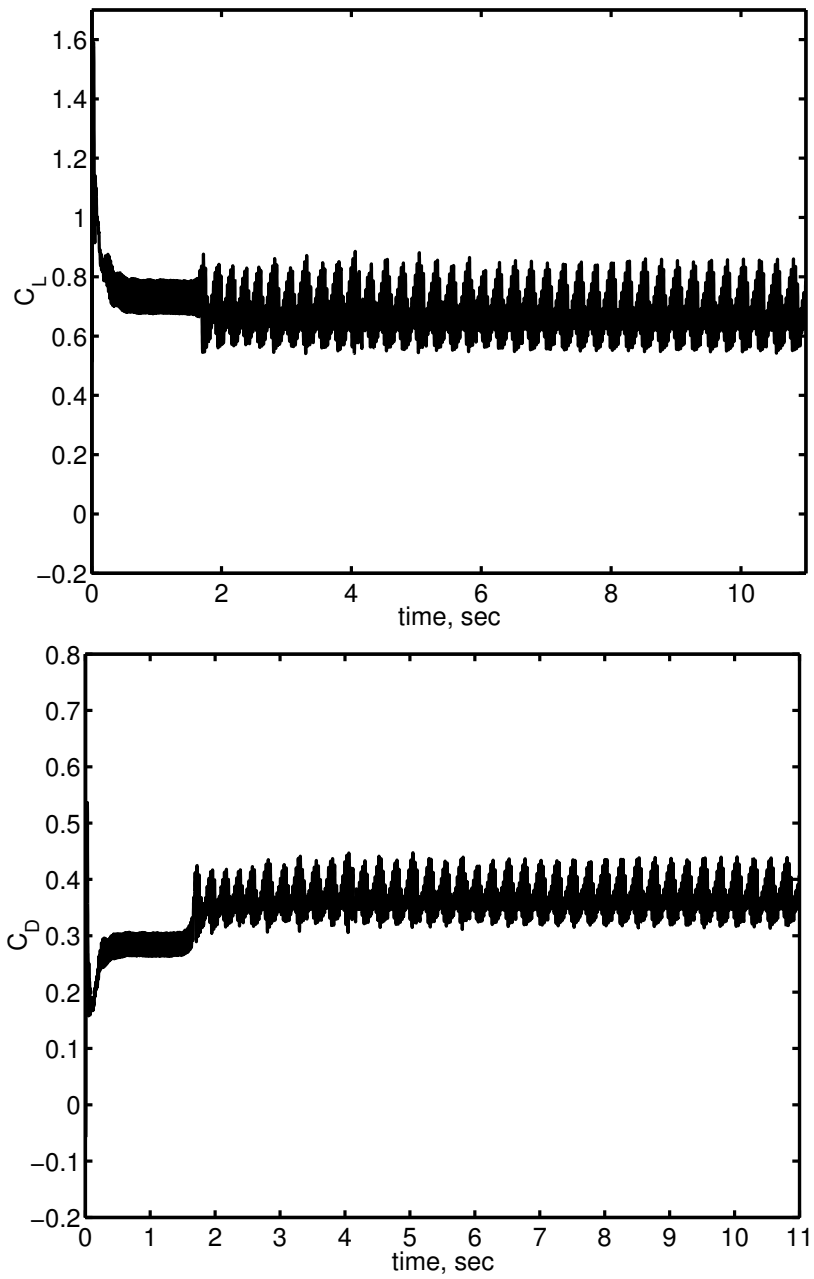


Figure 5.7. Lift and drag coefficients convergence history at 25 degrees angle of attack, $U_{fs} = 35$ m/s, uncontrolled flow.

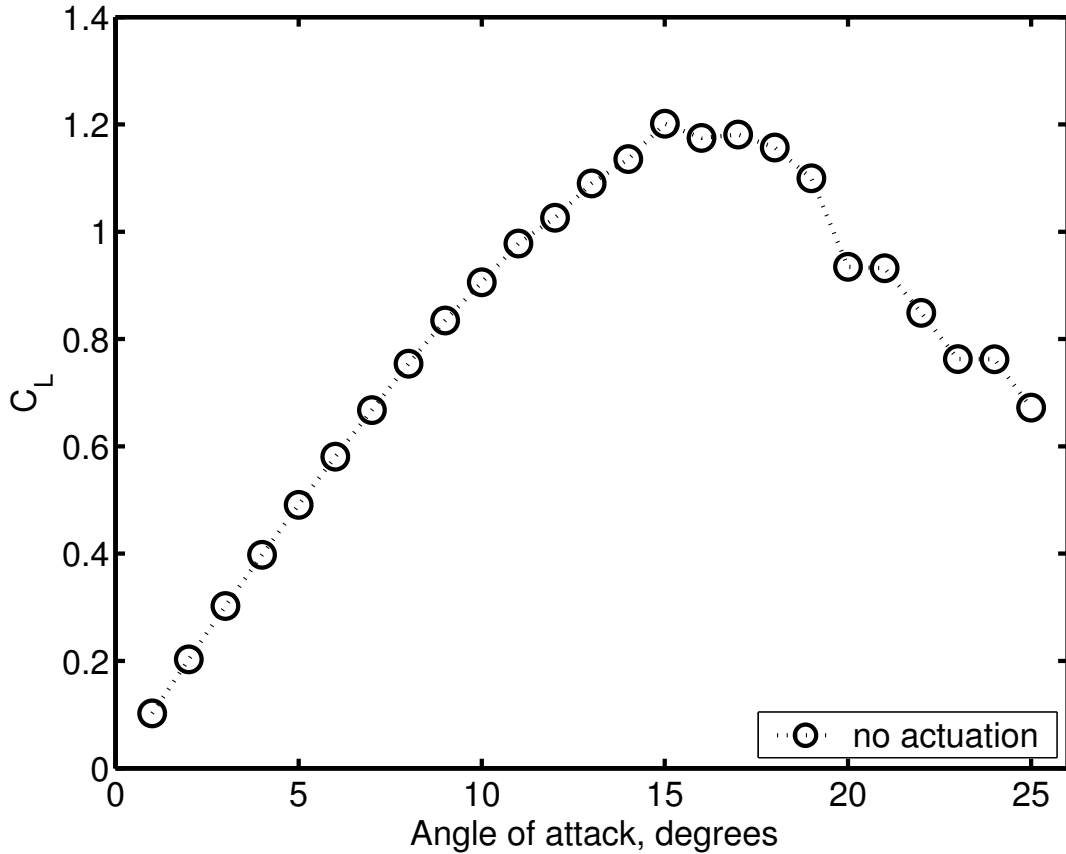


Figure 5.8. Lift coefficient versus angle of attack at $U_{fs} = 35$ m/s for uncontrolled flow.

Figure 5.8 documents the baseline computations for the NACA 0021 airfoil. This shows the expected lift coefficient slope of $0.11 \text{ degrees}^{-1}$. The maximum lift coefficient for this airfoil is approximately 1.2. The airfoil stalls at approximately 18° angle of attack. This simulation is reasonably close to this value, although the drop-off in lift is not as sharp as in the experiment.

For the second part of the simulation, a steady actuator effect was included in the governing equations. As described earlier, the plasma actuator was located at the leading edge of the airfoil. With FemLab, the plasma body force was

introduced using the User-Defined Function Module. For the steady actuator, the body force was constant in time. That is its magnitude was the same at each time step of the calculations.

The third part of the simulation dealt with “unsteady” plasma actuation. The previous experimental work [12] has indicated that better flow re-attachment would occur by operating the actuator at a periodic frequency. The optimum frequency was found in experiments to correspond to $F^+ = fc/U_{fs} = 1$. An example of the unsteady operation used in the experiment is shown in Figure 5.9. This switches on and off the a.c. carrier that ionizes the air in the experiments at a prescribed frequency and duty cycle. The experiments found that a 10% duty cycle was effective.

In the simulations, the body force was represented in the discrete computational time steps of the time dependent formulation. For example, if 100 time steps represented the full period of the actuator at $F^+ = 1$, for a 10% duty cycle, the body force would be non-zero for 10 time steps, and zero for the other 90 time steps. This was implemented using the User Defined Function Module just like with the steady actuator effect.

A sample test case was performed in the still air ($U_{fs} = 0$ m/s) to illustrate the effect of the plasma actuator presence on the airfoil surface. For this the actuator was impulsively switched on, and maintained for a long time period. Velocity vectors recorded a short time after the actuator was started are shown in Figure 5.10. Note that this is similar to the simulations that were done on a flat surface in Figures 3.16 and 3.17 of Section 3.2.2. As in the previous example, the impulsively started actuator produced a local wall jetting effect and a “starting” vortex that is turning counterclockwise. Figures 5.11 - 5.13 shows the vector field 0.02, 0.06

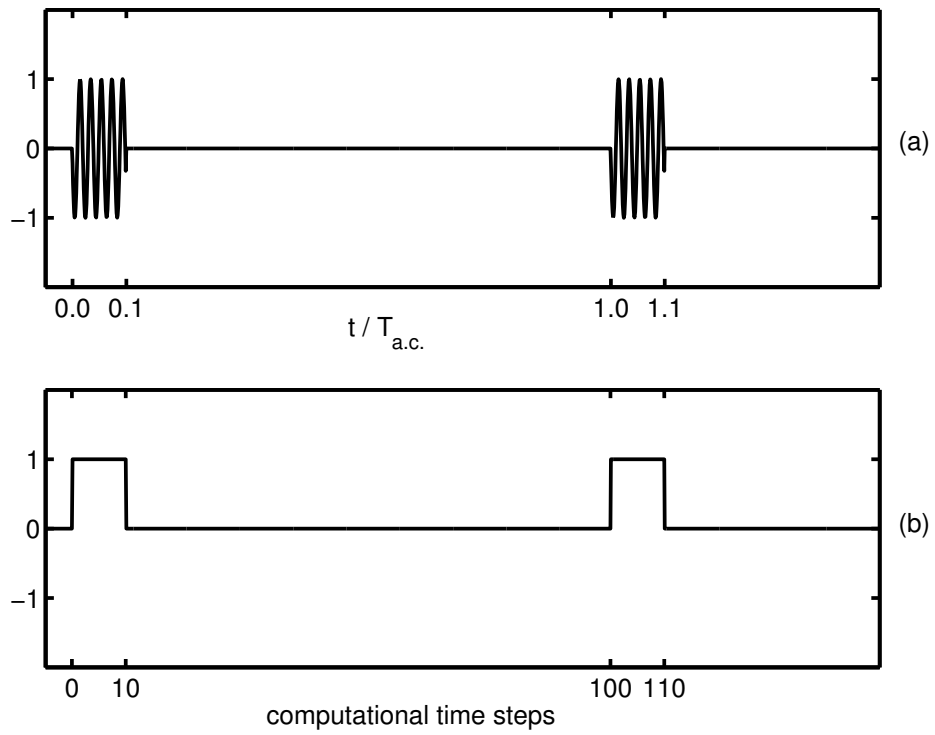


Figure 5.9. Example of short duty cycle a.c. input for unsteady operation of plasma actuators (a) and its numerical representation (b).

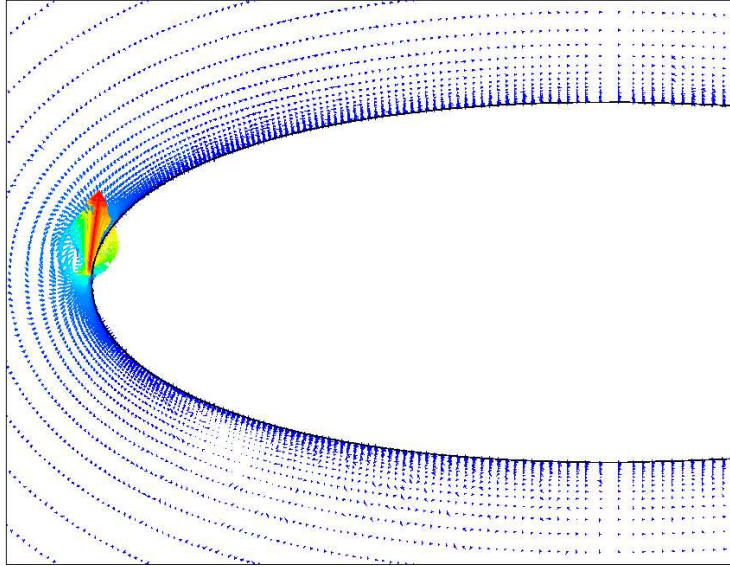


Figure 5.10. Velocity vector field near leading edge of airfoil at $t = 0.00001$ seconds after the impulsive start of the actuator. The largest velocity vector corresponds to $|V| = 4.03$ m/s.

and 0.18 seconds later, respectively. This shows the flow sweeping over the leading edge of the airfoil. There is still a counter-clockwise circulation associated with the impulsive start of the actuator. The wall jet magnitude in this simulation reached a maximum value of 8.37 m/s.

An example of the effect of the plasma actuator on the flow over the airfoil at a post-stall angle of attack of 23 degrees is considered. The flow over the airfoil without any actuation is shown in Figure 5.15. This shows a large separation bubble that starts from the leading edge and extends past the trailing edge. The streamlines show a large circulation indicating flow reversal over the airfoil and into the wake. This is supported by the $\lambda_2 = 0$ contours which show the large separation structure. The streamlines look very much like the streamline pho-

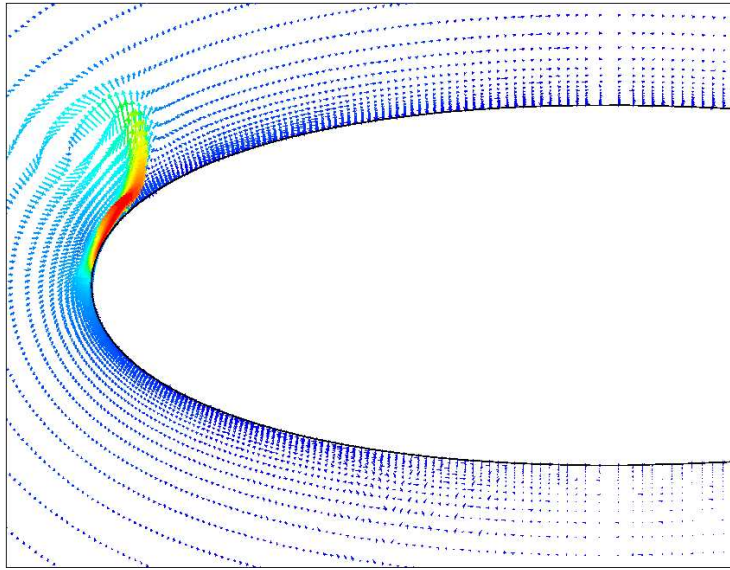


Figure 5.11. Velocity vector field near leading edge of airfoil at $t = 0.02$ seconds after the impulsive start of the actuator. The largest velocity vector corresponds to $|V| = 8.34$ m/s.

tographs of similar airfoils at post-stall angles of attack such as those by Post [61].

In contrast to the case with the actuator off, Figure 5.16 shows streamlines for the same angle of attack (23 degrees) with a steady plasma actuator on. This shows that the flow is attached at the leading edge, leaving only a smaller trailing edge separation. Visually, the wake of the airfoil is significantly smaller, which will translate into lower overall drag.

In case of the unsteady flow actuation, the flow is still attached at the leading edge of the airfoil as it is shown in Figure 5.17. The point where the boundary layer separates from the airfoil surface is approximately at the same location as in the steady actuation case. But the separation bubble appears to be shorter

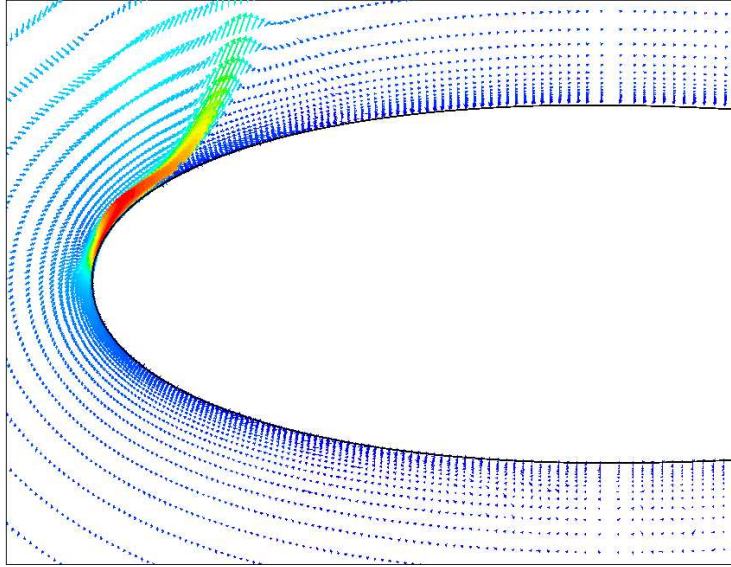


Figure 5.12. Velocity vector field near leading edge of airfoil at $t = 0.06$ seconds after the impulsive start of the actuator. The largest velocity vector corresponds to $|V| = 8.36$ m/s.

than the one during the steady actuation. This agrees well with the experimental observations [52].

A series of simulations at a range of angles of attack with steady and unsteady plasma actuators were conducted. The results of these are summarized in terms of the lift coefficient versus angle of attack and lift-drag polars. These are shown in Figures 5.18 and 5.19. The drag polar and the lift-to-drag ratio are shown in Figures 5.20 and 5.21. In general both the steady and unsteady plasma actuators significantly increased the stall angle of attack.

The experimental results obtained at a slightly lower free stream speed of 30 m/s are presented in Figure 5.22. Overall, they are showing the same trend. The unsteady actuation at the optimal frequency of $F^+ = 1$ delays the airfoil stall

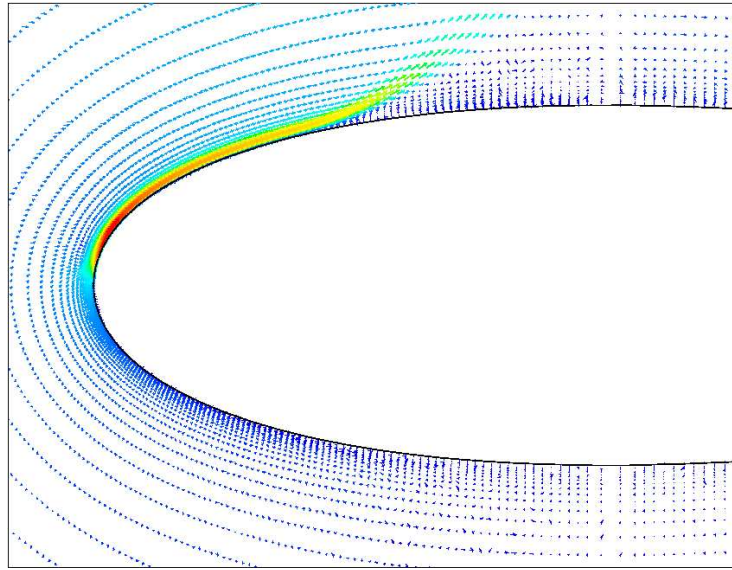
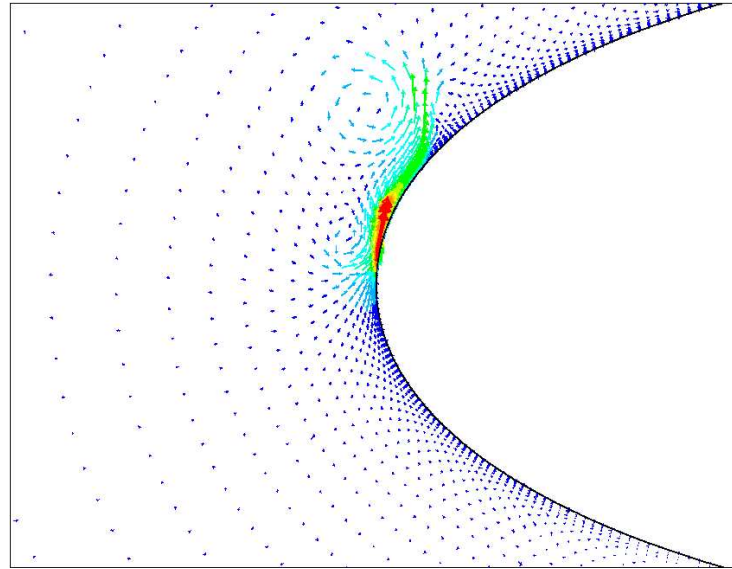


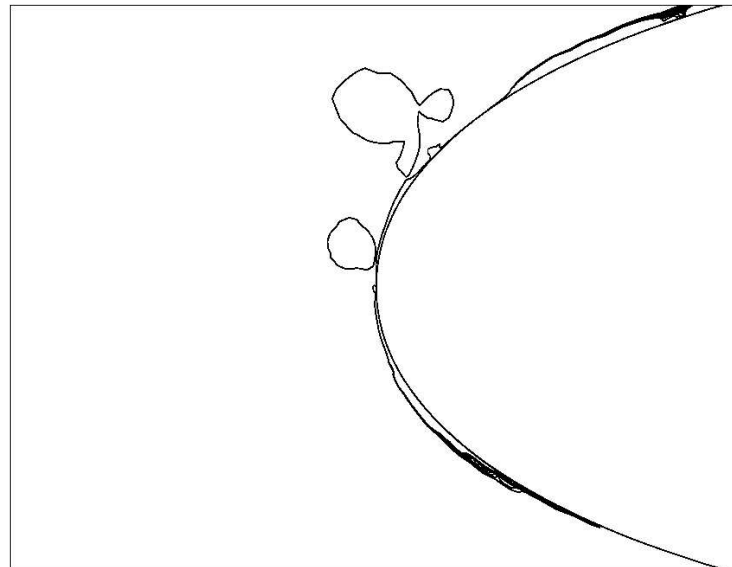
Figure 5.13. Velocity vector field near leading edge of airfoil at $t = 0.18$ seconds after the impulsive start of the actuator. The largest velocity vector corresponds to $|V| = 8.37$ m/s.

angle by 5 degrees, this significantly improves the airfoil characteristics at high angles of attack.

The results of this simulation show good agreement with the experiments. The plasma actuator placed near the leading edge of the airfoil delay the separation and increases the stall angle of attack. The unsteady flow actuation shows even better results than the steady actuation improving the airfoil characteristics at high angles of attack.

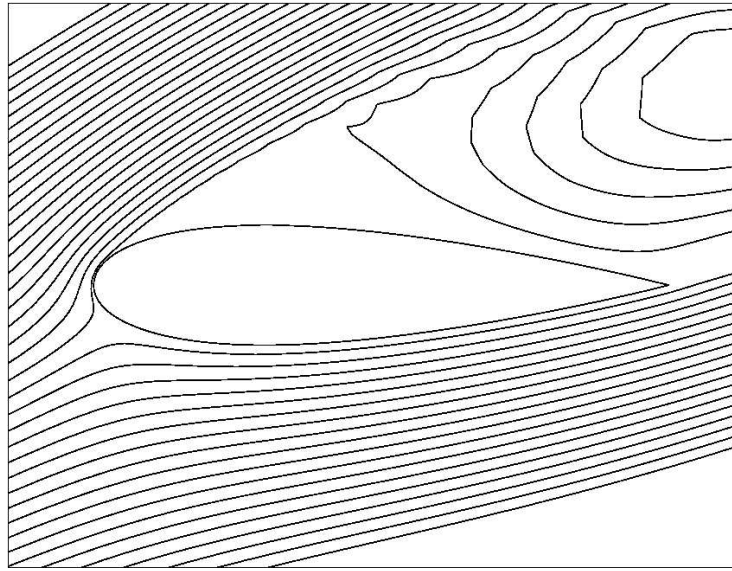


(a)

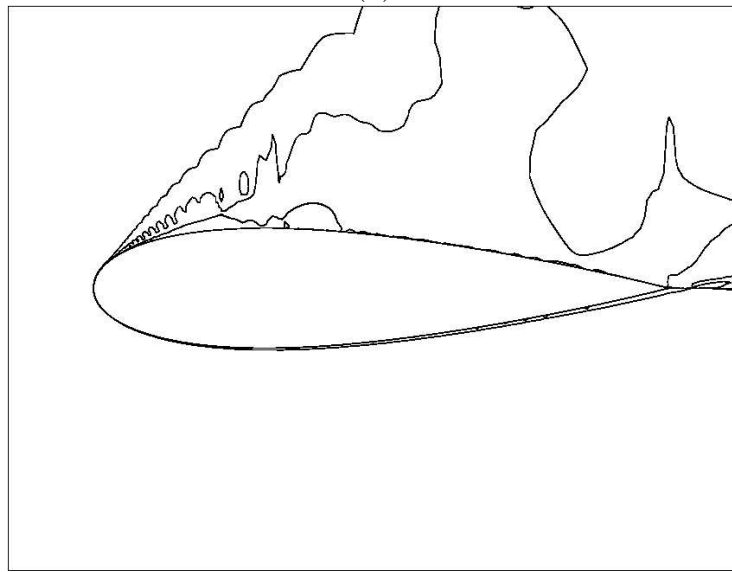


(b)

Figure 5.14. Velocity vector field (a) and contour lines of $\lambda_2 = 0$ (b) at $t = 0.01743$ seconds in still air. The plasma actuator is working in unsteady mode at 120 Hz. The largest velocity vector corresponds to $|V| = 4.49$ m/s.

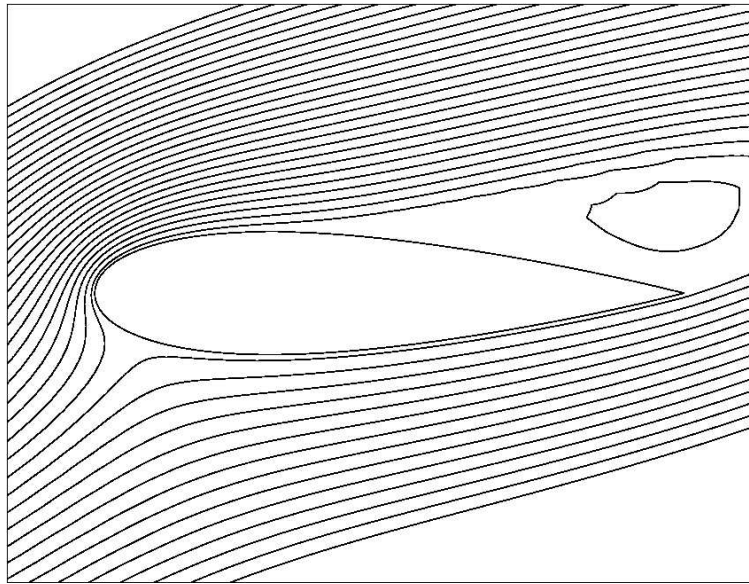


(a)

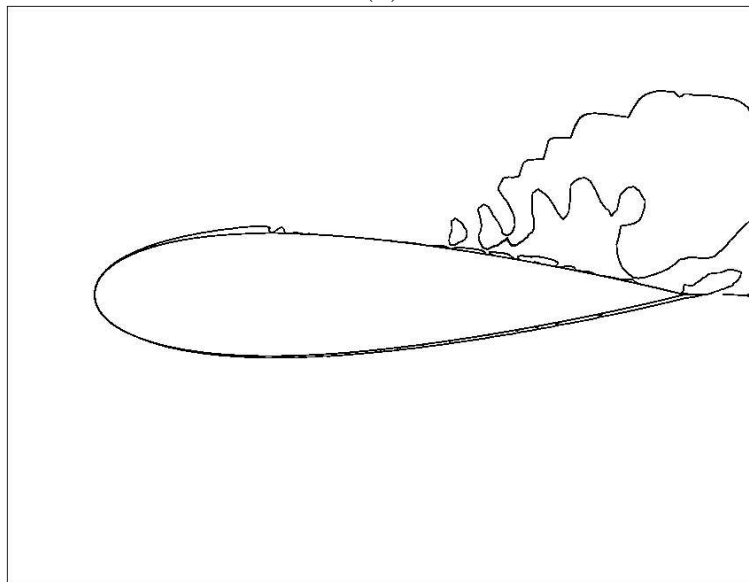


(b)

Figure 5.15. Contour lines of stream function (a) and $\lambda_2 = 0$ (b), no actuation, 23 degrees angle of attack.

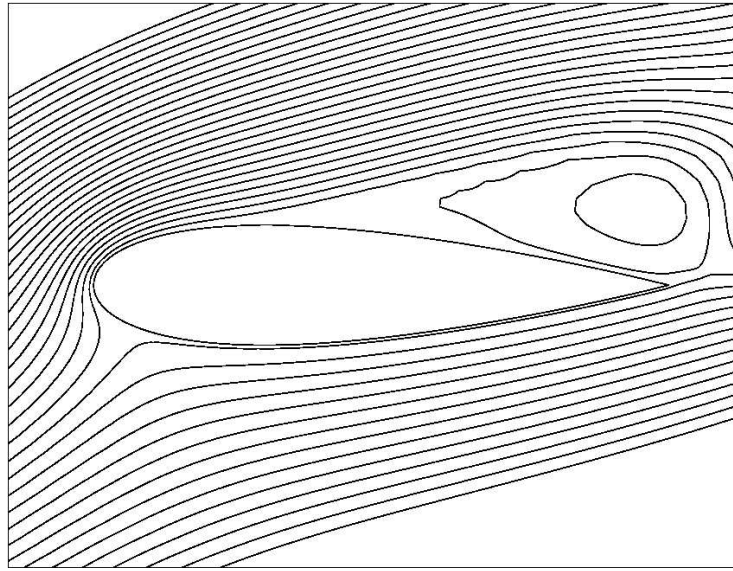


(a)

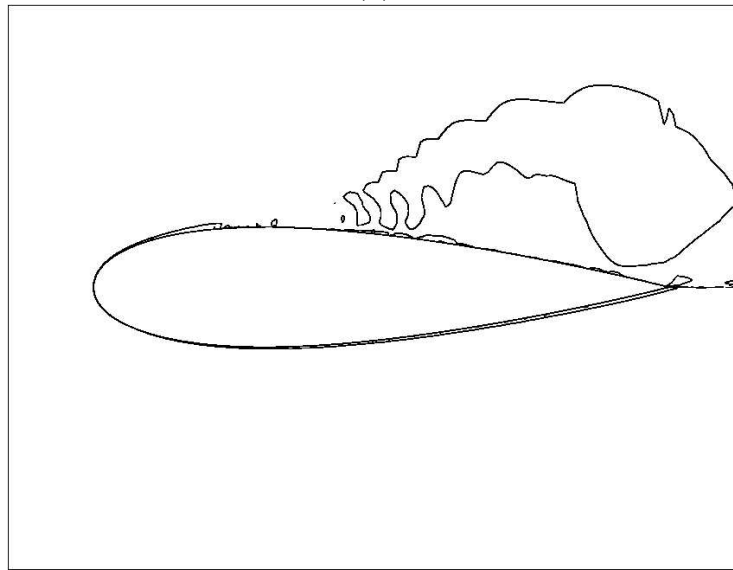


(b)

Figure 5.16. Contour lines of stream function (a) and $\lambda_2 = 0$ (b) for steady actuation, 23 degrees angle of attack.



(a)



(b)

Figure 5.17. Contour lines of stream function (a) and $\lambda_2 = 0$ (b) for unsteady actuation at 120 Hz, duty cycle of 10%, 23 degrees angle of attack.

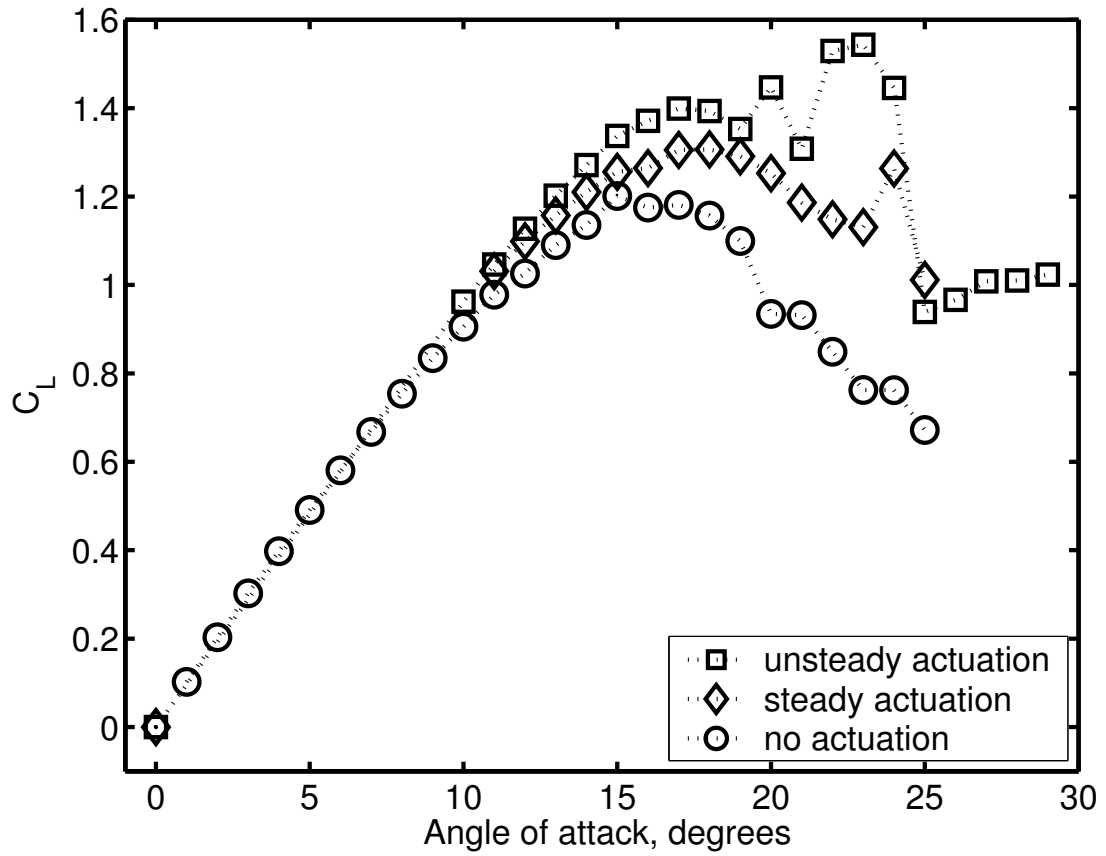


Figure 5.18. Lift coefficient versus angle of attack at $U_{fs} = 35$ m/s for uncontrolled flow, steady and unsteady actuation.

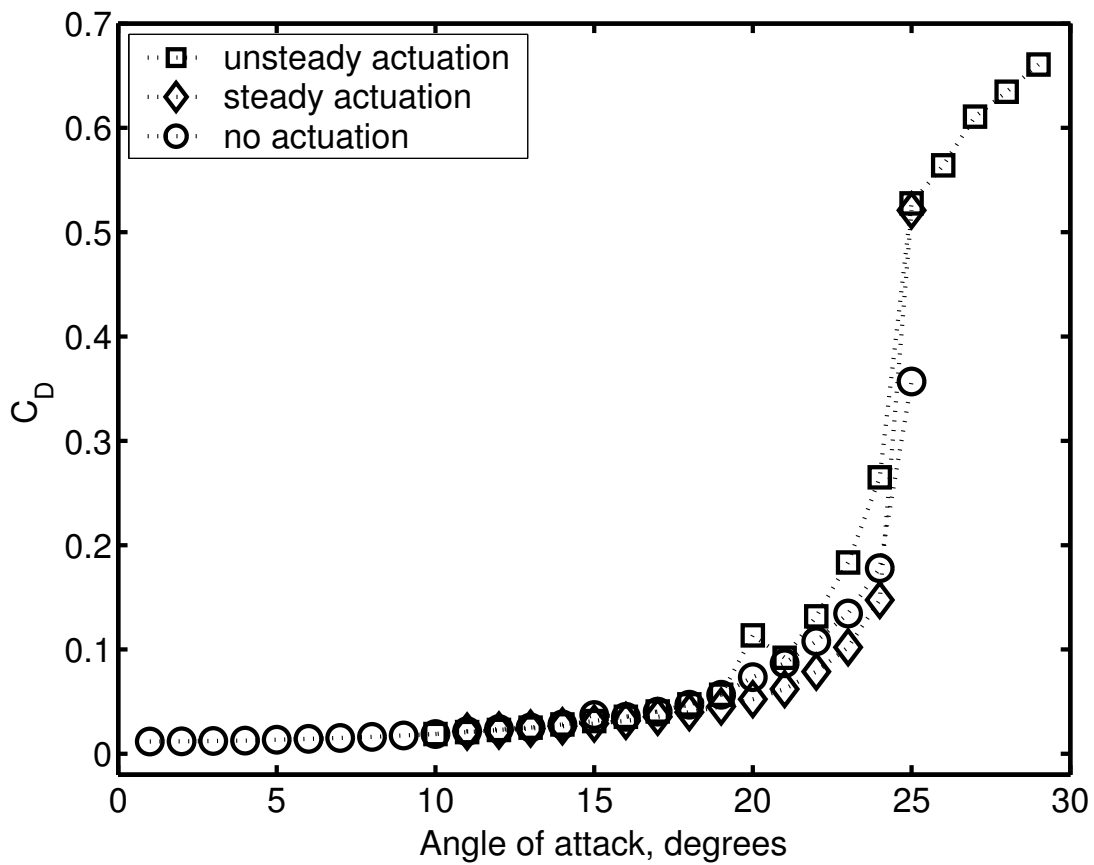


Figure 5.19. Drag coefficient versus angle of attack at $U_{fs} = 35$ m/s for uncontrolled flow, steady and unsteady actuation.

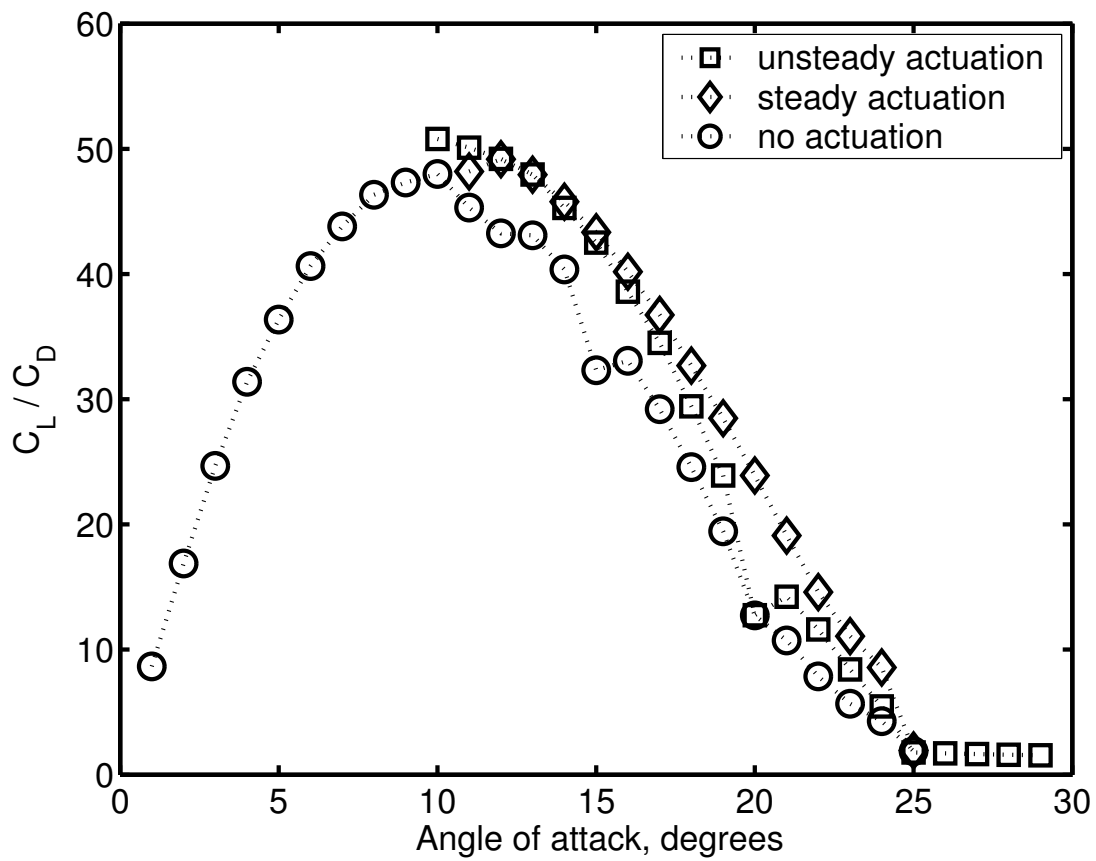


Figure 5.21. $\frac{C_L}{C_D}$ versus angle of attack at $U_{fs} = 35$ m/s for uncontrolled flow, steady and unsteady actuation.

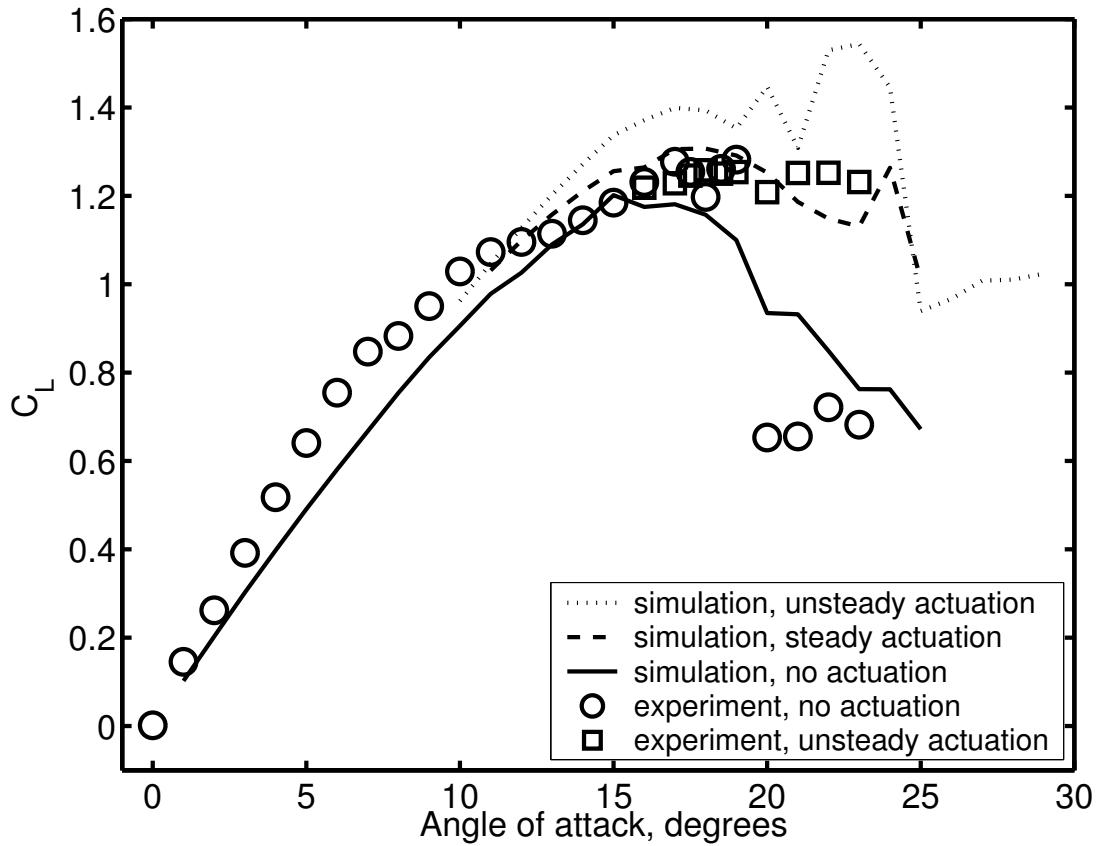


Figure 5.22. Comparison between numerical and experimental data for lift coefficient versus angle of attack for uncontrolled case, steady and unsteady actuation. Numerical simulations performed at $U_{fs} = 35$ m/s. Experiment performed at $U_{fs} = 30$ m/s, adopted from [52].

CHAPTER 6

CONCLUSIONS AND RECOMMENDATIONS FOR FUTURE WORK

This chapter presents conclusions related to the study of the physics of the single dielectric barrier discharge and the numerical model created to simulate it. In addition it summarizes the results of the numerical simulation of the leading-edge separation control on an airfoil. Finally it makes recommendations for the future work toward understanding the physics of the plasma actuator and modifying the electric circuit model to include these physics.

6.1 Conclusions

This section presents conclusions on the experimental investigation, modeling and numerical simulation of the plasma discharge and its application to leading-edge separation control.

6.1.1 Physics of Discharge

The single dielectric barrier discharge plasma actuator was characterized through a set of experiments. The focus was on the study of the light emission from the plasma actuator related to the plasma formation on the dielectric surface. These experiments were fundamental in understanding the physics of the discharge on the time scale associated with the applied a.c. cycle.

The double-slit photomultiplier was used to measure the light emission from the plasma actuator. Through the comparison with the electric current results, it was shown that the light emission directly correlated with the formation of the plasma discharge, and could be used as the measure of the volume of plasma on the dielectric surface. The light emission was measured while varying several parameters. One of the parameters was the applied a.c. voltage amplitude. The other parameter varied was the applied a.c. frequency.

The photomultiplier experiments revealed a very complex structure of the plasma discharge. During the operation of the plasma actuator, the plasma appears on the surface of the dielectric near the overlap junction of the electrodes. The volume of the plasma increases during the a.c. cycle, and the plasma sweeps across the surface. Given that the covered electrode is sufficiently wide, the plasma growth stops when the voltage difference across the plasma region becomes less than the voltage needed to maintain the plasma. This happens when the applied voltage reaches its maximum or minimum values. At this moment the plasma on the dielectric surface quenches.

The effect of the applied voltage amplitude on the discharge characteristics was investigated. For this, the a.c. frequency was kept constant at 5 kHz, and the amplitude of the applied voltage was varied in the range of 5-10 kV_{*p-p*}. The total light emission from the plasma actuator was found to be $L \propto V_{app}^{7/2}$. This agreed with the experimental results of Post [61] for the maximum plasma induced velocity and results of Enloe *et al.* [20, 21] for the thrust produced by the plasma actuator. In this set of experiments it was also found that the plasma propagation velocity increased slightly with the applied voltage amplitude. The plasma sweep velocity was found to be in the range of 70-110 m/s. It was also found that the

maximum extent of the plasma increased linearly with the voltage amplitude. These results agreed with the previous observations by Enloe *et al.* [20, 21].

The effect of the applied a.c. frequency was also studied. For this, a fixed applied voltage amplitude of 5 kV_{p-p} was used. In these experiments, the a.c. frequency was changed in the range of 5-11 kHz. It was found that the extent of the plasma over the dielectric surface did depend on the a.c. frequency. This resulted in a strong linear dependence of the plasma sweep velocity on the a.c. frequency. The observed sweep velocities were in the range of 80-180 m/s.

6.1.2 Electrostatic Model

In the experiments, it has been observed that there exist three different time scales associated with the plasma actuator. The first time scale, relates to the formation of the microdischarges, which is on the order of 10^{-8} seconds. The second time scale, defined by the a.c. frequency of the applied voltage, is on the order of 10^{-4} seconds. The largest time scale in the operation of the plasma actuator is associated with the neutral fluid response time which is of the order of 10^{-2} seconds.

This difference in time scales allowed us to construct a quasi-steady electrostatic model for the plasma actuator and to derive the plasma body force from first principles. This model included the idea of the Debye shielding in the plasma. The electrostatic model was used to study the asymmetric electrode arrangement. The distribution of the electric potential, electric field and the charge density were calculated near the electrodes. From these, the plasma body force was calculated.

The importance of accounting for the volume of the plasma over the covered electrode was also shown. This was done by applying the spatial weighting to the

body force results. The exponential form of the weighting function was chosen to reflect the experimental observations. Another type of the weighting that was used was a temporal weighting. It represented the linear growth of the volume of plasma during the a.c. cycle.

The spatially weighted and temporally-spatially weighted plasma body forces were used in the flow solver to model the flow in the closed box with the plasma actuator located on the bottom wall. The plasma body force computed separately, was introduced into the right hand side of the momentum equation point by point.

The numerical simulations showed the formation and growth of a starting vortex that was previously observed in the experiments by Post [61]. It was also shown that at $T \rightarrow \infty$, the induced flow developed into a the jet flow with the fluid drawn to the actuator and then accelerated downstream. The velocity profiles in the similarity region were used to compare the solutions for the spatially weighted and temporally-spatially weighted plasma body force cases. It was shown that the flow development was similar in both cases, but the maximum velocities in the jet were lower in case of the temporal-spatial weighting.

It was shown that the electrostatic model could be used to simulate the aerodynamic plasma actuator if the volume of plasma was know for the particular applied voltage conditions. An attempt to extrapolate these results to other voltage amplitudes was not possible with this model.

6.1.3 Lumped-element Circuit Model

To account for the change in the volume of plasma with respect to the applied voltage amplitude and frequency, the lumped-element circuit model was created. This model represented the plasma actuator as a parallel network of resistive and

capacitive elements. The capacitive elements representing the dielectric allowed us to model the accumulation of the charge on the surface of the dielectric.

Two types of the lumped-element circuit models were tested. The first model was a coarse spatial lumped-element circuit model. In this model, the plasma was represented by the time-varying resistive and capacitive elements. The values of these depended on the volume of the plasma present over the dielectric. As tests of this model showed, the power dissipated in the plasma actuator was $P \propto V_{app}^{7/2}$. This result is consistent with the results of Post [61] for the maximum velocity in the plasma jet and Enloe *et al.* [20, 21] for the thrust produced by the plasma actuator.

The second model was a spatial-temporal lumped-element circuit model. It was developed to simulate the internal structure of the plasma discharge. This model represented the plasma a series of parallel networks, each consisting of resistive and capacitive elements, and zenor diodes that controlled the values based on the current direction. The advantage of this model was that it could investigate the effect of amplitude and frequency without the need of experimentally determined coefficients. Prior to any other tests, this model was tested for the optimal number of parallel sub-circuits.

The space-time lumped-element circuit model allowed us to obtain the information about the current in the plasma, which has been shown previously to correlate directly to the light emission from the plasma. The results of the current distribution were found to be consistent with the light intensity measurements.

The effect of the applied voltage amplitude and a.c. frequency on the plasma characteristics was examined with the space-time lumped-element circuit model. The results were found to be in good agreement with the experimental results. The

maximum extent of the plasma was increasing linearly with the applied voltage amplitude, but was almost constant over the entire range of the a.c. frequencies tested. The plasma sweep velocity was found to increase linearly with the applied voltage amplitude and a.c. frequency.

The results of space-time lumped-element circuit model were used to calculate the time-resolved plasma body force. It was found that the plasma body force has four peaks during the a.c. cycle, and that the direction of the plasma body force is the same all the time. Spectral analysis performed on the plasma body force time series showed that the dominating frequency in the spectrum was two times the a.c. frequency.

The effect of the dielectric properties of the material was studied with the space-time lumped-element circuit model. The plasma body force calculations were performed for three different materials with $\varepsilon = 10, 100,$ and 1000 . It was shown that for each material tested there exists an optimal frequency at which the plasma body force is maximum. It was found that the optimal frequency decreased as the dielectric coefficient increased. The power dissipated in plasma due to ohmic heating monotonically increased with frequency. Therefore, too high a frequency is inefficient in terms of converting the input power into the body force.

6.1.4 Leading-edge Separation Control

With this approach, the leading-edge separation control on NACA 0021 using single-dielectric barrier discharge plasma actuator was studied numerically. FLUENT software was used to solve two-dimensional unsteady Reynolds-averaged Navier-Stokes equations with the $v^2 - f$ turbulence model.

The plasma actuator was modeled on the leading edge of the airfoil. The plasma body force computations were carried out using FemLab. The body force was then introduced into the flow solver using the user defined function.

The effect of the plasma actuator body force on the fluid was studied in still air. The formation of the starting vortex was observed near the actuator. The steady plasma actuator working for a long time form a jet near the airfoil surface. The unsteady plasma actuator was observed to form a periodic series of vortexes near the leading edge.

First, the flow around the airfoil was computed without any actuation for a range of angles of attack at 35 m/s inflow velocity. The convergence of the solution was based on the lift and drag coefficients. It was shown that at the lower angles of attack the airfoil characteristics were consistent with the linear airfoil theory, that is having the slope $\frac{dC_L}{d\alpha} = 2\pi$. The aerodynamic stall of the airfoil was observed at 18 degrees.

The leading-edge separation control with the steady and unsteady flow actuation was studied numerically. During the steady actuation, the plasma body force was permanently present. For the unsteady actuation, the body force was present only for 10% of the duty cycle. The frequency of the unsteady actuation corresponded to $F^+ = fc/U_{fs} = 1$.

In both cases, the separation bubble was observed to become smaller. The point of the separation was seen to move from the leading edge downstream to half-cord of the airfoil. This reduction of the separation bubble resulted in the increase of the lift and decrease of the drag of the airfoil.

It was found that the steady actuation increased the lift coefficient and delayed the stall by approximately 2 degrees of angle of attack. The unsteady actuation

was shown to produce even better results. The stall angle in that case was increased by 5 degrees. These results are consistent with the experiments for the same conditions.

6.2 Recommendations For Future Work

6.2.1 Physical Properties of Plasma Discharge

Recent experiments have shown the superiority of the Teflon dielectric over the traditional Kapton and PCB materials. This appears in the greater velocity of the plasma induced jet, and therefore, in the greater momentum transferred to the fluid. This advantage is probably due to the larger thickness of the Teflon dielectric layer which leads to a more uniform plasma discharge without filaments. This phenomenon of transition from the uniform plasma to filamentary discharge needs to be studied. This can be done by measuring the light emission from the filamentary and uniform plasma discharges using a photomultiplier. These experiments may also be accompanied by the acoustical measurements from the plasma actuator.

The SDB discharge plasma can also be studied optically with the fast CCD camera. The rate of data acquisition of this type of cameras (up to 10^5 images per second) allows one to obtain images of single discharge streamers. This information can help to further improve our knowledge about the physics of the discharge and refine the phenomenological model for plasma actuators.

In the present research one form of the input voltage signal has been studied, particularly the sinusoidal wave form. Additional data needs to be collected for different form of the input voltage signal to calibrate and test the space-time lumped-element circuit model. PMT measurements of the light emission from

the plasma actuator may be done for the “triangle”, “positive sawtooth” and “negative sawtooth” wave forms. These tests should be performed for the range of different applied voltage amplitudes and a.c. frequencies. This would give the information about the conditions of the plasma formation and quenching as well as the dependence of the plasma characteristics on the voltage form.

The other open question in the physics of the SDB discharges is how the momentum is transferred to the neutral fluid. There exist several theories which propose the PUSH-push, PUSH-pull and other mechanisms for the plasma actuators, meaning that during the a.c. cycle the plasma actuator creates a strong and a weak body forces which act either in the same direction, or in opposite directions. This question may be resolved by the velocity measurements directly in the plasma region. Aero-optical laser devices and methods developed at the University of Notre Dame may be used for this. In these methods, the density fluctuations are estimated from the deflections of the laser light which passes through the fluid. For this experiment, the glass may be used as the dielectric material, and the bottom surface of this insulator may be cover with the reflecting material, which would act as a mirror for the laser light. The velocity fluctuations may be calculated from the obtained density fluctuations. These experiments are intended to show if the fluid is accelerated during both halves of the a.c. cycle.

6.2.2 Improvements to the Lumped-element Circuit Model

Some improvements may be made for the lumped-element circuit model and plasma body force computations. As mentioned in the previous subsection, the plasma discharge may transition from the uniform regime to the filamentary regime. This formation of filaments may be accounted for in the model through

introduction of another resistive element with a possibly lower resistance value. This resistive element should be included into the circuit along with the zenor diode element which would govern the initiation of the filaments. The condition of this initiation may be possibly formulated using the voltage threshold for this transition from the uniform plasma. The value of the transition threshold voltage may be obtained experimentally.

The other improvement that may be done to the space-time lumped-element circuit model regards the breakdown of the dielectric layer. The condition for this breakdown and eventual shortage of the actuator circuit can be estimated from the dielectric strength of the material used for insulation.

In this work, the Lumped-element circuit model was tested for the sinusoidal applied voltage. In practical applications, the forms of the input signal are also used, such as the triangle wave, the “positive” and the “negative” sawtooth signals. The Lumped-element Circuit Model should be also tested for these forms of the input voltage. The results may be compared to the existing experimental results.

Another modification may be done in terms of the charge density estimation which is later used in the body force computations. The Lumped-element Circuit model gives us the information about the electric current that flows through the plasma actuator in each of the sub-circuits. This current is directly related to the number of the charges and their velocities. This means that if we can estimate the velocities of the charges in the plasma, then we can compute the ionization rate in each of the sub-circuits, and calculate the plasma body force directly without solving the Poisson electrostatic equation. The velocity of the charges can be estimated in several different ways. For example, this can be done assuming the Maxwell’s distribution for the gas particles.

6.2.3 Applications

The success of the numerical simulation of the leading edge separation control opens the possibilities for numerical study of other applications of the plasma actuators for flow control. For example, the active boundary layer control on the pitching airfoils may be studied computationally. The experimental data for this type of flow control was gathered previously by M. Post [61]. This study can be extended to include the plasma actuator into flow control on the micro air vehicles, UAVs, and flapping wings. In these simulations, the optimal configuration and active control strategy can be obtained for each flow control. This would help to optimize the performance of the plasma actuators in the experiments.

Another aspect of the flow actuation, which is of big importance, deals with the role played by the plasma actuators in the laminar-to-turbulent transition and transition delay and control. This study may be done by utilizing the e^N method, which had been shown to work fairly well for the situations in which the level of the free stream turbulence intensity is relatively low (flows around airfoils with turbulence intensity $< 1\%$).

BIBLIOGRAPHY

1. *IMSL Fortran Subroutines for Mathematical Applications*, 1977.
2. *COMSOL Multiphysics 3.2 User's Guide*, 2005.
3. *FLUENT 6.2 Documentation*, 2005.
4. *Gambit 2.2.30 Documentation*, 2005.
5. *MatLab 7.2.0.283 Documentation*, 2006.
6. ANDERSON, D. A., TANNEHILL, J. C., AND PLETCHER, R. H. *Computational Fluid Mechanics and Heat Transfer*. Hemisphere Publishing Corporation, 1984.
7. ANDERSON, R., AND ROY, S. Preliminary Experiments of Barrier Discharge Plasma Actuators Using Dry and Humid Air. AIAA Paper 2006-369, 2006.
8. ASGHAR, A., JUMPER, E. J., AND CORKE, T. C. On the Use of Reynolds Number as the Scaling Parameter for the Performance of Plasma Actuator in a Weakly Compressible Flow. AIAA Paper 2006-21, 2006.
9. BAIRD, C., ENLOE, C., McLAUGHLIN, T., AND BAUGHN, J. Acoustic testing of the dielectric barrier discharge (DBD) plasma actuator. AIAA Paper 2005-0565, 2005.
10. BATCHELOR., G. *An Introduction to Fluid Dynamics*. 1967.
11. CORKE, T. C. *Design of Aircraft*. Prentice Hall Publishers, New York, 2002.
12. CORKE, T. C., HE, C., AND PATEL, M. Plasma flaps and slats: an application of weakly-ionized plasma actuators. AIAA Paper 2004-2127, 2004.
13. CORKE, T. C., JUMPER, E. J., POST, M. L., ORLOV, D., AND McLAUGHLIN, T. E. Application of weakly-ionized plasmas as wing flow-control devices. AIAA Paper 2002-0350, 2002.

14. CORKE, T. C., MERTZ, B., AND PATEL, M. P. Plasma Flow Control Optimized Airfoil. AIAA Paper 2006-1208, 2006.
15. DOUVILLE, T., STEPHENS, J., CORKE, T., AND MORRIS, S. Turbine Blade Tip Leakage Flow Control by Partial Squealer Tip and Plasma Actuators. AIAA Paper 2006-20, 2006.
16. DURBIN., P. Separated flow computations with the k - ϵ - v^2 model. *AIAA Journal* 33 (1995), 659–664.
17. ENLOE, C. private communications, USAF Academy, CO, 2004.
18. ENLOE, C., MCCLAUGHLIN, T., FONT, G., AND BAUGHN, J. Parametrization of Temporal Structure in the Single Dielectric Barrier Aerodynamic Plasma Actuator. AIAA Paper 2005-0564, 2005.
19. ENLOE, C., MCCLAUGHLIN, T., VANDYKEN, R., AND FUSCHER, J. Plasma structure in the aerodynamic plasma actuator. AIAA Paper 2004-0844, 2004.
20. ENLOE, L., MCCLAUGHLIN, T., VANDYKEN, KACHNER, JUMPER, E., AND CORKE, T. Mechanisms and responses of a single-dielectric barrier plasma actuator: Plasma morphology. *AIAA* 42 (2004), 589–594.
21. ENLOE, L., MCCLAUGHLIN, T., VANDYKEN, KACHNER, JUMPER, E., CORKE, T., POST, M., AND HADDAD, O. Mechanisms and responses of a single-dielectric barrier plasma actuator: Geometric effects. *AIAA* 42 (2004), 585–604.
22. FONT, G. Boundary Layer Control with Atmospheric Plasma Discharges. AIAA Paper 2004-3574, 2004.
23. FONT, G., AND MORGAN, W. L. Plasma Discharges in Atmospheric Pressure Oxygen for Boundary Layer Separation Control. AIAA Paper 2005-4632, 2005.
24. FORTE, M., JOLIBOIS, J., MOREAU, E., TOUCHARD, G., AND CAZALENS, M. Optimization of a Dielectric Barrier Discharge Actuator by Stationary and Non-stationary Measurements of the Induced Flow Velocity - Application to Airflow Control. AIAA Paper 2006-2863, 2006.
25. GAITONDE, D. V., VISBAL, M. R., AND ROY, S. Control of Flow Past a Wing Section with Plasma-based Body Forces. AIAA Paper 2005-5302, 2005.
26. GIBALOV, V., AND PIETSCH, G. The development of dielectric barrier discharges in gas gaps and on surfaces. *J.Phys.D* 33 (2000).

27. GOLUBOVSKII, Y., MAIOROV, V., BEHNKE, J., AND BEHNKE, J. Influence of interaction between charged particles and dielectric surface over a homogeneous barrier discharge in nitrogen. *Journal of Physics D: Applied Physics* 35 (2002).
28. HALL, K., JUMPER, E. J., CORKE, T. C., AND MCCLAUGHLIN, T. E. Potential Flow Model of a Plasma Actuator as a Lift Enhancement Device. AIAA Paper 2005-0783, 2005.
29. HALL, K. D. Potential flow model for plasma actuation as a lift enhancement device. Master's thesis, University of Notre Dame, 2004.
30. HOFFMANN, K. A., AND CHIANG, S. T. *Computational Fluid Dynamics For Engineers*. Engineering Education System, 1993.
31. HUANG, J. *Documentation and control of flow separation on a linear cascade of Pak-B blades using plasma actuators*. PhD thesis, University of Notre Dame, 2005.
32. HUANG, J., CORKE, T., AND THOMAS, F. Separation control over low pressure turbine blades. In *Bulletin of the American Physical Society Division of Fluid Dynamics* (2002), vol. 47.
33. HUANG, J., CORKE, T., AND THOMAS, F. Separation control over low pressure turbine blades. In *Bulletin of the American Physical Society Division of Fluid Dynamics* (2003), vol. 48.
34. HUANG, J., CORKE, T. C., AND THOMAS, F. O. Plasma actuators for separation control of low pressure turbine blades. AIAA Paper 2003-1027, 2003.
35. HULTGREN, L. S., AND ASHPIS, D. E. Demonstration of separation delay with glow-discharge plasma actuators. AIAA Paper 2003-1025, 2003.
36. HUSSAIN, F., AND JEONG, J. On the identification of a vortex. *Journal of Fluid Mechanics* 285 (1995), 69–94.
37. KAKUTA, S., KAMATA, T., MAKABE, T., KOBAYASHI, S., TERAJ, K., AND TAMAGAWA, T. Study of surface charges on dielectric electrodes in a radio-frequency glow discharge. *J.Appl.Phys.* 77 (1995).
38. KOZLOV, K., WAGNER, H.-E., BRANDENBURG, R., AND MICHEL, P. Spatio-temporally resolved spectroscopic diagnostics of the barrier discharge in air at atmospheric pressure. *J.Phys.D:Appl.Phys.* 34 (2001).

39. LANDAU, L. D., AND LIFSHITZ, E. *Electrodynamics of continuous media*. Pergamon, 1984.
40. LIKHANSKII, A., SHNEIDER, M., MACHERET, S., AND MILES, R. Modeling of Interaction Between Weakly Ionized Near-Surface Plasmas and Gas Flow. AIAA Paper 2006-1204, 2006.
41. LIST, J., BYERLEY, A. R., MCCLAUGHLIN, T. E., AND VANDYKEN, R. D. Using a plasma actuator to control laminar separation on a linear cascade turbine blade. AIAA Paper 2003-1026, 2003.
42. MADANI, M., BOGAERTS, A., GIJBELS, R., AND VANGENEUGDEN, D. Modelling of a Dielectric Barrier Glow Discharge at Atmospheric Pressure in Nitrogen. In *International Conference on Phenomena in Ionized Gases* (2003).
43. MASSINES, F., RABEHI, A., DECOMPS, P., BEN GADRI, R., SEGUR, P., AND MAYOUX, C. Experimental and theoretical study of a glow discharge at atmospheric pressure controlled by dielectric barrier. *Journal of Applied Physics* 83 (1998).
44. MATLIS, E. H. *Controlled experiments on instabilities and transition to turbulence on a sharp cone at Mach 3.5*. PhD thesis, University of Notre Dame, 2004.
45. MORRIS, S. C., CORKE, T. C., VANNESS, D., STEPHENS, J., AND DOUVILLE, T. Tip Clearance Control Using Plasma Actuators. AIAA Paper 2005-0782, 2005.
46. NELSON, C., CAIN, A., PATEL, M., AND CORKE, T. Simulation of Plasma Actuators Using the Wind-US Code. AIAA Paper 2006-634, 2006.
47. ORLOV, D., AND CORKE, T. Numerical simulation of aerodynamic plasma actuator effects. AIAA Paper 2005-1083, 2005.
48. ORLOV, D., CORKE, T., AND HADDAD, O. DNS modeling of plasma array flow actuators. In *Bulletin of the American Physical Society Division of Fluid Dynamics* (2003), vol. 48.
49. ORLOV, D., CORKE, T., AND PATEL, M. Electric Circuit Model for Aerodynamic Plasma Actuator. AIAA Paper 2005-1206, 2006.
50. ORLOV, D., CORKE, T., AND POST, M. DNS modeling of plasma array flow actuators. In *Bulletin of the American Physical Society Division of Fluid Dynamics* (2002), vol. 47.

51. ORLOV, D., ERTURK, E., POST, M., AND CORKE, T. DNS modeling of plasma array flow actuators. In *Bulletin of the American Physical Society Division of Fluid Dynamics* (2001), vol. 46.
52. ORLOV, D. M., APKER, T., HE, C., OTHMAN, H., AND CORKE, T. C. Modeling and experiment of Leading-edge Separation Control Using Single-dielectric Barrier Discharge Plasma Actuators. AIAA Paper, 2007.
53. PAI, S., GUO, X., AND ZHOU, T. Closed form analytic solution describing glow discharge plasma. *Phys.Plasmas* 3 (1996).
54. PATEL, M. P., SOWLE, Z. H., CORKE, T. C., AND HE, C. Autonomous Sensing and Control of Wing Stall Using a Smart Plasma Slat. AIAA Paper 2006-1207, 2006.
55. PAULUS, M., STALS, L., RUDE, U., AND RAUSCHENBACH, B. Two-dimensional simulation of plasma-based ion implantation. *Journal of Applied Physics* 85 (1999).
56. POGGIE, J. DC Glow Discharges: A Computational Study for Flow Control Applications. AIAA Paper 2005-5303, 2005.
57. PORTER, C., BAUGHN, J., MCLAUGHLIN, T., ENLOE, C., AND FONT, G. Temporal Force Measurements on an Aerodynamic Plasma Actuator. AIAA Paper 2006-104, 2006.
58. POST, M., AND CORKE, T. Separation control using plasma actuators. In *Bulletin of the American Physical Society Division of Fluid Dynamics* (2002), vol. 47.
59. POST, M., AND CORKE, T. Airfoil leading-edge separation control using plasma actuators. In *Bulletin of the American Physical Society Division of Fluid Dynamics* (2003), vol. 48.
60. POST, M. L. Phased plasma actuators for unsteady flow control. Master's thesis, University of Notre Dame, 2001.
61. POST, M. L. *Plasma actuators for separation control on stationary and unstationary airfoils*. PhD thesis, University of Notre Dame, 2004.
62. POST, M. L., AND CORKE, T. C. Separation control on high angle of attack airfoil using plasma actuator. AIAA Paper 2003-1024, 2003.
63. POST, M. L., AND CORKE, T. C. Separation control using plasma actuators - stationary and oscillatory airfoils. AIAA Paper 2004-0841, 2004.

64. ROTH, J. *Industrial plasma engineering*. Institute of Physics Publishing, 1995.
65. ROTH, J., SHERMAN, D., AND WILKINSON, S. Electrohydrodynamic flow control with a glow-discharge surface plasma. *AIAA Journal* 38 (2000).
66. ROY, S., AND GAITONDE, D. V. Radio frequency induced ionized collisional flow model for application at atmospheric pressures. *Journal of Applied Physics* (2004).
67. ROY, S., AND GAITONDE, D. V. Modeling Surface Discharge Effects of Atmospheric RF on Gas Flow Control. AIAA Paper 2005-0160, 2005.
68. ROY, S., PANDEY, B., POGGIE, J., AND GAITONDE, D. V. Modeling low pressure collisional plasma sheath with space-charge effect. *Physics of Plasmas* 10 (2003), 2578–2585.
69. SHYY, W., JAYARAMAN, B., AND ANDERSSON, A. Modeling of glow discharge-induced fluid dynamics. *Journal of applied physics* 92 (2002).
70. SIEMENS, W. *Poggendorffs Ann. Phys. Chem.* 102 (1857).
71. SUZEN, Y., AND HUANG, P. Simulation of Flow Separation Control using Plasma Actuators. AIAA Paper 2006-877, 2006.
72. SUZEN, Y., HUANG, P., JACOB, J., AND ASHPIS, D. Numerical Simulations of Plasma Based Flow Control Applications. AIAA Paper 2005-4633, 2005.
73. THOMAS, F. O., KOZLOV, A., AND CORKE, T. C. Plasma Actuators for Bluff Body Flow Control. AIAA Paper 2006-2845, 2006.
74. VAN NESS, D. K., CORKE, T. C., AND MORRIS, S. C. Turbine Tip Clearance Flow Control using Plasma Actuators. AIAA Paper 2006-21, 2006.
75. VISBAL, M. R., AND GAITONDE, D. V. Control of Vortical Flows Using Simulated Plasma Actuators. AIAA Paper 2006-505, 2006.
76. VOIKOV, V., CORKE, T., AND HADDAD, O. Numerical simulation of flow control over airfoils using plasma actuators. In *Bulletin of the American Physical Society Division of Fluid Dynamics* (2004), vol. 49.
77. WILKINSON, S. private communications, NASA Langley Research Center, VA, 2003.
78. WILKINSON, S. P. Investigation of an Oscillating Surface Plasma for Turbulent Drag Reduction. AIAA Paper 2003-1023, 2003.